PPTC propeller used as the turbine in the simulation of a **TUSK** energy system. **OpenFOAM** as the simulation tool to study *flow conditions* surrounding the *propeller*, *airfoil*, and *kite*. **SIMPLE** and **PIMPLE** algorithms to solve the *governing equations* in the $k-\omega$ SST turbulence model. Simulation validated against **PPTC** experimental data in the *propeller* case and against **XFOIL** code for the *airfoil* simulation. *Thrust* and *torque* were extracted from the simulation to produce the *performance* and *power* curves for the *hydrokinetic kite*.

Flow Simulation to Study SMART KITE Design

OpenFOAM using PIMPLE solver and kOmega SST Turbulence Model

Cuong Chi Nguyen at *University of Stavanger* in collaboration with *SMART KITE AS*

Preface

This is a master's thesis in *Master of Science in Engineering Structures and Materials* program at *University of Stavanger* written by **Cuong Chi Nguyen** Spring 2021 in collaboration with **SMART KITE** AS. Thanks to my supervisor *Knut Erik Teigen Giljarhus* associate professor within the field of *Computational Fluid Dynamics* (**CFD**) at the *Department of Mechanical and Structural Engineering and Materials Science*, and to my external advisor *Peter Sommer-Larsen* CEO of **SMART KITE** AS.

Abstract

The *Potsdam Propeller Test Case* **PPTC** propeller was used as the turbine for the flow simulation of the *tethered undersea kite* **TUSK** energy system in this project. **OpenFOAM** *'Propeller'* and *'wingMotion'* tutorials used as starting points to study the *flow conditions* surrounding the *propeller*, *airfoil*, and *kite*. **SIMPLE** and **PIMPLE** algorithms were used to solve the *governing equations* in the $k-\omega$ SST turbulence model. Simulation was validated against **PPTC** experimental data in the *propeller* case and against **XFOIL** code in the *airfoil* simulation. *Thrust* and *torque* were extracted from the simulation to produce the *performance* and *power* curves for the *hydrokinetic kite*.

Keywords

Computational fluid dynamics CFD, $k-\omega$ SST turbulence model, tethered undersea kite **TUSK** energy system, hydrokinetic kite, propeller, wingMotion, SIMPLE, PIMPLE, airfoil, crosswind drag powered kit.

Contents

Figures

Tables

Nomenclature

Governing Equations

$\boldsymbol{\rho}$	Fluid Density	$\boldsymbol{\mu}$	Dynamic Viscosity
$\boldsymbol{\nabla}$	$\vec{\nabla}=\left[\frac{\partial}{\partial x},\frac{\partial}{\partial y},\frac{\partial}{\partial z}\right]$	$\boldsymbol{\nabla^2}$	$\vec{\nabla}\cdot\vec{\nabla}=\left[\frac{\partial^2}{\partial x^2},\frac{\partial^2}{\partial y^2},\frac{\partial^2}{\partial z^2}\right]$
$\boldsymbol{\vec{u}}$	Velocity	$\boldsymbol{\vec{S}}$, $\boldsymbol{S_\phi}$	Source Term
$\boldsymbol{\phi}$	General Transport Property	$\boldsymbol{\Gamma}$	Diffusivity Constant
$\boldsymbol{\partial t, \Delta t, dt}$	Time Step		
$\boldsymbol{dA}$	Discretized Area	$\boldsymbol{dV}$, CV	Control Volume
$\boldsymbol{grad\ f}$	Gradient of a Scalar ∇f	$\boldsymbol{div\ \vec{F}}$	Divergent of a Vector $\nabla\cdot\vec{F}$

Turbulence Model

$\boldsymbol{u}$	Velocity		
$\boldsymbol{\bar{u}}$	Mean value of u	$\boldsymbol{u'}$	Fluctuation of u around $\bar{u}$
$\boldsymbol{\tau_{ij}}$	Reynold's Stresses	$\boldsymbol{s_{ij}}$	Rate of Deformation
$\boldsymbol{\overline{u_i'u_j'}}$	Time average of the product of u_i' and u_j'	$\boldsymbol{\delta_{ij}}$	Kronecker Delta
$\boldsymbol{\mu_t}$	(Turbulent) Eddy *Viscosity*	$\boldsymbol{\Gamma_t}$	(Turbulent) Eddy *Diffusivity*
$\boldsymbol{k}$	Turbulent Kinetic Energy	$\boldsymbol{\delta_{ij}}$	Kronecker Delta
$\boldsymbol{v}$	Characteristic Velocity Scale	$\boldsymbol{\ell}$	Characteristic Length Scale

$C_\mu, \sigma_k, \sigma_\varepsilon, C_{1\varepsilon}, C_{2\varepsilon}$	$k-\varepsilon$ model constants		
U_{ref}	Reference Velocity	T_i	Turbulence Intensity
ω	Turbulence Frequency	$P_k, P_\omega, P_{\omega,2}$	Collection Term
$\sigma_k, \sigma_\omega, \gamma_1, \beta_1, \beta^*$	$k-\omega$ model constants		
u^+	Dimensionless u	y^+	Dimensionless y
τ_w	Wall Shear Stress	u_τ	Near-Wall Velocity Scale
U_∞	Free Stream Velocity	κ, B, E, A	Universal Constants
δ	Boundary Layer Thickness	ν	Kinematic Viscosity
$\sigma_k, \sigma_{\omega,1}, \sigma_{\omega,2}, \gamma_2, \beta_2, \beta^*$	SST $k-\omega$ model constants		
C_f	Skin Friction	L	Characteristic Length
Re	Reynold's Number	Re_L	Local Reynolds's Number

Crosswind Kite Power

P	Power	P_w	Power Density
F	Power Factor	F_S	Power Factor (Simple Kite)
F_C	Power Factor (Lift Power)	F_D	Power Factor (Drag Power)
V_A	Apparent Velocity	V_w	Incoming Velocity
D_K	Kite Drag	D_P	Turbine Drag
L	Lift	C_p	Betz's Limit

Airfoil vs Wing

c_l	Lift Coefficient (Airfoil)	c_d	Drag Coefficient (Airfoil)
α	Angle of Attack (geometric)	α_i	Angle of Attack (induced)
α_{eff}	Angle of Attack (effective)	$\alpha_{L=0}$	Zero-lift Angle of Attack
$C_{D,i}$	Lift Induced Drag	C_L	Lift Coefficient (Wing)
δ	Induced Factor for Drag	C_D	Drag Coefficient (Wing)
e	Span Efficiency Factor	τ	Lift Efficiency Factor
a_0	Lift Slope (Airfoil)	a	Lift Slope (Wing)
$\Gamma(y)$	Circulation Distribution	Γ_0	Vortex Filament Strength
AR	Aspect Ratio	S	Wing Area
b	Wingspan	c	Chord Length

PPTC

K_T	Thrust Coefficient	K_Q	Torque Coefficient
J	Advance Coefficient	η_0	Open Water Efficiency

1 Introduction

Economic development is a prerequisite and a necessary condition for other *social* or *humanitarian* development like eliminating *hunger*, alleviate *poverty* and reduce increasing *inequality* and ever widening gap between the rich and the poor, *developed* nations, and the *developing* countries. The severity and immediacy of **climate change** has only recently reached a somewhat global and universal consensus. Attempts to solve some ills seems to contradict or make it challenging to solve others. Although most people can agree on the *problem*, less agreement have been reached on *solutions*. For humanity to succeed with the lofty endeavor of reaching the *UN Sustainable Development Goals* (**SDG)** by the end of the century, preferably even the first half, greater leadership, commitment, and dedication is acutely needed. To allow the struggling south a chance and an opportunity to develop, the affluent north need to carry more of the load and pay more of the bill. The developed nations need to *invest* in research, *finance* implementation and *cut* own emissions. Clean *renewable* **energy** solution is one small but important contribution to the grander scheme.

1.1 Motivation

In the pursuit of greener energy solution for a sustainable future *crosswind drag powered* **kite** concepts first formulated by Loyd is one of the more interesting and promising concepts. The main idea behind these concepts is that the *apparent* **velocity** felt by the kite is much higher than the *incoming* wind speed. The **power** is proportional to the *velocity cubed* and it is theorized that the power potential in the wind is exponential when the velocity increases. The other inspiration behind these relatively new concepts is that the flying kite can *sweep* a larger **area** and therefore increase the overall power potential harvestable in the wind. The third thought behind these emerging proposals is the higher **density** of water comparative to air. Since power dependents on *density*, sweeping *area* and *velocity* cubed it is important to explore these three aspects to better understand the power potential in the fluid and any concepts attempting to harvest the energy from the fluid.

1.2 Literature

Aerodynamic performance of *horizontal axis wind turbine* (**HAWT**) blades has been well studied both computational and experimental, a review is presented in [1]. The focus has been on wind speed, rotational speed, and *tip speed ratio* (**TSR**). The classical *blade element momentum* (**BEM**) theory was an often-used numerical method. A more recent method has been *computational fluid dynamic* (**CFD**), where *large eddy simulation* (**LES**), *actuator disk method* (**ADM**), *actuator line method* (**ALM**), were among the innovations in the numerical computational field. Mixed BEM-CFD has been studied, and f*ield test* and *wind tunnel experiment* were performed as well. **Near wake** *experiments* has been of increasing interest and focus when commercial wind farms search to optimize array arrangements. Additional anomalies like *wind shear*, *gusts* and *yaw transition* were studied in [2]. The focus was on *blade deflection* and *performance* under aerodynamic *load* and *vibrational response* of the blades under aerodynamic *loading*.

Performance and *near wake* of a 0.90 *m* diameter three bladed turbine were studied in a wind tunnel in [3]. *Power*, *thrust*, *torque* and *rotor speed power coefficient* were measured with varying yaw angle as shown in figure below.

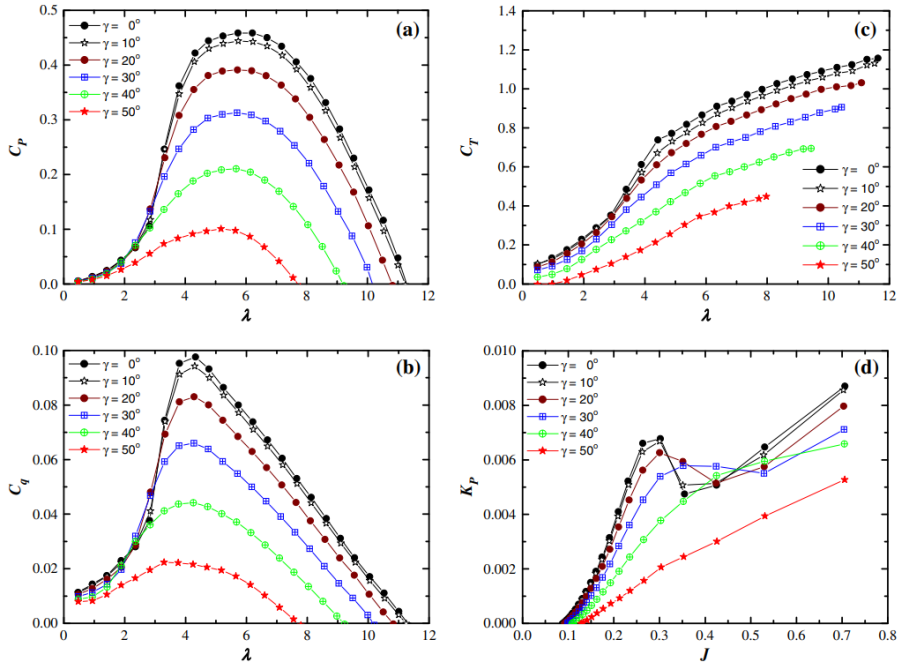

FIGURE 1 PERFORMANCE CHARACTERISTICS AT VARIOUS YAW ANGLES γ FOR (A) POWER COEFFICIENT C_P, (B) THRUST COEFFICIENT C_T, (C) TORQUE COEFFICIENT C_q AND (D) ROTOR SPEED POWER COEFFICIENT K_P.

A range of *computational method* was used to predict *performance* and *wake* development in [4]. Classic **BEM**, fully resolved **CFD**, and **LES** were among the methods participated in the study. Simulation was compared to the wind tunnel experimental data as shown in figures below.

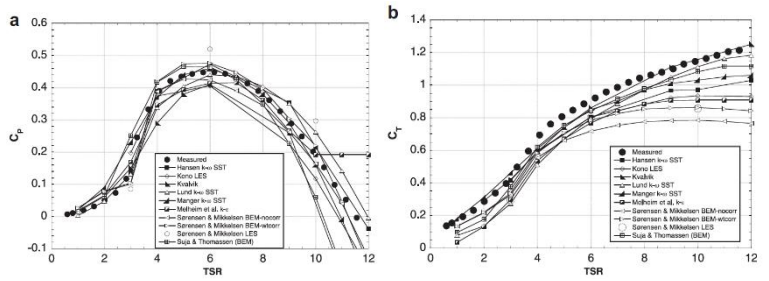

FIGURE 2 TURBINE PERFORMANCE. (A) POWER COEFFICIENT C_P (B) THRUST COEFFICIENT C_T

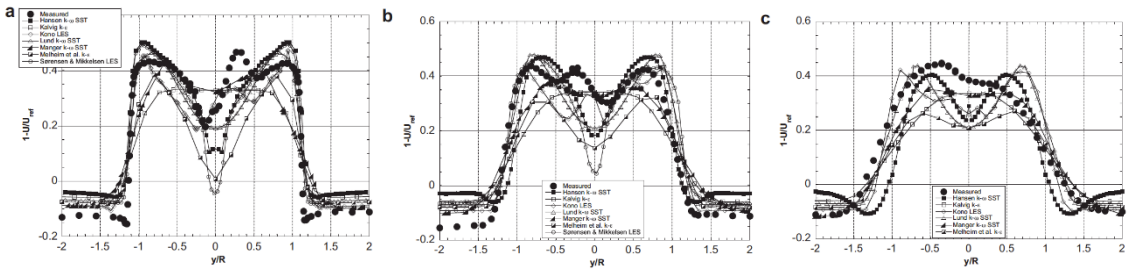

FIGURE 3 MEAN VELOCITY PROFILES ALONG A HORIZONTAL LINE FOR $TSR = 6$ (A) $X/D = 1$, (B) $X/D = 3$, (C) $X/D = 5$.

LES coupled with **ALM**, *Reynolds Average Navier-Stokes* **RANS** model using **ADM**, (unsteady) **U-RANS** using *fully resolved* blade geometry was among the 9 contributions in a study in [5]. The influence of the upstream on the downstream turbine and the subsequent high uncertainty in the results was expected; more surprising was the downwind turbine influence on the upstream one and the relative high scatter (±20%) in the calculation for the upstream turbine. Figure below shows the setup, figure on the next page compares the upstream and downstream turbine *power* and *thrust* coefficient with simulations.

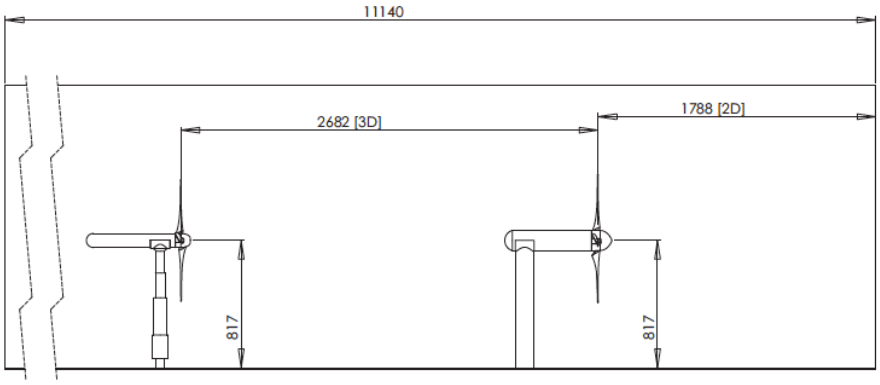

FIGURE 4 WIND TUNNEL SETUP PLAN.T_1 IN FRONT OF T_2 DIMENSIONS IN $[mm]$

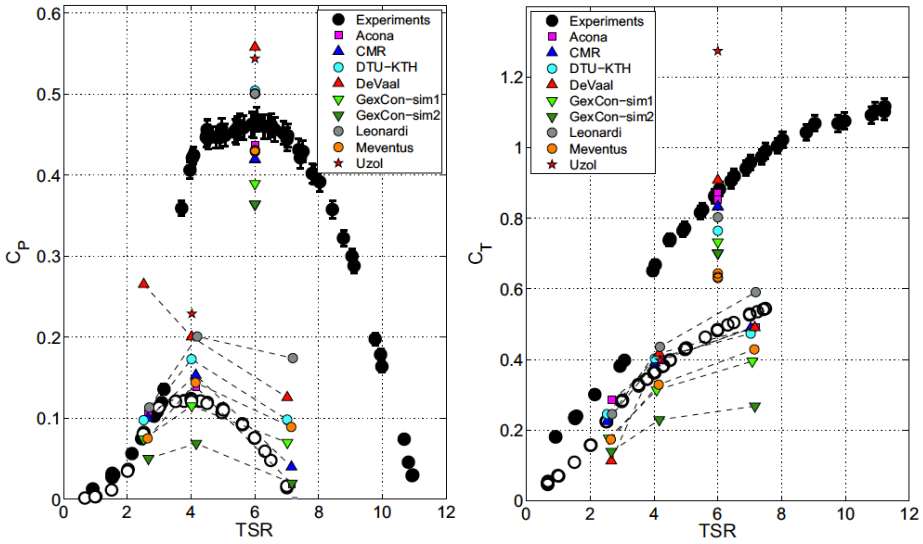

FIGURE 5 EXPERIMENTAL C_P(LEFT) OF C_T(RIGHT) OF T_1(FILLED CIRCLES) AND T_2(OPEN CIRCLES) VS. SIMULATIONS. UPSTREAM TURBINE T_1RUNS AT FIXED $\lambda_1 = 1.6$, T_2 RUNNING AT $\lambda_2 = 4,7$ and 2.5

Two in-line turbine models were again studied with a slight *offset* from each other in [6]. This arrangement is common and produces complex and harmful flow field downstream. The experiment was performed with and without grid in front of the first turbine as shown in figures below. The numerical method participated predicted *power* and *thrust* well, but the **LES** method seems to consistently outperform the others when studying *wake field*. Figures below summarize *power* and *thrust* coefficient.

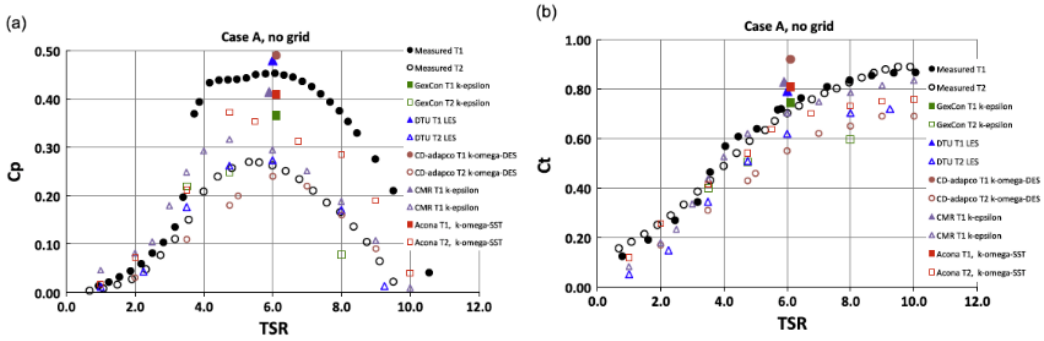

FIGURE 6 CASE A: (A) POWER COEFFICIENT C_P (B) THRUST COEFFICIENT C_T

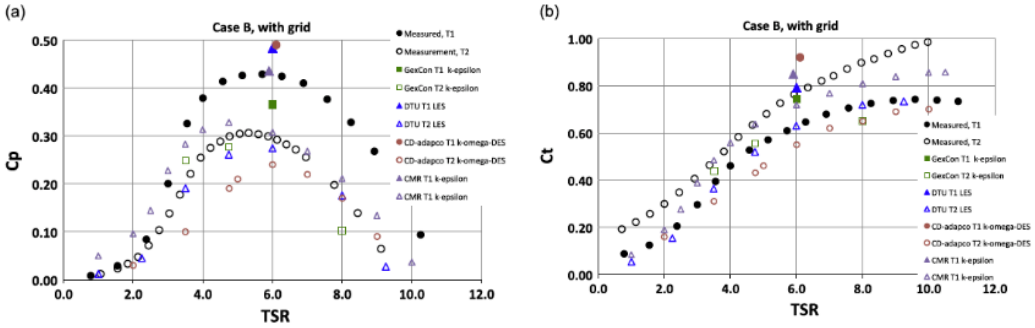

FIGURE 7 CASE B: (A) POWER COEFFICIENT C_P (B) THRUST COEFFICIENT C_T

The *National Renewable Energy Laboratory* (**NREL**) provides experimental measurement data. Figure below shows the only facility sizable enough to accommodate a 10-m-diameter wind turbine located at **NASA** *Ames Research Center at Moffett Field*, California [7]. 19 different wind turbine *modelling tools* were compared to *measurements* at the facility [8]. Assumptions on how to use 2D airfoil data and extrapolate it to 3D simulation was among the main explanation for discrepancies found in the study, provided by the participating modelers.

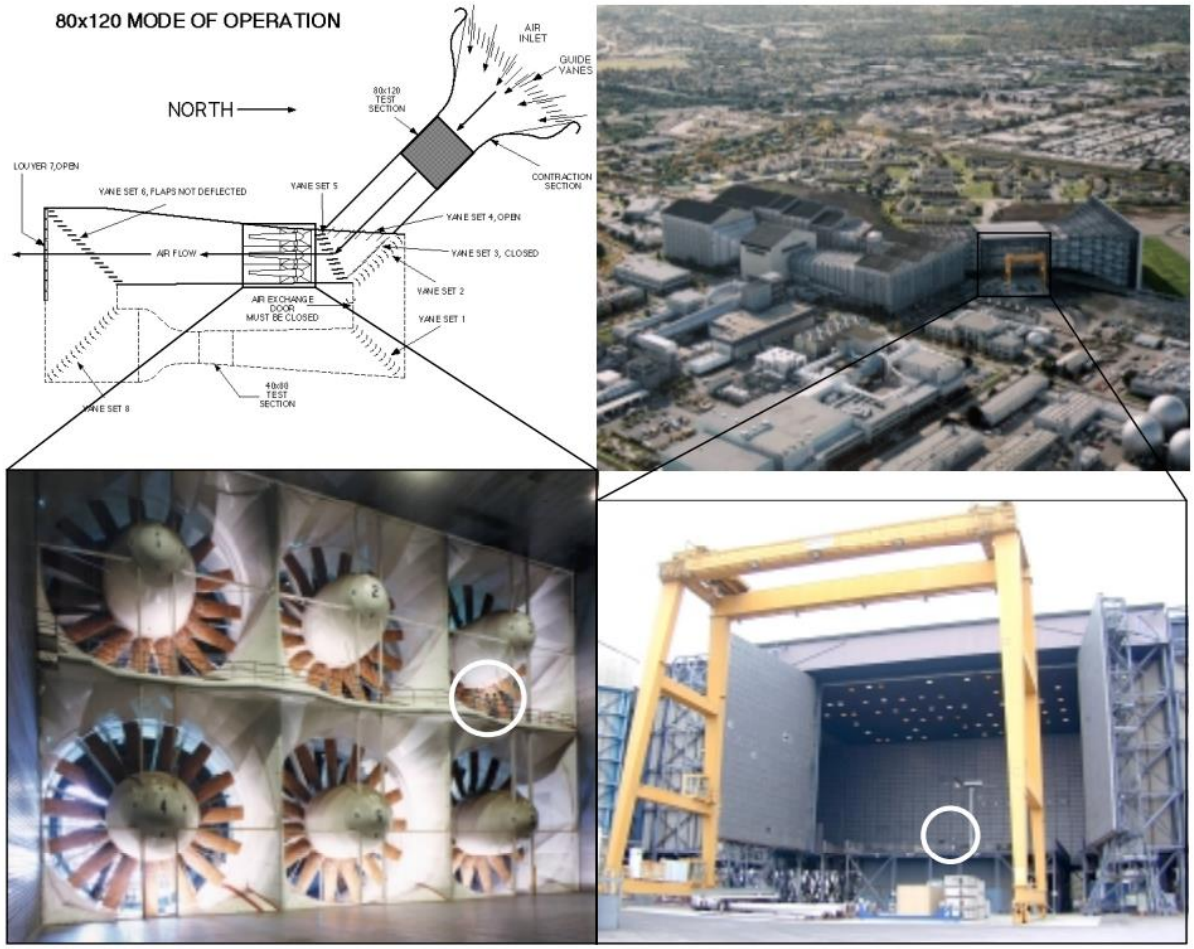

FIGURE 8 NASA AMES RESEARCH CENTER FULL-SCALE AERODYNAMICS COMPLEX WITH CLOSE-UP VIEW OF FAN DRIVES AND (80 X 120) TEST SECTION. NOTE PEOPLE FOR SCALE.

Actuator line method (**ALM**) wake field simulation of a *tidal stream turbine* (**TST**) was compared with *full rotor geometry* (**FRG**) and validated against experimental measurements in [9]. Figures below show the source term for the ALM, computational domain, rotational mesh for the FRG and comparison between the two methods.

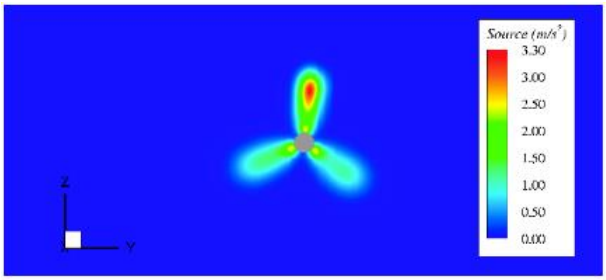

FIGURE 9 SOURCE TERMS IMPLEMENTED IN THE ACTUATOR LINE (AL) METHOD

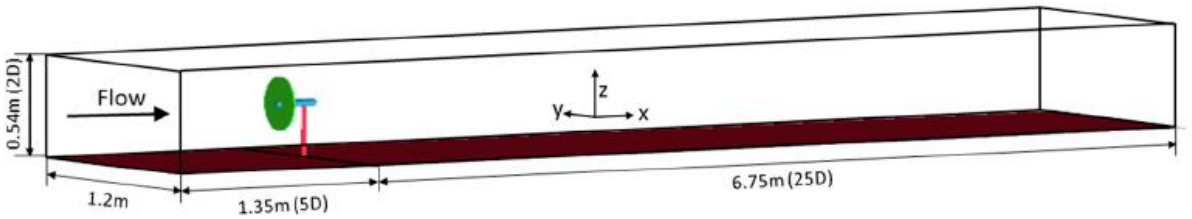

FIGURE 10 COMPUTATIONAL DOMAIN FOR THE AL METHOD. NACELLE AND MONO-PILE FOUNDATION

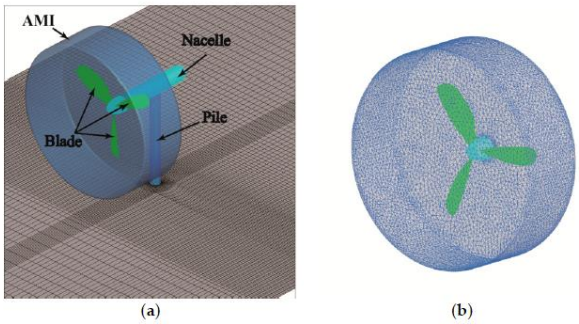

FIGURE 11 FULL ROTOR GEOMETRY (FRG) METHOD IN OPENFOAM. (A) FLOW FIELD DIVIDED INTO STATIC AND ROTATIONAL REGION. (B) THE ROTATIONAL REGION WITH UNSTRUCTURED MESH

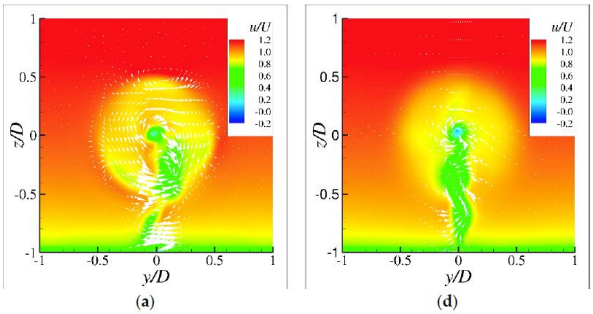

FIGURE 12 DEVELOPMENT OF WAKE ROTATION IN THE DOWNSTREAM WITH THE COLOR PRESENTING THE STREAMWISE VELOCITY AND THE ARROWHEAD CIRCULATION VECTOR. ALM ON THE LEFT AND FRG ON THE RIGHT

Design *parameters* of a water turbine and its effects on *performance* were studied in [10]. *Torque* was measured for varies *rotational speeds* and validated against two experimental datasets. Power output and power coefficient for varies *blade radius*, *blade numbers* and *incoming velocity* was studied. As expected, power is proportional to the square of the radius, cube of the velocity and the optimal blade number is three. Figures below are some of the results.

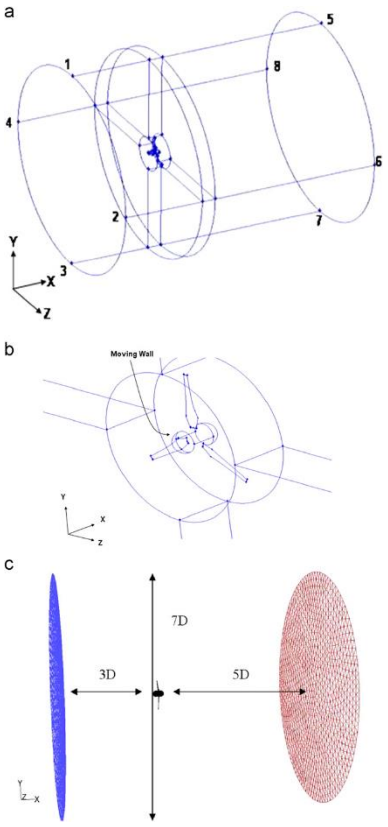

FIGURE 13 (A) COMPUTATIONAL DOMAIN; (B) CLOSE-UP OF THE ROTOR BOUNDARY; AND (C) SAMPLE COMPUTATIONAL DOMAIN SIZE

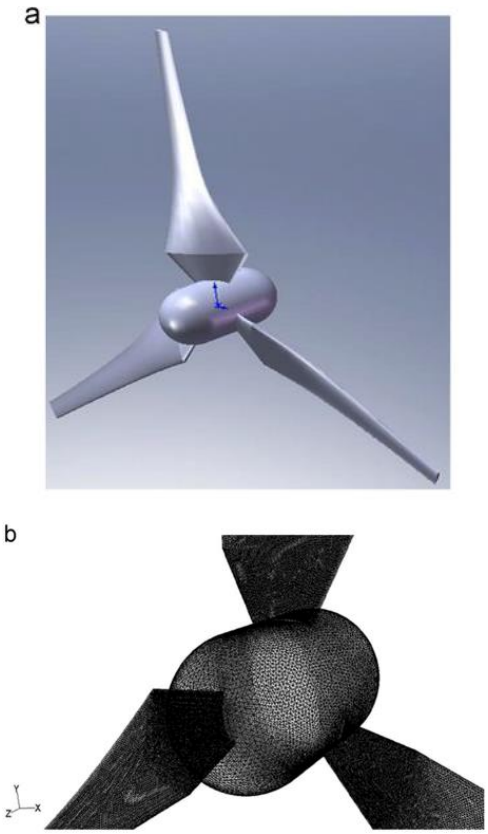

FIGURE 14 (A) ROTOR APPEARANCE (B)MESHING GRIDS AROUND THE HUB BOUNDARY AREAS

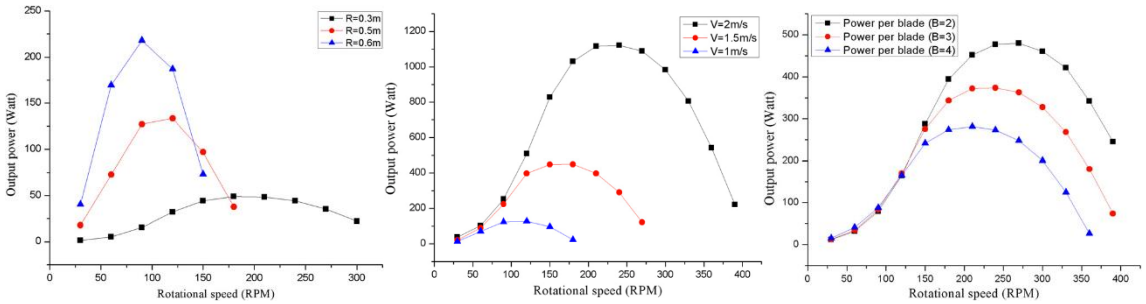

FIGURE 15 POWER YIELD VS. (1) BLADE RADIUS (2) INCOMING VELOCITY AND (3) BLADE NUMBER

Hydrokinetic energy conversion devices allow for energy harvest of hydropower without the need for large dams, impoundments or channels or deviation of large bodies of waters. A review of the CFD advancements in this field the recent 10-15 years is presented in [11]. Figure below shows different proposals.

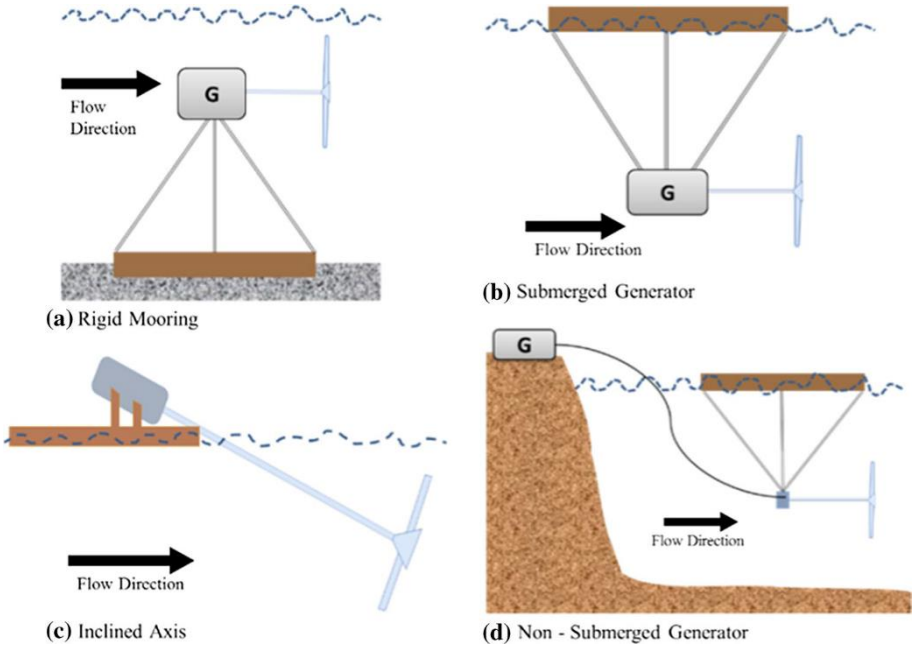

FIGURE 16 AXIAL FLOW TURBINES

Power and *thrust* measurements were performed on a 800 mm diameter *marine current turbine* (**MCT**) in a 60 m towing tank and a 2.4 m x 1.2 m cavitation tunnel in [12]. *Power* and *thrust* coefficient for a range of *tip speed ratios* (**TSRs**) and pitch setting were presented as shown in figure below.

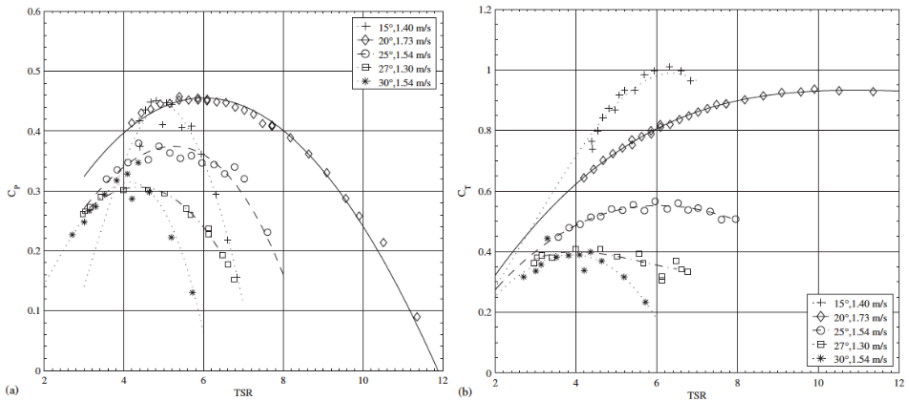

FIGURE 17 COMPARISONS OF HUB AT PITCH ANGLES AT THE CAVITATION TUNNEL—ZERO YAW. (A) POWER COEFFICIENT C_P, (B) THRUST COEFFICIENT C_T.

Two geometries of *rear diffuser* to *enhance* power output of hydrokinetic turbine was studied in a wind tunnel in [13]. First figures show the geometries of the diffuser designs studied. The other figure shows the enhanced power coefficient C_p of 48.7 % and 79.5% for S1223 and CII design, respectively, outperforming the theoretical Betz limit in both cases.

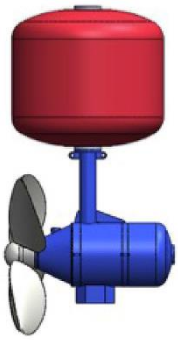

FIGURE 18 HYDROKINETIC TURBINE HK-10.

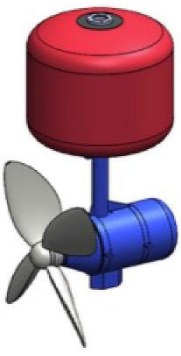

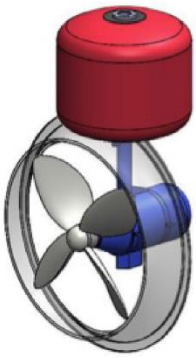

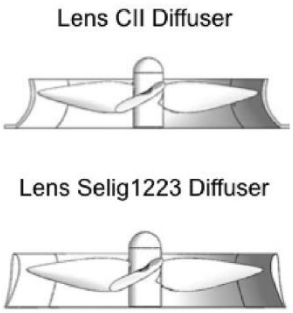

FIGURE 19 LENS DIFFUSERS CII AND S1223

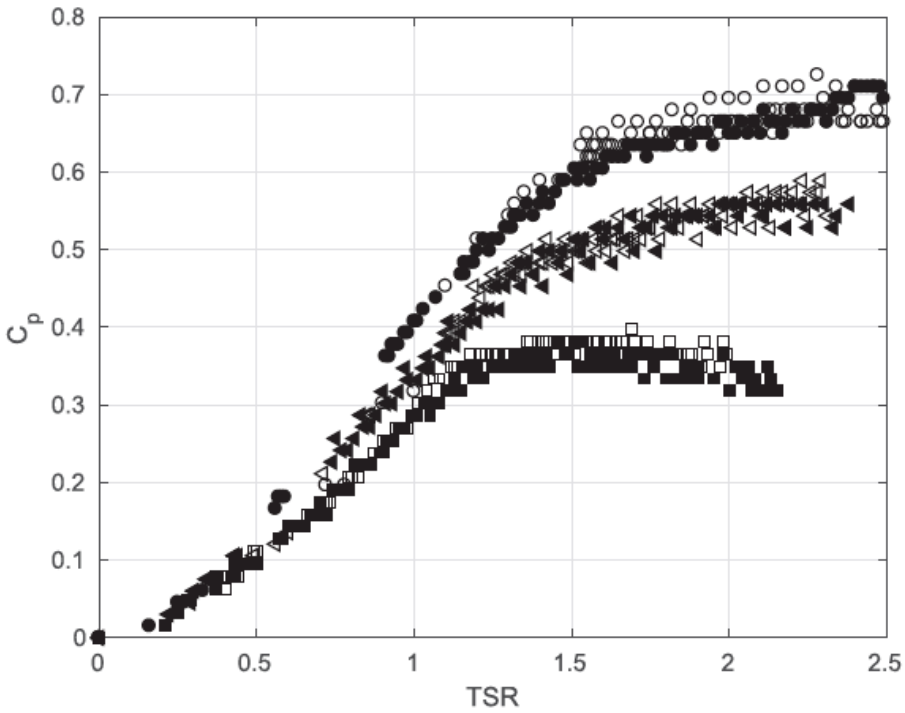

FIGURE 20 SHROUDED TURBINE PERFORMANCE. •*CII AT* $10\,m/s$; ◦*CII AT* $8\,m/s$; ◀$S1223$ *AT* $10\,m/s$; ◁$S1223$ *AT* $8\,m/s$; ▪*FREE RUNNER AT* $10\,m/s$; ▫*FREE RUNNER AT* $8\,m/s$.

Performance of a 2-bladed *horizontal axis marine current turbine* (**HAMCT**) was studied using **BEM** and **QBlade** (*theoretical*) and **RANS CFD** (*numerical*) and validated against experimental data from measurements in both *towing tank* (**TT**) and *circulating water channel* (**CWC**) at *Australian Marine College* (**AMC**) in [14]. Measurements were performed with *Acoustic Doppler Velocimeter* (**ADV**) on two scales, 500 *mm* and 800 *mm* diameter. Simulation tools for the study based on **BEM**, a commercial code (*GH-Tidal Bladed*) and an academic in-house code (*SERG-Tidal*), was developed and verified in [15]. First figure shows the two scales studied and the next compares the different methods.

FIGURE 21 TURBINE PHYSICAL SCALE MODELS

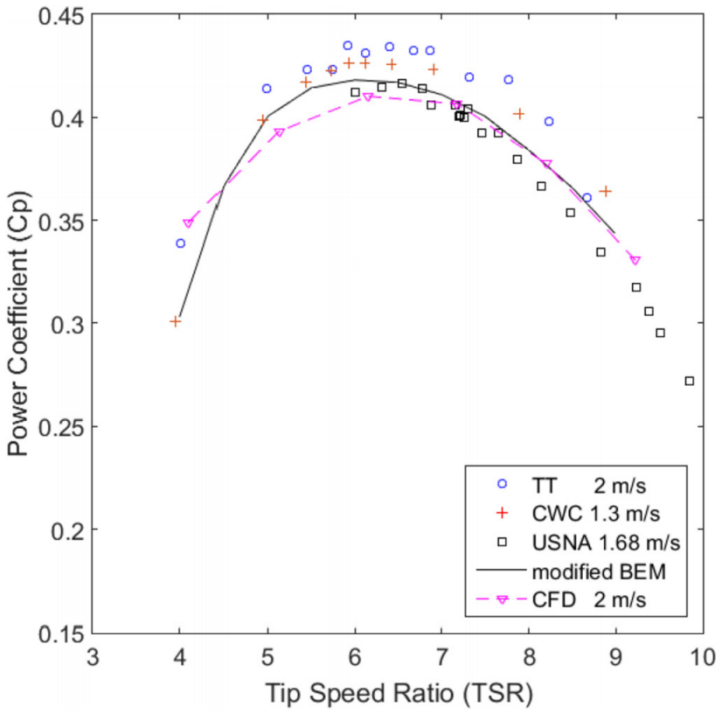

FIGURE 22 COMPARING THE METHODS EMPLOYED FOR PERFORMANCE EVALUATION OF 800 *mm*

Loyd first formulated *Crosswind Power Kite* in [16], more on this in the theory part. A *review* of the *airborne wind energy system* (**AWES**) proposed since is given in [17]. Divided mainly by the *ground-gen* and *fly-gen* types, the first type is further divided into *fixed* or *moving* ground-station types. First figure shows the two main types, the second illustrate the two phases in the ground-gen type.

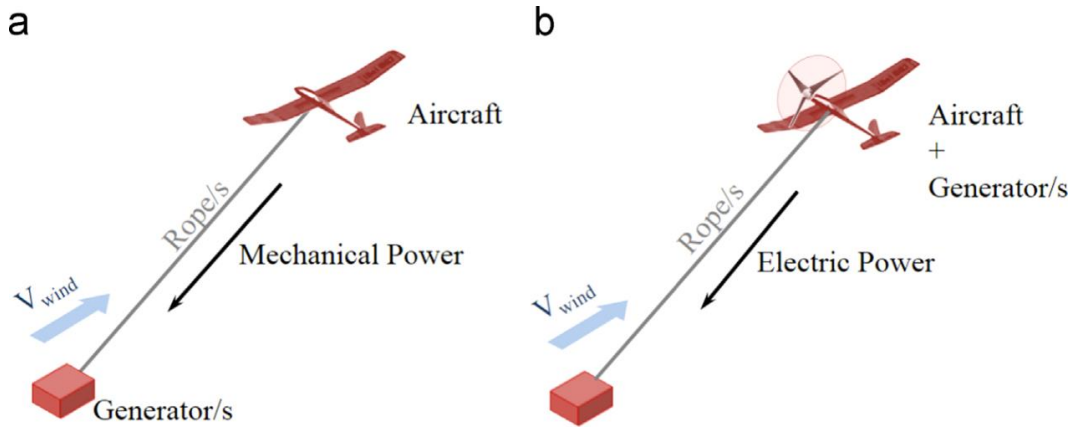

FIGURE 23 EXAMPLE OF GROUND-GEN (A) AND FLY-GEN (B) AWESS

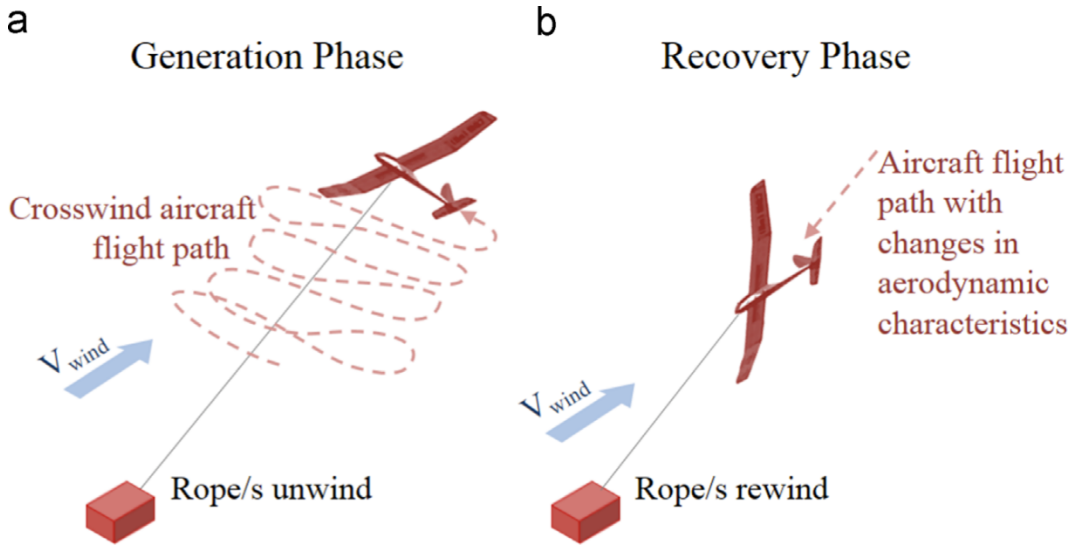

FIGURE 24 SCHEME OF TWO-PHASE DISCONTINUOUS ENERGY PRODUCTION FOR GG AWESS. (A) GENERATION PHASE (UNWINDING) (B) RECOVERY PHASE (REWINDING), CONSUMING MIN ENERGY

First figure below shows three different *moving-ground-station ground-gen* **AWE** proposals. On the left is a vertical axis generator where the axis is fixed with anchors connected to the periphery of the rotor. The middle shows kites grounded on a rail in a closed loop. At last, the kite can pull stations on open loop rails. The second figure shows control mechanism and solutions.

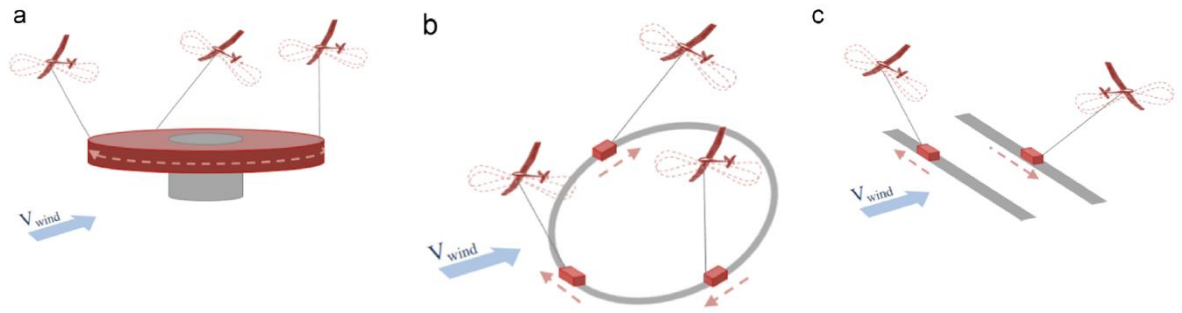

FIGURE 25 SCHEME OF THREE CONCEPTS OF MOVING-GROUND-STATION GG-AWES. (A) VERTICAL AXIS GENERATOR (B) CLOSED LOOP RAIL (C) OPEN LOOP RAIL

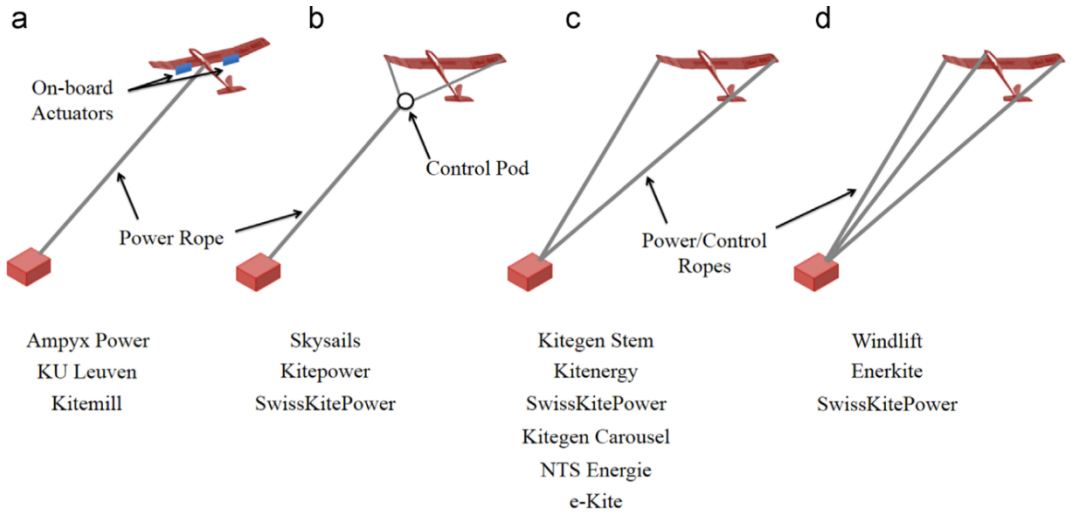

FIGURE 26 CONTROL LAYOUT OF CROSSWIND GG-AWESS. (A) ON-BOARD CONTROL ACTUATORS (B) FLYING CONTROL POD (C) THROUGH POWER ROPES (D) ADDITIONAL CONTROL ROPE

A kite with *onboard* wind turbine flying *crosswind* were studied in [18]. Kite *performance* was first computed *analytically* (iteratively) to plot performance parameters against lift coefficient for small-scale and utility-scale kite. With a 40 m *wingspan* the top figure on the next page shows a 4.1 MW *rated power* assuming a *power density* of 52 kW/m^2.

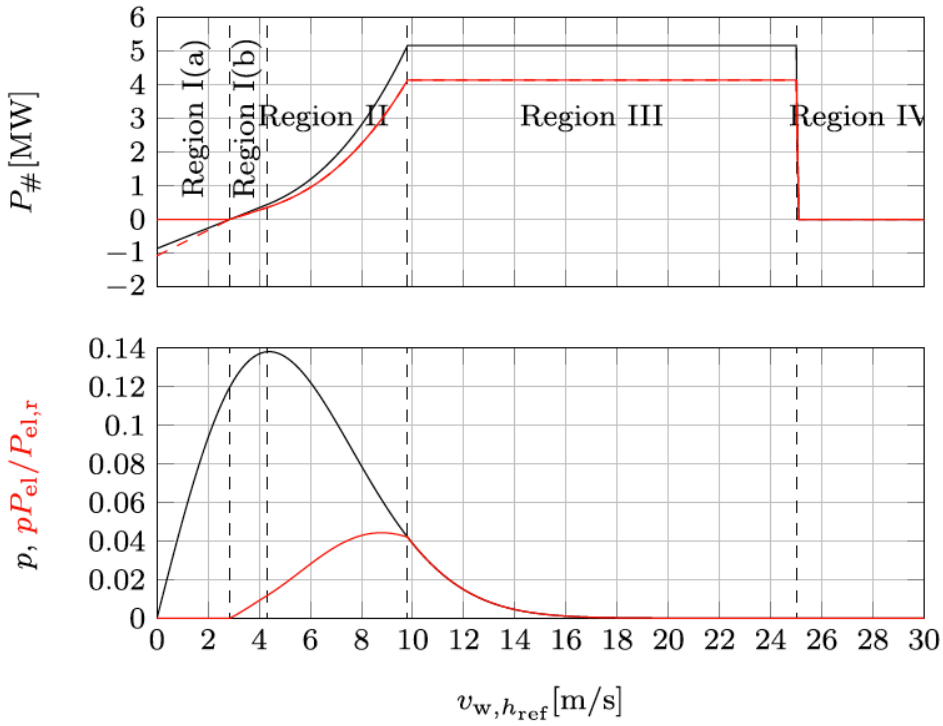

FIGURE 27 POWER CURVE OF THE OPTIMIZED UTILITY-SCALE BIPLANE WITH EXTRACTED POWER P_a IN (−) AND ELECTRICAL POWER P_{el} IN (−) (TOP), AND WIND PROBABILITY DISTRIBUTION p IN (−) AND NORMALIZED ENERGY YIELD DISTRIBUTION $pP_{el}/P_{el,r}$ IN (−) (BOTTOM).

The CFD simulation of monoplane and biplane was compared as shown in figure below. With an optimal lift coefficient of 4.5, the biplane outperforms the monoplane.

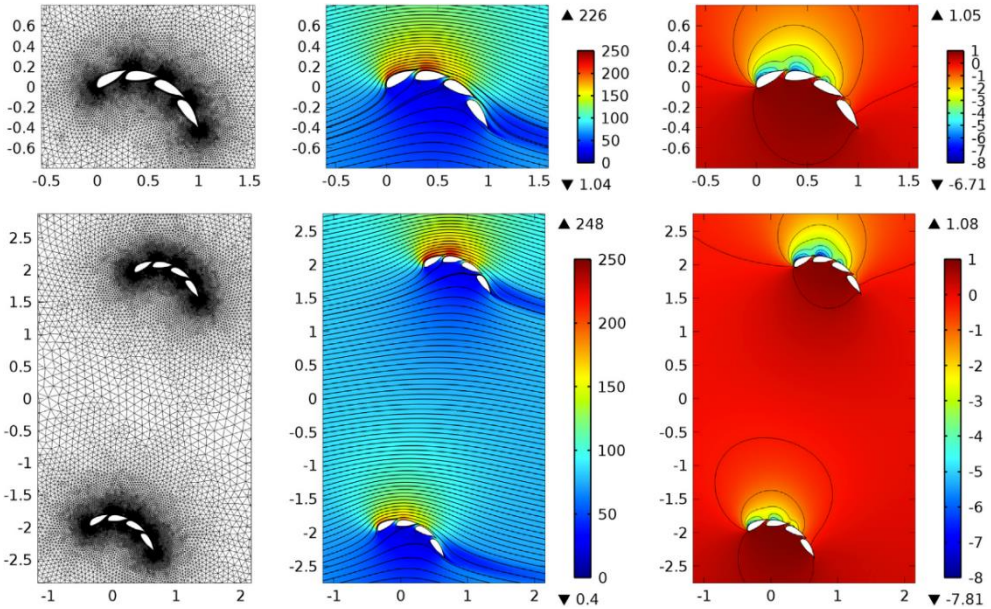

FIGURE 28 CFD RESULTS FOR MONOPLANE CONFIGURATION (TOP) AND BIPLANE CONFIGURATION (BOTTOM): (UNSTRUCTURED) MESH (LEFT), VELOCITY FIELD (MIDDLE) AND PRESSURE COEFFICIENT FIELD (RIGHT). ALL SPACE COORDINATES ARE IN m AND ALL SPEED VALUES ARE IN m/s.

Makani shared their *13-year experience* in [19]. Some of the puzzling findings were the severe underperformance of their latest kite design. **Obtoberkite** was intended as the next iteration after **M600**. First figure shows the *intended* vs the *realized* power output of M600. The second shows the *Force Balance Loop* (**FBL**) optimizer predictions of the Octoberkite vs. M600.

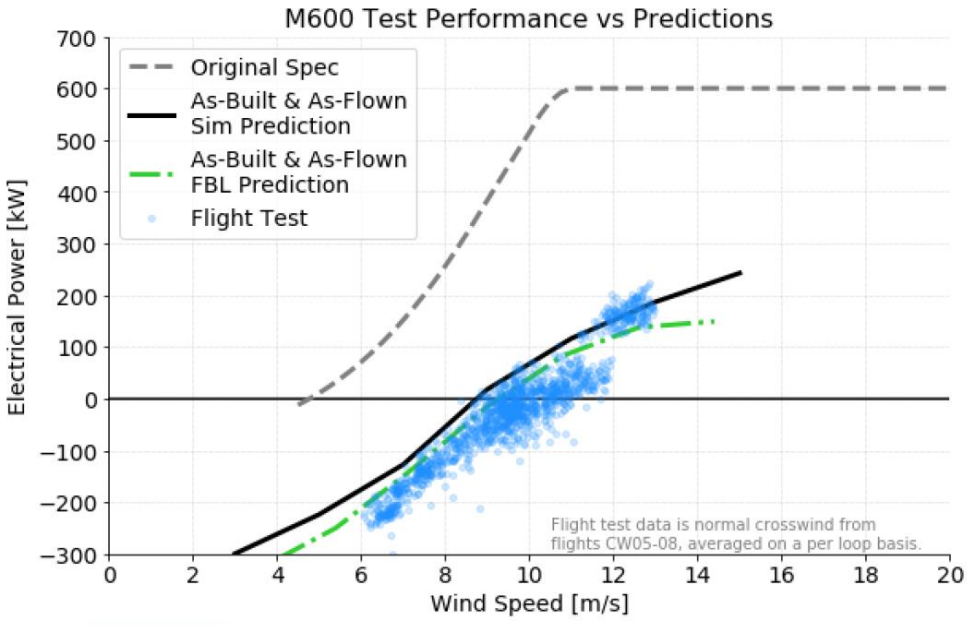

FIGURE 29 POWER CURVE OF M600 TEST VS PREDICTIONS

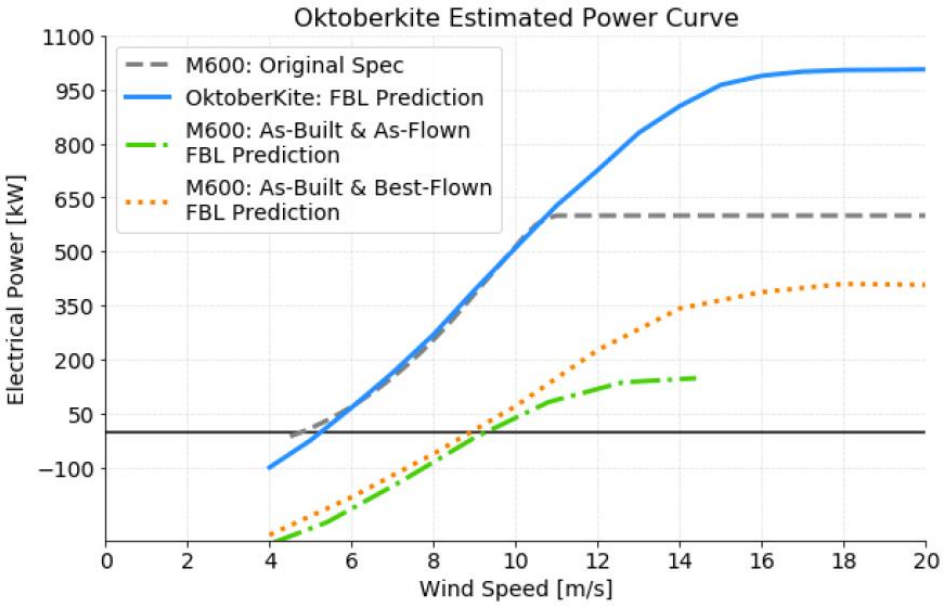

FIGURE 30 POWER CURVE OF M600 VS OCTOBERKITE

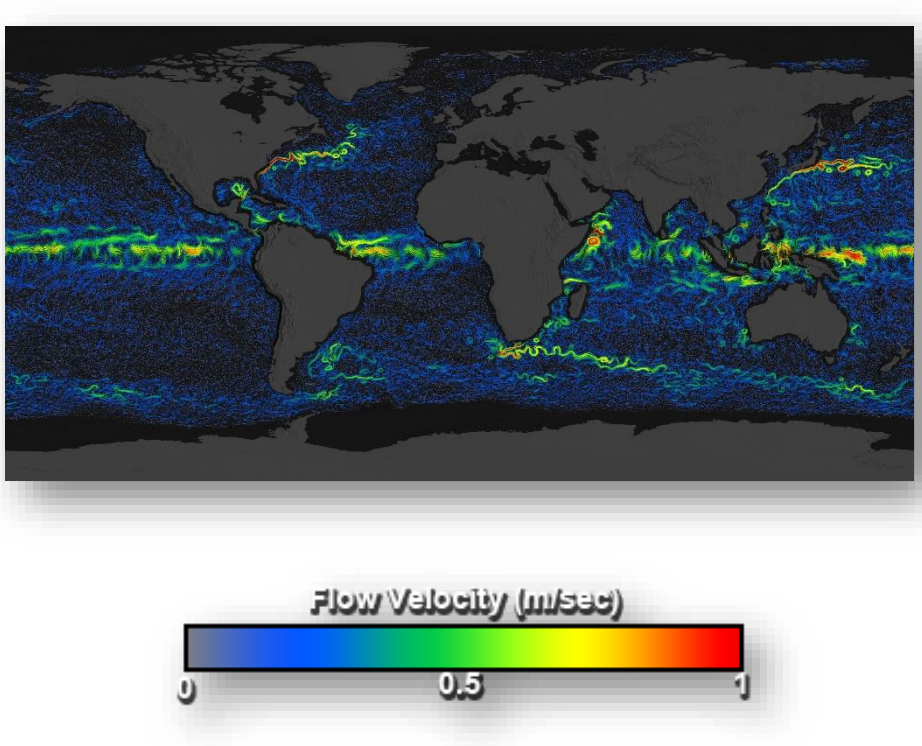

FIGURE 31 OCEAN CURRENT AROUND THE WORLD WITH VELOCITY INDICATED AS COLORS ACCORDING TO THE COLOR BAR

A more resent emergence is the study of *tethered undersea kite* (**TUSK**) systems. The *ocean currents* appear to be relatively untapped resource, and the potential not exhaustively explored, figure above indicate a potential resource [20]. *Worcester Polytechnic Institute* (**WPI**) has performed some relatively comprehensive studies and experimentations. A model-scaled TUSK was designed and tested [21]. Figure below show the isometric and section view of the proposed design.

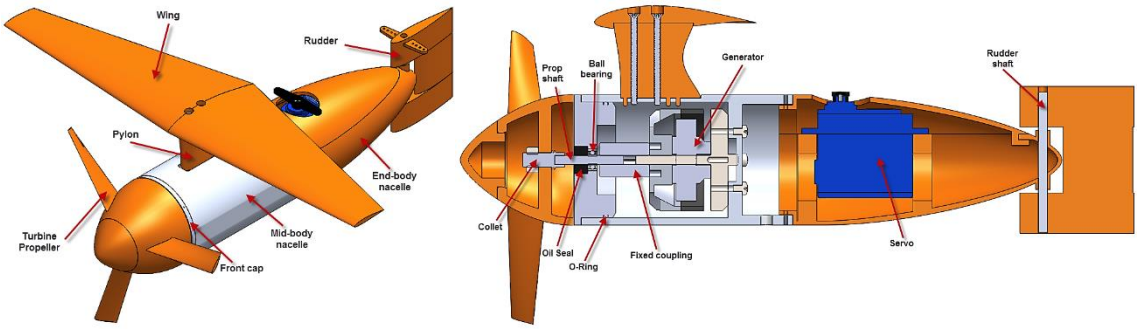

FIGURE 32 ISOMETRIC AND SECTION VIEW OF HYDRO-KITE

A modified concept, s*urface undersea kite* (**SUSK**) was design and tested [22]. Figure below shows side and top views. Small-scale simulation was performed and compared to large-scale simulation as shown in the figure at the bottom of the page.

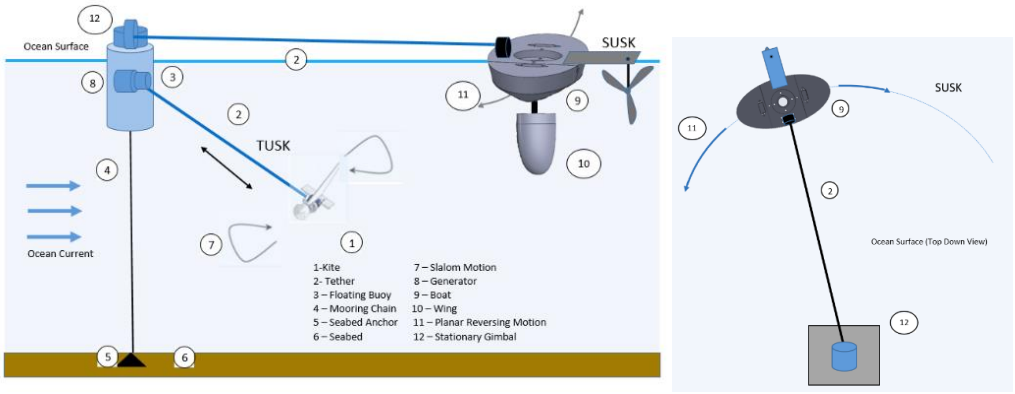

FIGURE 33 COMPARISON OF THE TUSK AND SUSK SYSTEM CONCEPTS

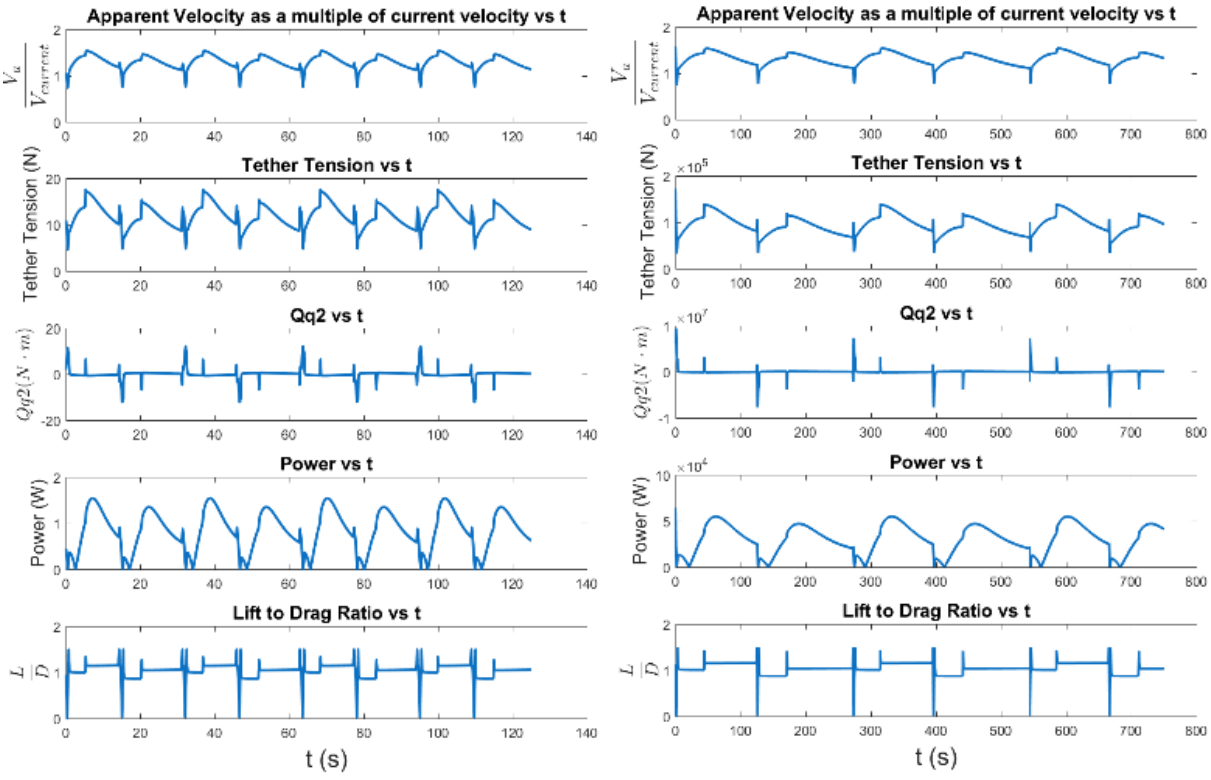

FIGURE 34 SMALL-SCALE SIMULATION (LEFT) AND LARGE-SCALE SIMULATION (RIGHT)

A *modified* **TUSK** design was tested and compared to simulations in [23]. Figures below show the overview of the general system and some maneuverability of the redesign.

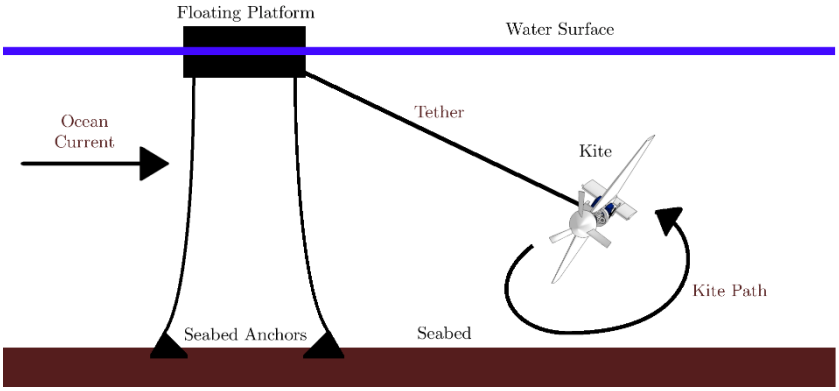

FIGURE 35 OVERVIEW OF THE GENERAL TUSK SYSTEM

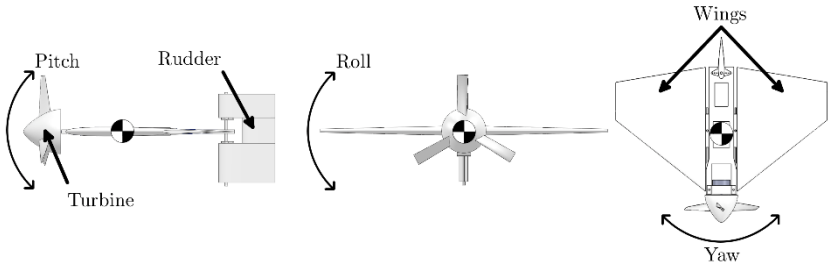

FIGURE 36 ILLUSTRATION OF PITCH, ROLL, AND YAW AXES, ALONG WITH ROTATION CENTERS

Simulations were performed on both the *circular* path and the *figure 8* flight path. *Trajectory* were tracked, *velocity* and *power* measured, as well as parameters like power coefficient, lift-to-drag ratio were logged. Figure below shows only power and velocity for the figure 8 path flight.

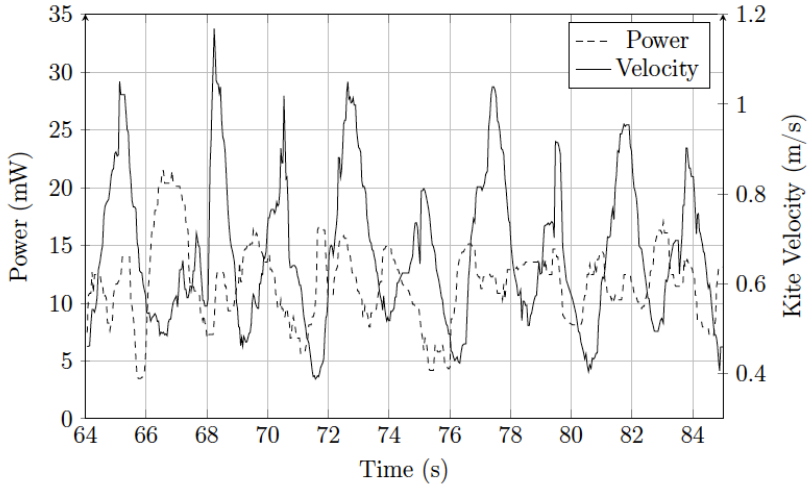

FIGURE 37 POWER AND V_{kite} IN THE KITE BODY REFERENCE FRAME

An elaborate **computational modeling** was developed for the **TUSK** system in [24]. Using a *moving computational domain* coupled with *Open Multi-Processing* (**OpenMP**) a *dynamic model* was built. Figures below show the *computational domain* and the *moving domain*.

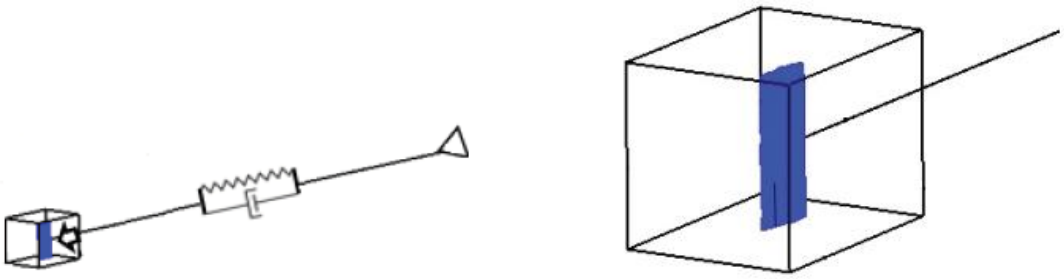

FIGURE 38 SCHEMATIC DIAGRAM OF THE KITE-TETHER SYSTEM IN WHICH THE ATTACHMENT POINT IS OUTSIDE OF THE COMPUTATIONAL DOMAIN, ZOOM-IN VIEW ON THE RIGHT

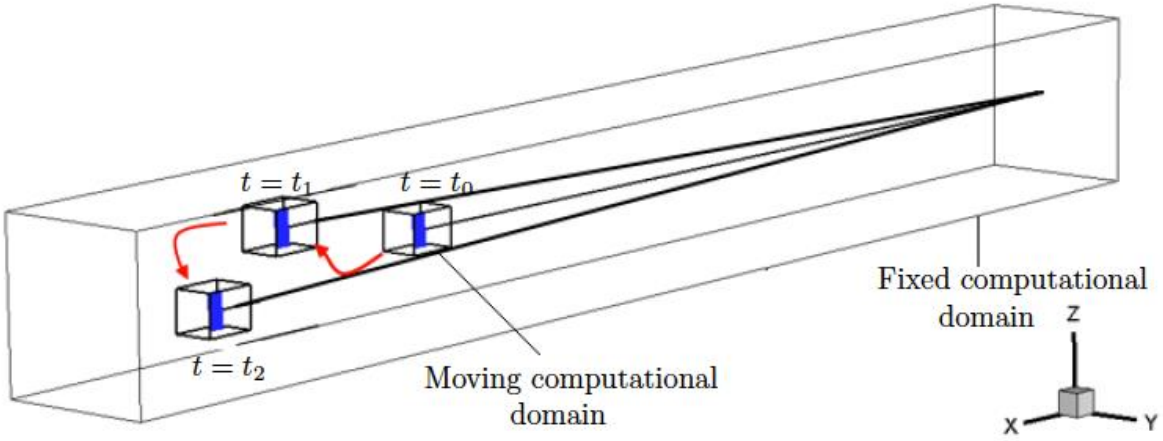

FIGURE 39 SCHEMATIC OF A MOVING COMPUTATIONAL DOMAIN WHICH IS USED IN 3D BASELINE

Figure on the next page shows the kite in its *trajectory* surrounded by *contours* indicating *vorticity*. These so-called nonlinear effects are challenging to capture fully in any turbulence modellings. The figure also shows the *power* phase and *retraction* (or recovery) phase, when the tether length first *increases* and then *reduces*.

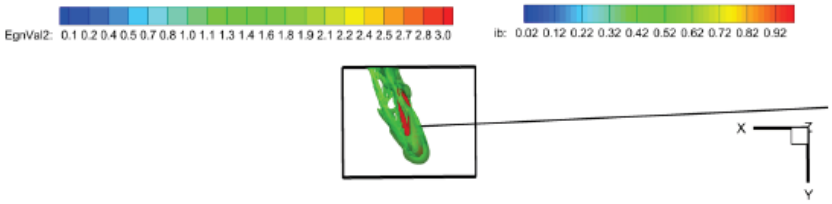

(a) Kite position at 28 s - Power phase.

(b) Kite's position at 44 s - Power phase.

(c) Kite's position at 57 s - Power phase.

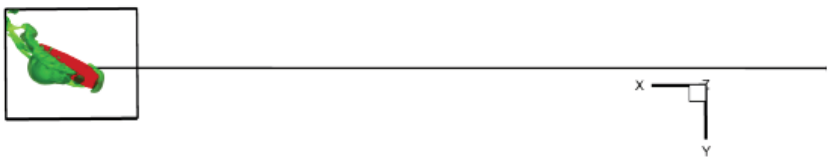

(d) Kite's position at 84 s - Beginning of retraction phase.

(e) Kite's position at 135 s - Retraction phase.

FIGURE 40 TOP VIEW OF THE KITE POSITION WITH FLOW VORTICITY (λ_2) CONTOURS

Figures below track the *trajectory* of kite and the corresponding *pitch*, *roll* and *yaw angle*.

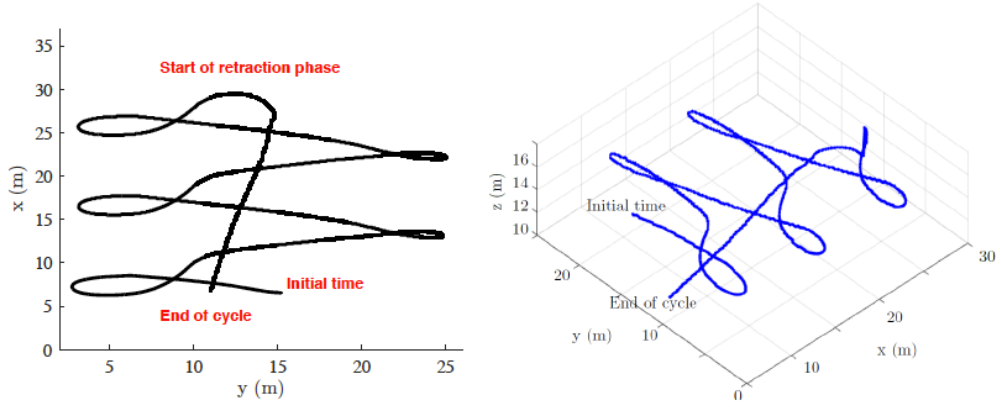

(a) Top view of kite center of mass trajectory. (b) Kite center of mass trajectory in 3D.

FIGURE 41 TRAJECTORY OF KITE CENTER OF MASS VS TIME

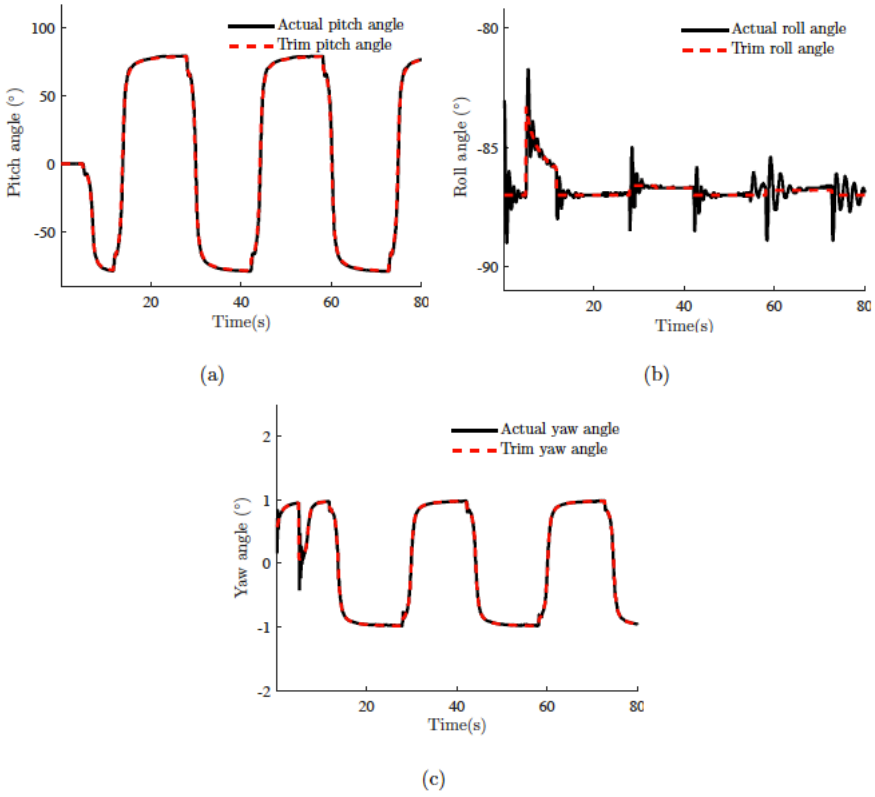

FIGURE 42COMPARISON OF THE ACTUAL AND TRIM KITE ANGLES VS TIME (A) PITCH ANGLE (B) ROLL ANGLE, (C) YAW ANGLE.

Figures below show *lift*, *drag* and *resultant coefficients*, using side-slip condition and no-slip condition. Next figure shows tether *tension* and *velocity*. And power output is shown in the last figure.

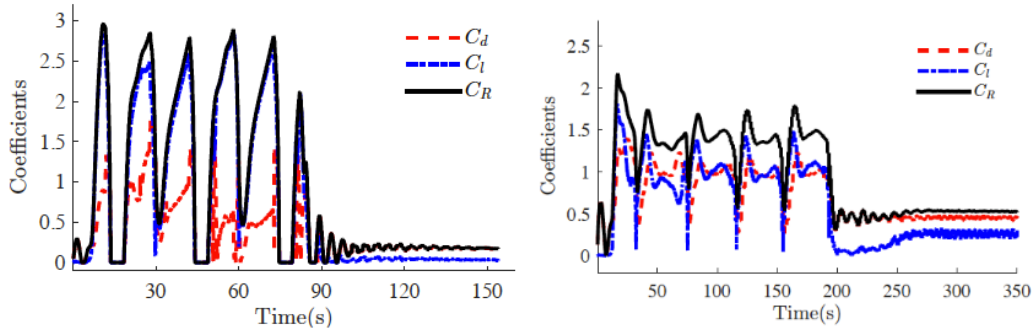

FIGURE 43 LIFT, DRAG, RESULTANT COEFFICIENTS. SIDE-SLIP ON THE LEFT, NO-SLIP ON THE RIGHT

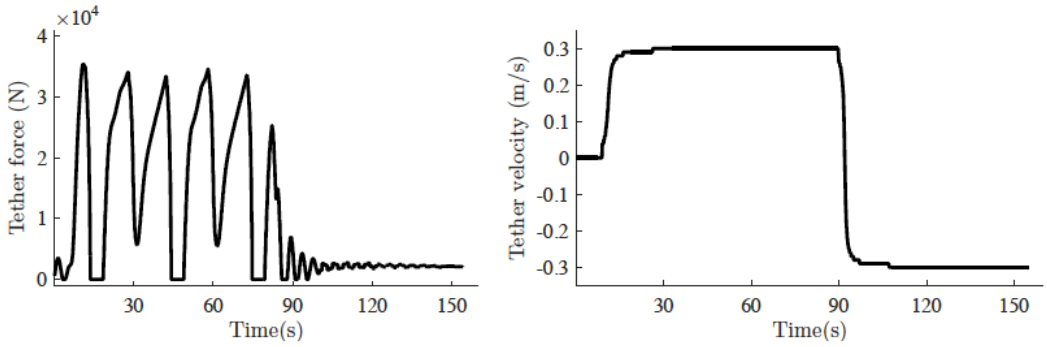

(a) Tether tension vs time. (b) Tether velocity vs time.

FIGURE 44 TETHER PARAMETERS IN THE 3D BASELINE SIMULATION (SLIP)

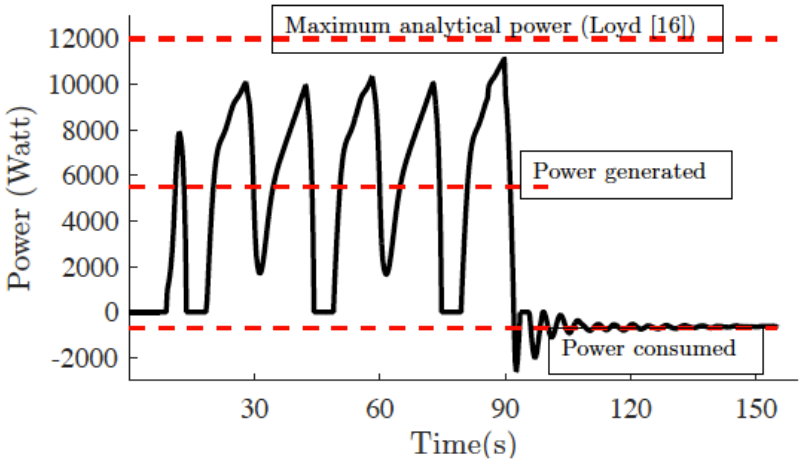

FIGURE 45 POWER OUTPUT OF 3D BASELINE SIMULATION VS TIME

A comprehensive *modelling* and c**ontrol system** was developed for the **TUSK** system in [25]. Figures below show *configuration*, the *translational* and *rotational kinematics* of the **TUSK** system.

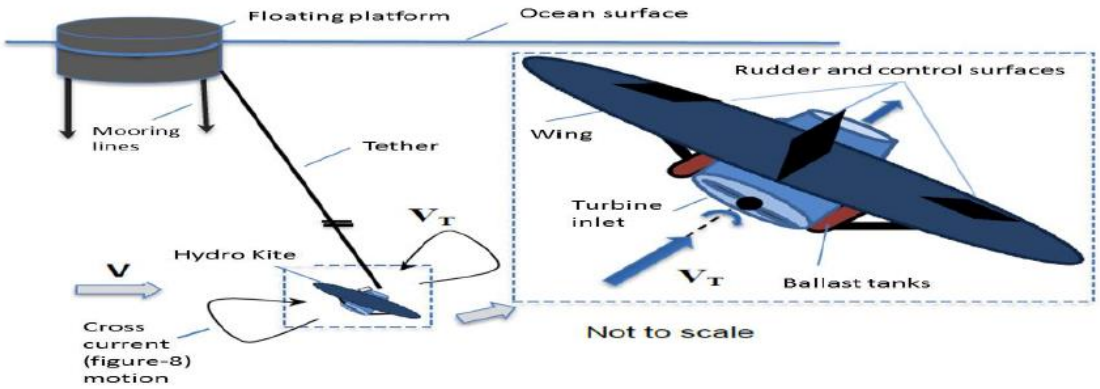

FIGURE 46 SYSTEM CONFIGURATION OF UNDERSEA KITE ENERGY SYSTEM

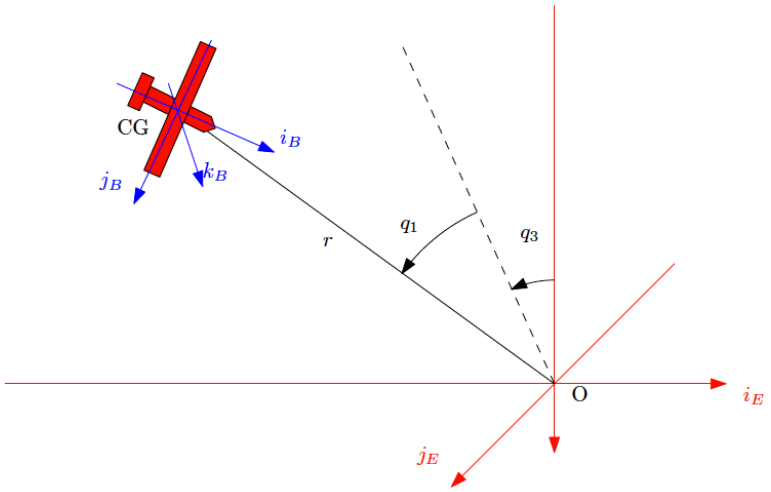

FIGURE 47 KITE TRANSLATIONAL KINEMATICS

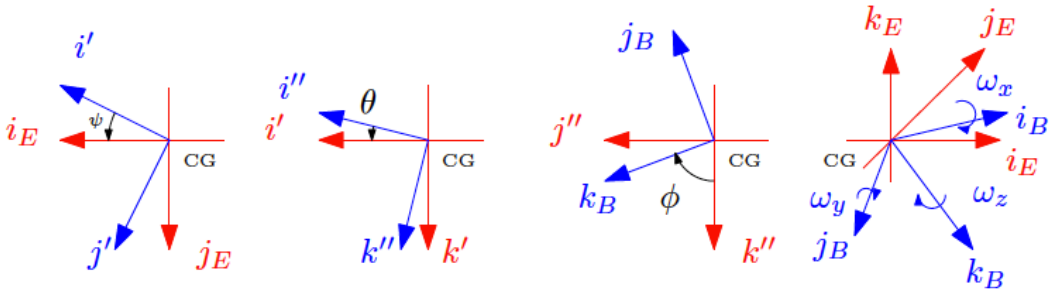

FIGURE 48 KITE ROTATIONAL KINEMATICS

Figure below show c**ontrol parameters** and **power output** for kite flying at wind speed 7 m/s and mass 12 kg. Equivalent to g*round-gen* Mode, mechanical to electrical. Power Output 2.57 kW as shown in table below.

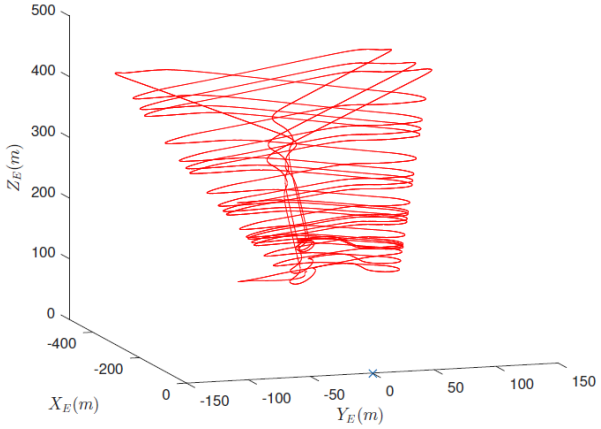

(a) Kite Spherical Coordinate Trajectory

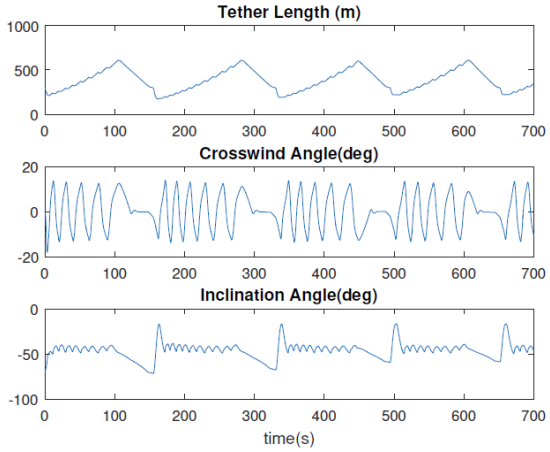

(b) Kite Spherical Coordinate Trajectory

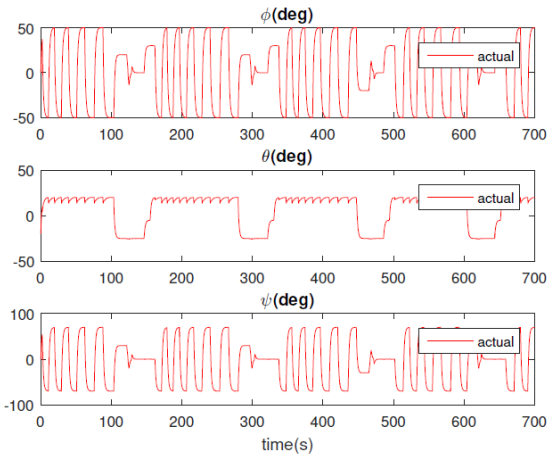

(c) Kite Aerodynamics Coefficient

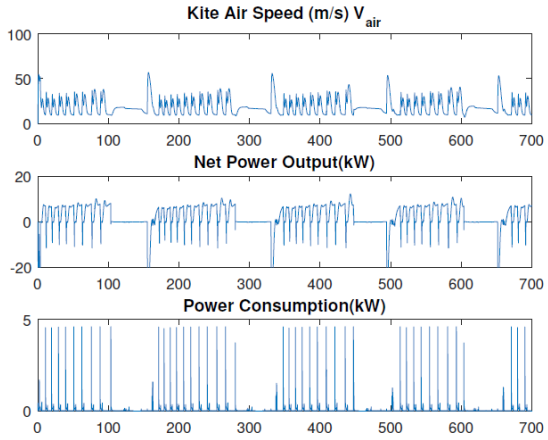

(d) Angle of attack and control tension

FIGURE 49 WIND SPEED = 7 m/s, MASS = 12 kg

TABLE 1 POWER OUTPUT

Wind Speed(m/s)	mass(kg)	Power(kW)
6	12	2.17
	15	2.57
	18	2.56
7	12	2.57
	15	2.58
	18	2.37

Figure below show **control parameters** and **power output** for kite with fixed tether and experiencing current speed 2.5 m/s with mass 3.4 ton. Equivalent to *fly-gen* Mode, apparent wind to power. Power Output 58.06 kW as shown in table below.

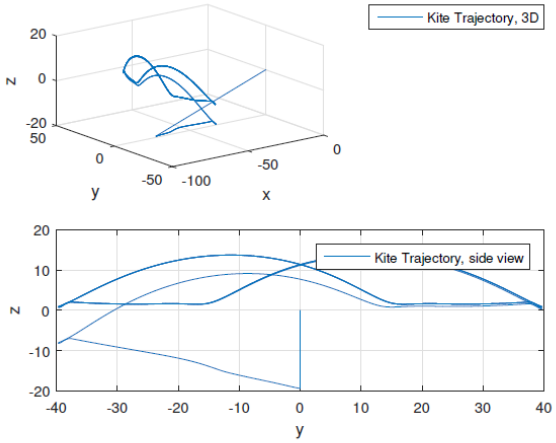

(a) Kite Translational Trajectory

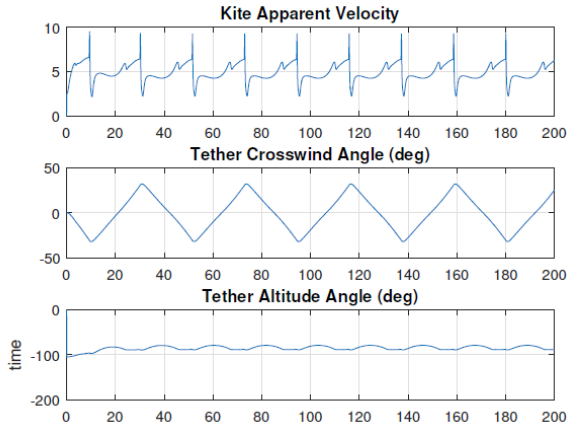

(b) Kite Euler Angles Trajectory

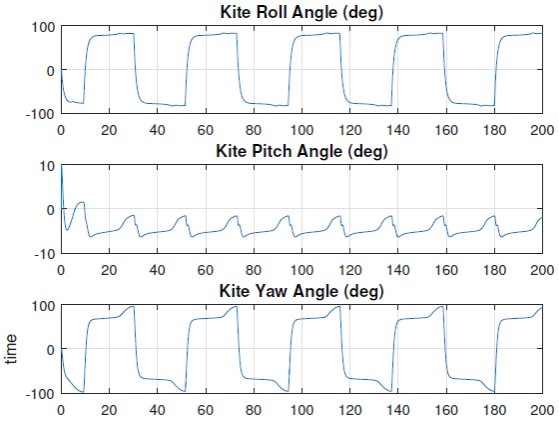

(c) Kite apparent Attitude

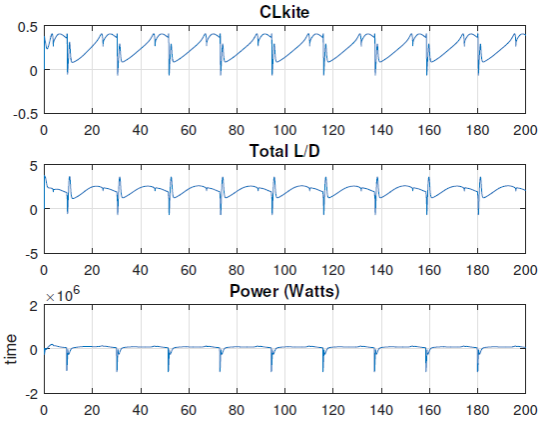

(d) Kite Angular Velocity

FIGURE 50 CURRENT SPEED = 2.5 m/s, MASS = 3.4 ton, AREA = 30 m^2

TABLE 2 POWER OUTPUT

Current Speed(m/s)	Area(m^2)	mass(ton)	Power(kW)
2	30	3.4	31.98
	35	4.0	29.79
	40	4.6	28.27
2.5	30	3.4	58.06
	35	4.0	55.10
	40	4.6	43.42

XFOIL "is an interactive program for the design and analysis of subsonic isolated airfoils" well known for its ability to precisely predict profile coefficients and good agreement with experimental data [26]. First figure below illustrates the *panel method* the **XFOIL** code based its numerical calculations on. The other two figures are validations of the code against experimental measurements, *polar plot* shown in the first and *pressure coefficient* shown the last [27].

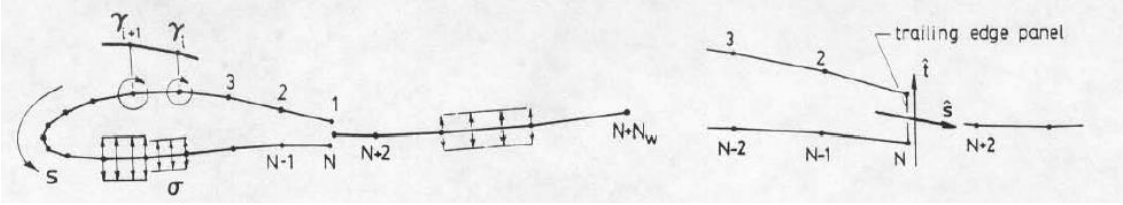

FIGURE 51 AIRFOIL AND WAKE PANELING WITH VORTICITY AND SOURCE DISTRIBUTION

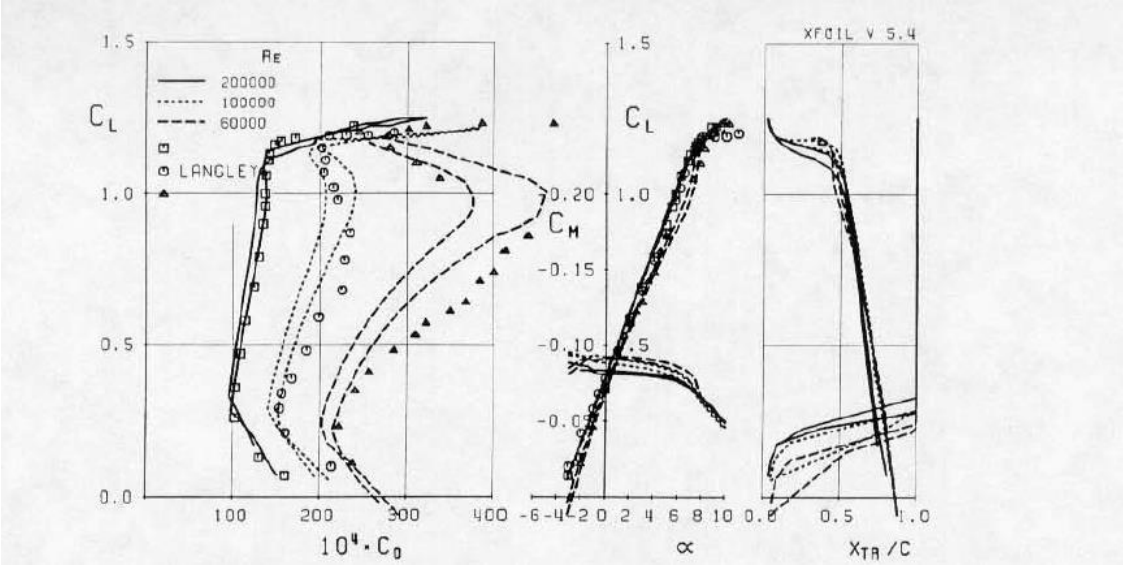

FIGURE 52 CALCULATED AND MEASURED EPPLER 387 POLARS FOR $N_{crit} = 9$

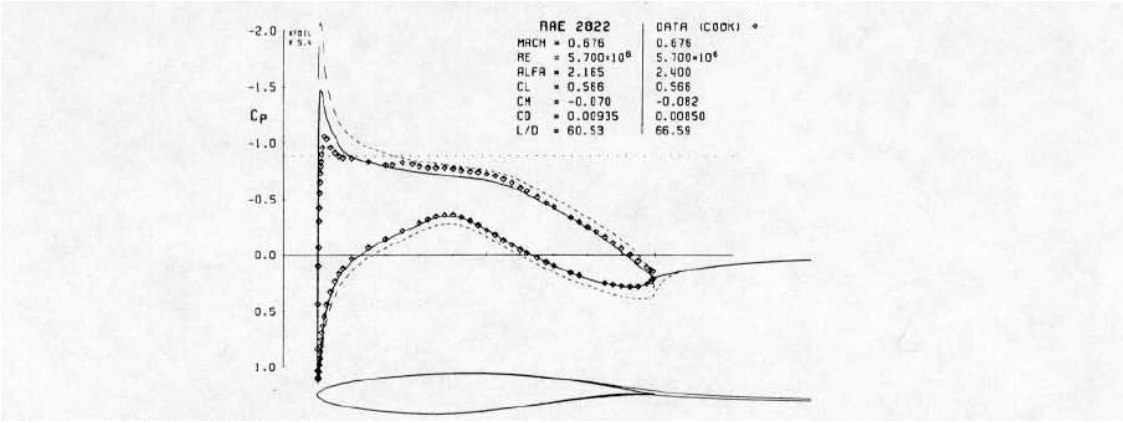

FIGURE 53 CALCULATED AND EXPERIMENTAL RESULTS FOR RAE 2822 AIRFOIL

XFOIL code were compared to **CFD** predictions for high lift low Reynolds number airfoils in [28]. Figures below compares the *polar plot* of the varies turbulence model against *experimental data*.

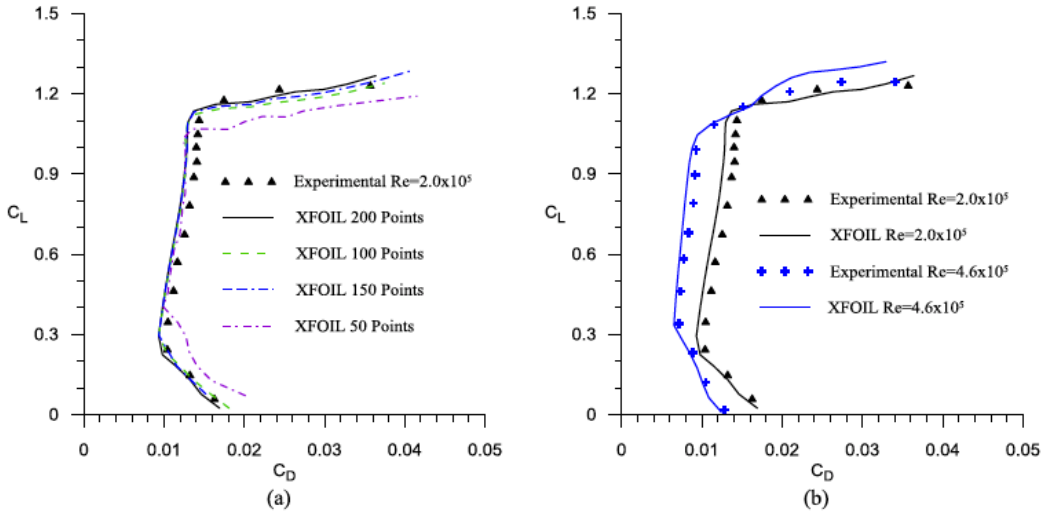

FIGURE 54.(A) VALIDATION OF POLAR CALCULATION USING DIFFERENT NUMBER OF POINTS TO DEFINE AN AIRFOIL IN XFOIL. (B) COMPARISON BETWEEN XFOIL AND EXPERIMENTAL STUDIES [29] FOR E387 AIRFOIL AT DIFFERENT REYNOLDS NUMBERS.

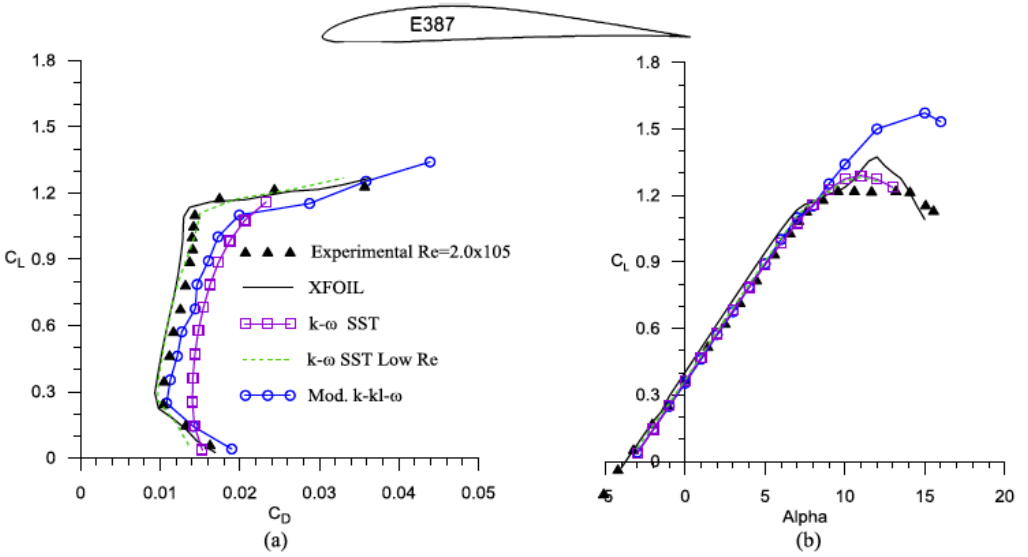

FIGURE 55 AERODYNAMIC CHARACTERISTICS OF THE E387 AIRFOIL MEASURED AT PENN STATE WIND TUNNEL [30] COMPARED WITH THE NUMERICAL SIMULATION RESULTS. (A) C_L VS. C_D (B) C_L VS. α.

A useful collection of many often-used airfoil profiles can be found at **UIUIC** *Airfoil Coordinates Database* [31]. The *National Advisory Committee for Aeronautics* (**NACA**) airfoil profiles, more specifically **NACA63415**, are frequently used in turbines and are often studied.

The $k-\omega$ SST Turbulence model is often used in these *computational fluid dynamic* (**CFD**) studies. A study conducting simulation on **NACA63-415** *airfoil* were performed with one-equation *Spalart-Allmaras* (**SA**), two-equation **RNG** $k-\varepsilon$ and **SST** $k-\omega$ models and *Reynolds Stress Model* (**RSM**) in [32]. Figures below show some of the comparison between the models and experimental data.

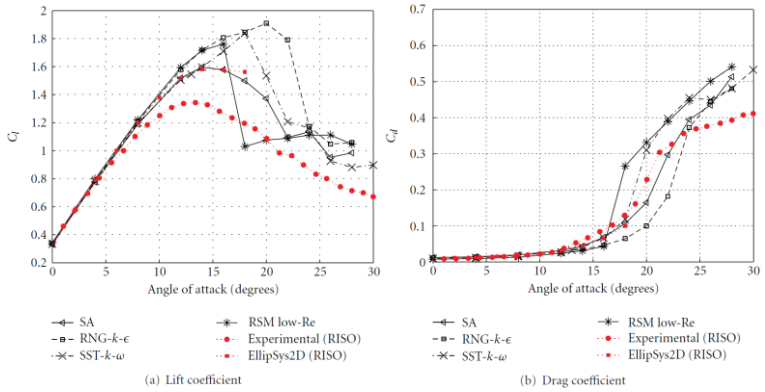

FIGURE 56 COMPARING LIFT AND DRAG COEFFICIENTS

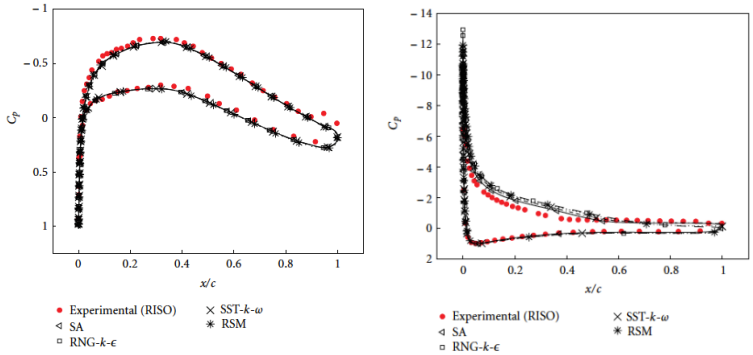

FIGURE 57 PRESSURE COEFFICIENT AT 0°*(LEFT) AND* 16°*(RIGHT)*

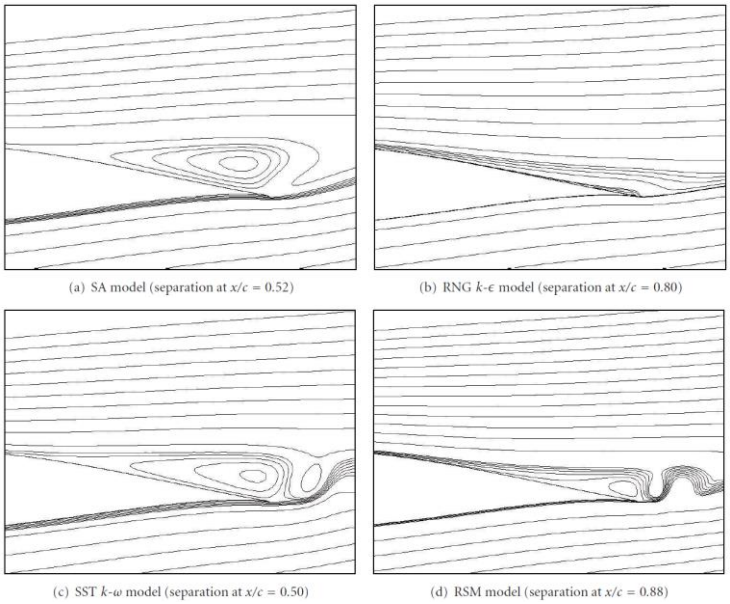

FIGURE 58 STREAMLINES USING VARIOUS TURBULENCE MODELS AT 16°

A similar study with similar *turbulence model* and *airfoil profile* were performed on a 3D **HAWT** *blade* in [33]. Figures below show first the 3D *CAD* model, then the computational *domain* and lastly *pressure coefficient* for various turbulence model at *root*, *midspan* and *blade tip*.

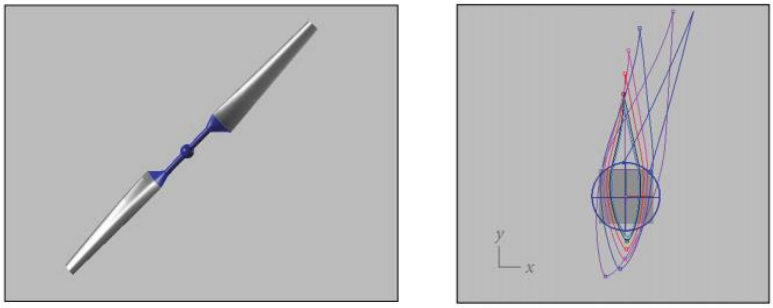

FIGURE 59 3D CAD MODEL OF THE NREL PHASE VI EXPERIMENTAL WIND

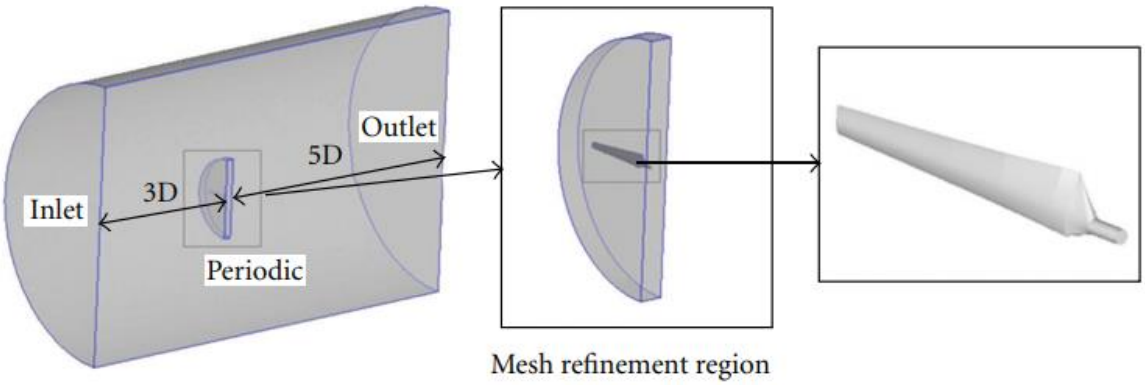

FIGURE 60 COMPUTATIONAL DOMAIN FOR THE NREL PHASE VI ROTOR

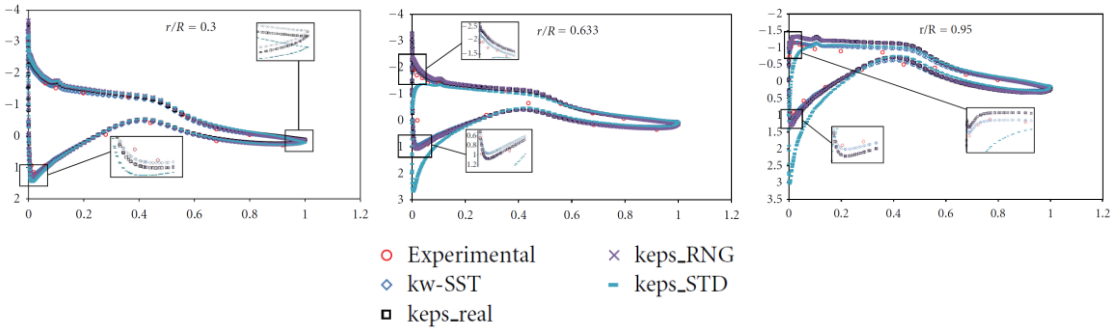

FIGURE 61 COMPARISON OF PRESSURE COEFFICIENTS FOR VARIOUS TURBULENCE MODELS AGAINST EXPERIMENTAL DATA FOR: ROOT, MIDSPAN, AND BLADE TIP

1.3 Objective

This project explores the *tethered undersea kite* (**TUSK**) *energy system* to better understand the *power potential* in the *ocean* or *tidal current*.

How much energy can a flying undersea kite produce?

Using *flow simulation* as a tool this project aims to investigate the *power potential* in the *moving seawater* using a *tethered kite* according to **Loyd's** *crosswind drag powered kite* formulation, *Potsdam Propeller Test Case* (**PPTC**) propeller as the turbine, and the **XFOIL** code as the bases for the validation of *airfoil* and *wing*. The goal is to help **SMART KITE** better understand *flow conditions* around the *propeller* (i.e., the turbine) and the *kite* (i.e., the aerofoil/wing). As a preliminary step, this project aims to be useful in the design work of a functioning prototype and optimisation of future designs.

1.4 Outline

The **theory** part starts with the *theoretical grounding* and the *turbulence modelling* for the flow simulation. It continues with some elaboration about the a**ctuator disk theory** to calculate *power potential* in the *fluid*. Some *differentiations* between the **airfoil** section vs. a finite **wing** follows. Finally, the **Loyd** *formulation* for c**rosswind kite** is presented before *calculations* on the **PPTC** *propeller* as the turbine is performed for the project. The **main** part is separated into two sub-parts, validation of the **propeller** and validation of the **kite**. The latter is further divided into 2D simulation of the **airfoil**, 3D simulation of the **wing** and finally the 3D simulation of the **kite** where wing and propeller is combined. Lastly, **thrust** and **torque** data is extracted from the simulation to produce the **performance** and **power** curves. The report concludes with a **summary** with some final remarks and suggestions for **future works**.

2 Theory

Starting with the **conservation laws** (i.e., conservation of *mass*, *momentum*, and *energy*) we establish the *mathematical foundation* for the flow simulation. When a fluid flows some general *property* ϕ is *transported* by the flow through the mechanism of *convection* and *diffusion*, through *space* and through *time*. When we ignore time and only considers flow through space the flow is seen as being in a *steady state* (i.e., changes in time are negligible relative to changes in space). When time is not ignored the flow is considered *transient* (i.e., changes from one steady-state to another is of relative importance).

2.1 Governing Equations

The **governing equation** is the mathematical statements of the above-mentioned conversation laws. Formulated as the **general transport equation** it is a general-purpose model applicable for multiple uses [34].

$$\rho \frac{\partial \phi}{\partial t} + \rho \, div(\phi \vec{\boldsymbol{u}}) = div(\Gamma \, grad \, \phi) + S_\phi$$

ϕ is the property that is transported, Γ is a constant and S_ϕ is a source term.

Integrate over **Space** (i.e., Control Volume CV or dV)

$$\rho \int_{CV} \frac{\partial \phi}{\partial t} dV + \rho \int_{CV} div(\phi \vec{\boldsymbol{u}}) \, dV = \int_{CV} div(\Gamma \, grad \, \phi) \, dV + \int_{CV} S_\phi \, dV$$

In **words** the equation is, *rate of inflow* of ϕ in CV plus *net rate of outflow* of ϕ in CV due to **convection** equals *net rate of increase* of ϕ in CV due to **diffusion** plus net *rate of increase* of ϕ due to **source** inside CV.

Using Gauss's divergence theorem $\int_{CV} div(\vec{\boldsymbol{F}}) \, dV = \int_A \vec{\boldsymbol{n}} \cdot \vec{\boldsymbol{F}} \, dA$. Flux out of a *surface* equals reduction in the *volume* (encapsulated by the surface).

$$\rho \frac{\partial}{\partial t} \left(\int_{CV} \phi \, dV \right) + \rho \int_A \vec{\boldsymbol{n}} \cdot (\phi \vec{\boldsymbol{u}}) \, dA = \int_A \vec{\boldsymbol{n}} \cdot (\Gamma \, grad \, \phi) \, dA + \int_{CV} S_\phi \, dV$$

In **words** the equation is, *rate of increase* over time of ϕ inside CV plus *net rate of decrease* of ϕ over CV surface due **convection** equals *net rate of increase* of ϕ over CV surface due to **diffusion** plus net rate of **creation** of ϕ inside CV.

Integrate over **Time** (i.e., discretized time step Δt)

$$\rho \int_{\Delta t} \frac{\partial}{\partial t}\left(\int_{CV} \phi \, dV \right) dt + \rho \int_{\Delta t} \int_{A} \vec{\boldsymbol{n}} \cdot (\phi \vec{\boldsymbol{u}}) \, dA \, dt$$
$$= \int_{\Delta t} \int_{A} \vec{\boldsymbol{n}} \cdot (\Gamma \, grad \, \phi) \, dA \, dt + \int_{\Delta t} \int_{CV} S_{\phi} \, dV \, dt$$

Solving the set of equation above will results in **velocity** (vector) **field** and **pressure** (scalar) **field**. **Turbulence** is the *fluctuation* around a trending *average* of velocity, defined as the *turbulence kinetic energy per unit mass* k, can be derived from these fields, same for *dissipation rate* ε, *turbulence frequency* ω and eddy viscosity μ_t.

The **Mass** of is conserved in a fluid flow (i.e., continuity condition).

$$\rho \cdot \nabla \cdot \vec{\boldsymbol{u}} = 0$$

The rate of change of **Momentum** equals the sum of forces on a fluid particle (i.e., Newton's 2nd Law).

$$\rho \left(\frac{\partial \vec{\boldsymbol{u}}}{\partial t} + \vec{\boldsymbol{u}} \cdot \nabla \cdot \vec{\boldsymbol{u}} \right) = \mu \nabla^2 \vec{\boldsymbol{u}} + \vec{\boldsymbol{S}}$$

The fluid is considered incompressible so **density** ρ is considered a constant (i.e., do not change in space or time) and can be placed outside any *differentiation* ∇ or *integration* $\int$ operations. Note also that **viscosity** μ is considered a constant as well.

Integrate over T**ime** and **Space**:

$$\rho \int_{\Delta t} \frac{\partial}{\partial t}\left(\int_{CV} \vec{\boldsymbol{u}} \, dV \right) dt + \rho \int_{\Delta t} \int_{A} \vec{\boldsymbol{n}} \cdot (\vec{\boldsymbol{u}} \cdot \vec{\boldsymbol{u}}) \, dA \, dt$$
$$= \int_{\Delta t} \int_{A} \vec{\boldsymbol{n}} \cdot (\mu \, grad \, \vec{\boldsymbol{u}}) \, dA \, dt + \int_{\Delta t} \int_{CV} S_{\phi} \, dV \, dt$$

Energy is also assumed conserved but not explicitly solved.

2.2 Turbulence Model

The randomness and unpredictability of turbulent flow makes it difficult to model and simulate. *Direct Numerical Simulation* (**DNS**) is computationally costly and demands high resolution both in *space* and *time*. Two simplification and approximation methods are well known, each with its own compromise and priorities. *Large Eddy Simulation* (**LES**) put an emphasis on the large eddies which carry most of the energy and *Reynolds Average Navier-Stokes* (**RANS**) disregard the fluctuation and concentrate more on the *average* variation. This project will use the latter method [34]. Figure below shows how flow transitions into turbulent flow.

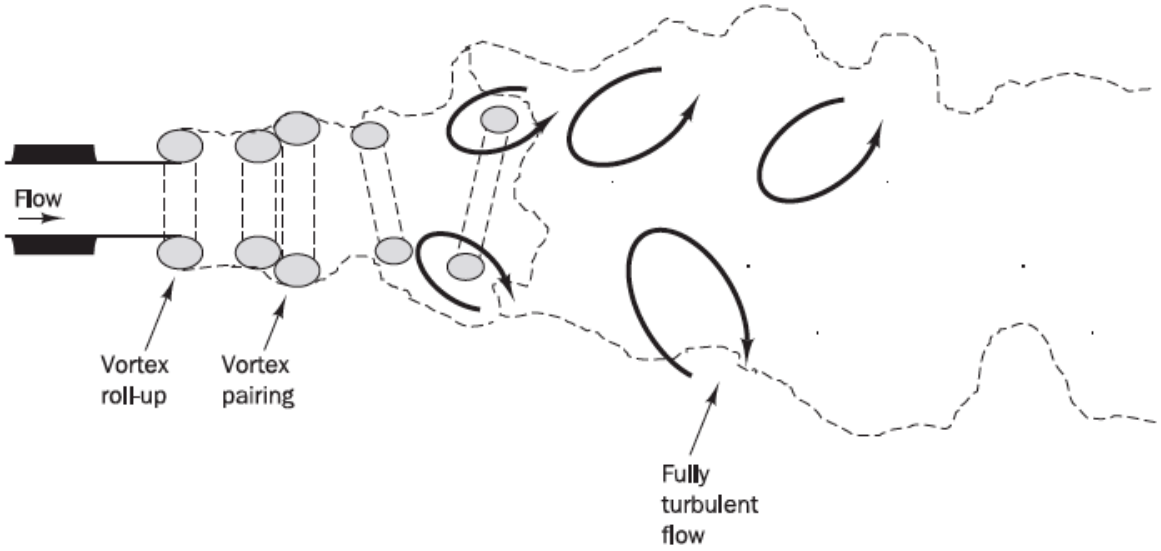

FIGURE 62 TRANSITION OF TURBULENT FLOW [34, P. 46]

2.2.1 RANS Modelling

Assuming that the randomness of turbulence can be decomposed into a steady mean $\bar{u}$ and a fluctuation around this mean u', the velocity u can be expressed.

$$u = \bar{u} + u'$$

The expression is known as the *Reynolds Decomposition*. The figure below is an illustration of the *randomness*, the *time-average* and the *fluctuation* around the *mean*.

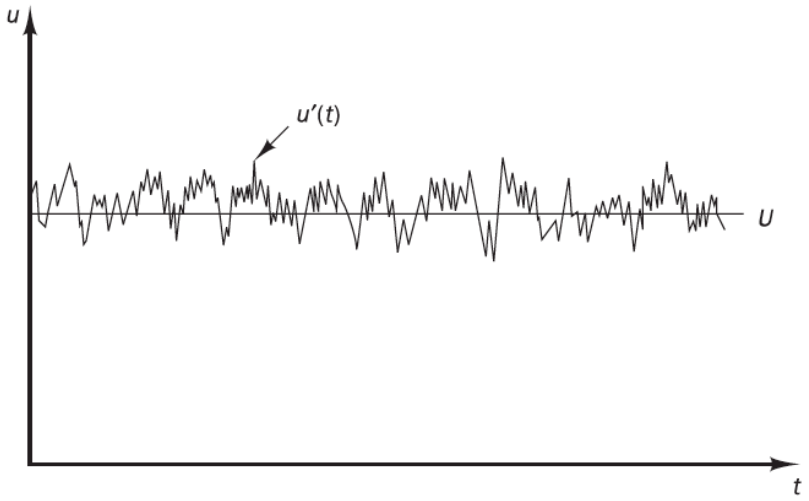

FIGURE 63 TYPICAL POINT VELOCITY MEASUREMENT IN TURBULENT FLOW [34, P. 41]

These fluctuations give rise to additional stresses in the flow known as *Reynolds Stresses*.

$$\tau_{ij} = -\rho\overline{u_i' u_j'} = \begin{bmatrix} \rho\overline{u'^2} & \rho\overline{u'v'} & \rho\overline{u'w'} \\ \rho\overline{v'u'} & \rho\overline{v'^2} & \rho\overline{v'w'} \\ \rho\overline{w'u'} & \rho\overline{w'v'} & \rho\overline{w'^2} \end{bmatrix}, \qquad s_{ij} = \begin{bmatrix} s_{xx} & s_{xy} & s_{xz} \\ s_{yx} & s_{yy} & s_{yz} \\ s_{zx} & s_{zy} & s_{zz} \end{bmatrix}$$

Analogous to *Viscous Stress*

$$\tau_{ij} = \mu s_{ij} = \mu\left(\frac{\partial u_i}{\partial x_j} + \frac{\partial u_j}{\partial x_i}\right)$$

2.2.2 Boussinesq Approximation

Assuming that Reynolds Stresses can be expressed proportional to the *mean rate of deformation*.

$$\tau_{ij} = -\rho\overline{u_i' u_j'} = \mu_t\left(\frac{\partial U_i}{\partial x_j} + \frac{\partial U_j}{\partial x_i}\right) - \frac{2}{3}\rho k \delta_{ij}$$

$\boldsymbol{\mu_t}$ is known as *turbulent or eddy viscosity* (dimensions $Pa \cdot s$) and $\boldsymbol{k}$ is t*urbulent kinetic energy* per unit mass.

$$k = \frac{1}{2}\left(\overline{u'^2} + \overline{v'^2} + \overline{w'^2}\right) \; with \; dimension \left[\frac{J}{kg} = \frac{Nm}{kg} = \frac{\frac{kg}{m/s^2}\cdot m}{kg} = \frac{m^2}{s^2}\right]$$

Analogous to *heat diffusion* (or *mass diffusion*)

$$-\rho\overline{u_i' \phi'} = \Gamma_t \frac{\partial \Phi}{\partial x_i}$$

$\boldsymbol{\Gamma_t}$ is known as *turbulent* or *eddy diffusivity*.

Introducing the *Prandtl/Schmidth Number*

$$\sigma_t = \frac{\mu_t}{\Gamma_t}$$

experiments have shown that this ratio is often nearly close to constant.

Since dissipation of both **mass** and **momentum** is cause by *eddy mixing*, σ_t is usually assumed close to unity (≈ 1) in most models. This assumption is known as the *Reynolds Analogy*.

2.3 $k-\epsilon$ model

In the standard formulation of this model *turbulent kinetic energy* $\mathbf{k}$ (m^2/s^2) and *rate of dissipation* $\boldsymbol{\varepsilon}$ $(m^2/s^2/s)$ was used to define the *velocity scale* ϑ and *length scale* ℓ.

$$\vartheta = k^{1/2}, \qquad \ell = \frac{k^{3/2}}{\varepsilon}$$

Eddy viscosity depends only on *k* and *ε*

$$\mu_t = C\rho\vartheta\ell = \rho C_\mu \frac{k^2}{\varepsilon}, \qquad C_\mu = \ dim.less\ model\ const.$$

Transport equation for **k**

$$\rho\frac{\partial \boldsymbol{k}}{\partial t} + \rho\ div(k\bar{U}) = div\left(\left(\mu + \frac{\mu_t}{\sigma_k}\right) grad\ \boldsymbol{k}\right) + 2\mu_t(S_{ij}\cdot S_{ij}) - \rho\boldsymbol{\varepsilon}$$

Transport equation for $\boldsymbol{\varepsilon}$

$$\rho\frac{\partial \boldsymbol{\varepsilon}}{\partial t} + \rho\ div(\boldsymbol{\varepsilon}\bar{U}) = div\left(\left(\mu + \frac{\mu_t}{\sigma_\varepsilon}\right) grad\ \boldsymbol{\varepsilon}\right) + C_{1\varepsilon}\frac{\boldsymbol{\varepsilon}}{k}2\mu_t(S_{ij}\cdot S_{ij}) - C_{2\varepsilon}\rho\frac{\boldsymbol{\varepsilon}^2}{k}$$

In **words** the equations are, *rate of change* of k and *ε* plus transport of k and *ε* by *convection* equals transport of k and *ε* by *diffusion* plus the difference between rate of *production* and *destruction* of k and *ε*.

$$C_\mu = 0.09, \qquad \sigma_k = 1.00, \qquad \sigma_\varepsilon = 1.30, \qquad C_{1\varepsilon} = 1.44, \qquad C_{2\varepsilon} = 1.92$$

Rough approximation for initial values for *k* and *ε* can be obtained from assumptions about *turbulence intensity* T_i and *characteristic length* L.

$$k = \frac{3}{2}(U_{ref}T_i)^2, \qquad \varepsilon = C_\mu^{3/4}\frac{k^{3/2}}{\ell}, \qquad \ell = 0.07L$$

It is useful to note the limitation of k − ε model in the transport equation for ε where flow experience very large rates of deformation S_{ij}. The model becomes less precise for aerodynamic simulations. The k − ω and especially SST k − ω was developed to correct for some of these unsatisfactory limitations.

2.4 $k-\omega$ model

Wilcox introduced *turbulence frequency* $\boldsymbol{\omega} = \frac{\varepsilon}{k}$ *with dimension* $[s^{-1}$ *or* $Hz]$. Length scale becomes $\ell = \frac{\sqrt{k}}{\omega}$. And eddy viscosity becomes $\mu_t = \frac{\rho k}{\omega}$, a function of k and ω. Using Boussinesq expression for *Reynold's Stresses* as before. The transport equations for k and ω for turbulent flow with high *Reynold's Number* becomes:

$$\rho \frac{\partial \boldsymbol{k}}{\partial t} + \rho\, div(\boldsymbol{k}\bar{U}) = div\left[\left(\mu + \frac{\mu_t}{\sigma_k}\right) grad\,(\boldsymbol{k})\right] + P_k - \beta^* \rho k \omega$$

and

$$\rho \frac{\partial \boldsymbol{\omega}}{\partial t} + \rho\, div(\boldsymbol{\omega}\bar{U}) = div\left[\left(\mu + \frac{\mu_t}{\sigma_\omega}\right) grad\,(\boldsymbol{\omega})\right] + P_\omega - \beta_1 \rho \boldsymbol{\omega}^2$$

where

$$P_k = \left(2\mu_t S_{ij} \cdot S_{ij} - \frac{2}{3}\rho k \frac{\partial U_i}{\partial x_j}\delta_{ij}\right), \qquad P_\omega = \gamma_1 \left(2\rho S_{ij} \cdot S_{ij} - \frac{2}{3}\rho\omega \frac{\partial U_i}{\partial x_j}\delta_{ij}\right)$$

In **words** the equations are, *rate of change* of k and ε plus transport of k and ω by *convection* equals transport of k and ω by *diffusion* plus the difference between rate of *production* and *destruction* of k and ω.

$$\sigma_k = 2.0, \qquad \sigma_\omega = 2.0, \qquad \gamma_1 = 0.533, \qquad \beta_1 = 0.075, \qquad \beta^* = 0.09$$

Somewhat problematic in this model is the boundary condition of ω in the free stream where turbulence kinetic energy $k \to 0$ and turbulence frequency $\omega \to 0$ and therefore eddy viscosity $\mu_t \to \infty$ and cannot be determined. To use non-zero value of ω for **free stream** is unsatisfactory in external aerodynamic and aerospace application where determination of free stream boundary conditions (i.e., **initial values**) are routinely used. Shear Stress Transport or SST $k-\omega$ model is therefore considered an improvement. SST $k-\omega$ model combines the two previous models. Using the $k-\omega$ near the wall and $k-\varepsilon$ in the free stream. A description of the **Law of the Wall** might be useful to better understand the challenges modelling flow near the wall.

2.5 Law of the Wall

Close to the wall the flow is dominated by *viscous forces*. Father away by *inertia forces*, as illustrated by the figure on the right.

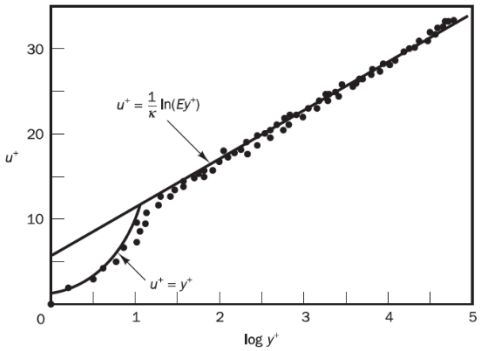

FIGURE 64 VELOCITY DISTRIBUTION NEAR WALL [43]

Law of the Wall:

$$u^+ = \frac{U}{u_\tau} = f\left(\rho \frac{u_\tau}{\mu} y\right) = f(y^+)$$

Introducing two dimensionless groups, u^+ and y^+ and defining wall shear stress τ_w as function of the *distance from the wall* y and friction velocity u_τ (velocity scale appropriate close to the wall).

$$\tau(y) = \mu \frac{\partial U}{\partial y} \cong \tau_w, \qquad u_\tau = \sqrt{\tau_w/\rho}$$

Where the fluid layer is in contact with the wall, the flow velocity U is determined by y in the **viscos sub-layer** $(y^+ < 5)$.

$$U = \frac{\tau_w}{\mu} \cdot y$$

Velocity-defect Law:

$$\frac{U_\infty - U}{u_t} = g\left(\frac{y}{\delta}\right)$$

The degree of velocity deficiency $U_\infty - U$ is dependent on the distance from the wall relative to the boundary layer thickness δ. The wall shear stress causes the velocity to slow down linearly, i.e., u is proportional to y.

$$u^+ = y^+$$

Beyond this region, in the **log-law layer** $(30 < y^+ < 500)$, the viscous effect becomes less influential.

$$u^+ = \frac{1}{\kappa}\ln(y^+) + B = \frac{1}{\kappa}\ln(Ey^+)$$

In the **outer region** the viscous effect is diminished, and inertia forces are taking over. *Law of the Wake*:

$$\frac{U_\infty - U}{u_t} = -\frac{1}{\kappa}\ln\left(\frac{y}{\delta}\right) + A$$

2.5.1 Boundary Layer Thickness – δ

The thickness of the boundary layer δ is dependent on the flow regime (laminar or turbulent) and the skin friction of the surface C_f, which in turn is dependent on the flow regime (i.e., local Re). There is therefore no straightforward way to calculate the boundary layer thickness without knowing the flow regime, and in turn no direct way to calculate y^+.

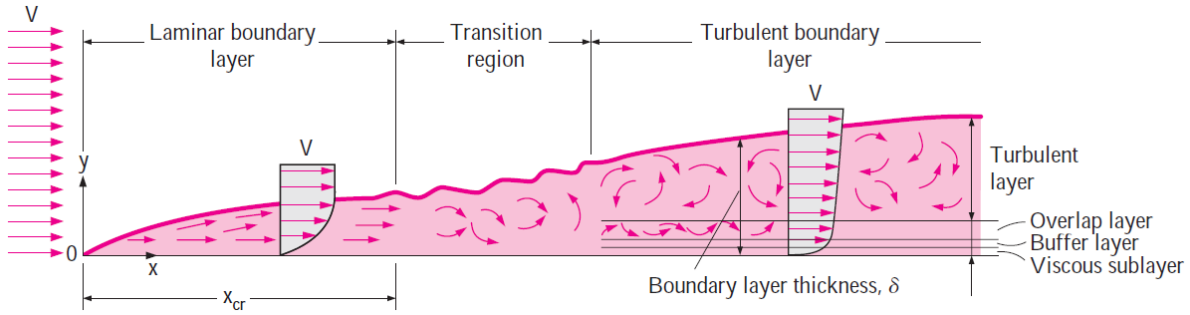

FIGURE 65 THE DEVELOPMENT OF THE BOUNDARY LAYER FOR FLOW OVER A FLAT PLATE, AND THE DIFFERENT FLOW REGIMES. NOT TO SCALE [35].

2.5.2 yPlus – y^+

A useful estimate of the distance to the first node of the mesh if a desired y^+ value is decided on is proposed by *Leading Engineering Application Providers* (**LEAP**) [36].

$$\Delta y = L \cdot y^+ \cdot \sqrt{74} \cdot Re_L^{-13/14}$$

Figure on the right illustrate the two different assumptions or model about the flow close to the wall. The two blue lines intersect at $y^+ = 11$, there is a buffer or transition zone around this point where neither model fully capture the flow entirely. Table below is a summary using the formula mentioned above.

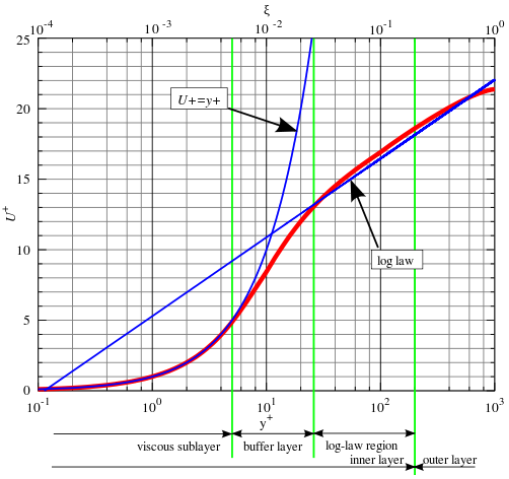

FIGURE 66 NON-DIMENSIONAL VELOCITY VERSUS DISTANCE FROM THE WALL [45]

TABLE 3 DISTANCE TO WALL - Δy

				y^+				y/δ	
				1	5	**30**	300		
	Re	V_A	Re_L			**Δy**		**0.02**	**0.20**
I	8.0E+06	23	4.0E+06	1.91E-06	9.57E-06	5.74E-05	5.74E-04	9.03E-05	9.03E-04
H	6.9E+06	20	3.5E+06	2.18E-06	1.09E-05	6.53E-05	6.53E-04	9.29E-05	9.29E-04
G	3.5E+06	10	1.7E+06	4.15E-06	2.07E-05	1.24E-04	1.24E-03	1.07E-04	1.07E-03
F	1.7E+06	5	8.7E+05	7.89E-06	3.95E-05	2.37E-04	2.37E-03	1.23E-04	1.23E-03
E	1.0E+06	3	5.0E+05	1.32E-05	6.58E-05	3.95E-04	3.95E-03	1.37E-04	1.37E-03

2.5.3 Wall Function

To save computational power, *wall function* is used in the *buffer layer* and *viscous sublayer* instead of resolving the mesh all the way to the wall (i.e., $y^+ < 1$). A reasonable range to aim for when constructing the mesh (for this project) is y^+ values between 30 to 500 (i.e., the log-law layer and preferably more towards the lower range when possible). Using wall functions allows for a lower mesh resolution (less computational power and time). This project tends to favor faster runtime and explore more aspect of the flow condition rather than high mesh resolution and computational precision.

There are a few wall functions to choose from in OpenFOAM. Most relevant is k, ω and ν_t wall functions, since the $k-\omega$ SST turbulence model is of interest of this project [37]. Wall functions are a kind of boundary condition defined in the **0 folder** in the *case folder*. kLowReWallFunction was used for k since it captures both high and low Re. omegaWallFunction switches between viscous and log region according to y^+. nutkWallFunction provide eddy viscosity condition based on k.

Just as a reminder, "All models are wrong, but some models are useful" George E. P. Box. In other words, all models are *approximations*. With these *caveats* and *compromises* in mind we now present **Menter's** $k-\omega$ SST model which is the version of the *turbulence modelling* used in this project.

2.6 SST $k-\omega$ model

Menter built on **Wilcox's** $k-\omega$ model by substituting $\varepsilon = k\omega$ [34].

Transport equation for $\boldsymbol{k}$:

$$\rho\frac{\partial \boldsymbol{k}}{\partial t} + \rho\, div(\boldsymbol{k}\bar{U}) = div\left[\left(\mu + \frac{\mu_t}{\sigma_k}\right)\cdot grad\,(\boldsymbol{k})\right] + P_k - \beta^*\rho\boldsymbol{k}\omega$$

where

$$P_k = \left(2\mu_t S_{ij}\cdot S_{ij} - \frac{2}{3}\rho\boldsymbol{k}\frac{\partial U_i}{\partial x_j}\delta_{ij}\right)$$

Transport equation for $\boldsymbol{\omega}$:

$$\rho\frac{\partial \boldsymbol{\omega}}{\partial t} + \rho\, div(\boldsymbol{\omega}\bar{U}) = div\left[\left(\mu + \frac{\mu_t}{\sigma_{\omega,1}}\right)\cdot grad\,(\boldsymbol{\omega})\right] + P_{\omega,2} - \beta_2\rho\boldsymbol{\omega}^2 + 2\frac{\rho}{\sigma_{\omega,2}\boldsymbol{\omega}}\frac{\partial k}{\partial x_k}\frac{\partial \boldsymbol{\omega}}{\partial x_k}$$

(Note the extra source term at the end)

where

$$P_{\omega,2} = \gamma_2\left(2\rho S_{ij}\cdot S_{ij} - \frac{2}{3}\rho\boldsymbol{\omega}\frac{\partial U_i}{\partial x_j}\delta_{ij}\right)$$

Revised model constants:

$$\sigma_k = 2.0, \qquad \sigma_{\omega,1} = 2.0, \qquad \sigma_{\omega,2} = 1.17, \qquad \gamma_2 = 0.44, \qquad \beta_2 = 0.083, \qquad \beta^* = 0.09$$

Blending function for smoother transition:

$$C = F_C C_1 + (1 - F_C)C_2$$

Limiters for better performance:

$$\mu_t = \frac{a_1\rho k}{\max(a_1\omega, SF_2)}$$

where

$$S = \sqrt{2S_{ij}S_{ij}}, \qquad a_1 = constant, \qquad F_2 = blend\ function$$

and

$$P_k = \min\left(10\beta^*\rho k\omega, 2\mu_t S_{ij}\cdot S_{ij} - \frac{2}{3}\rho k\frac{\partial U_i}{\partial x_j}\delta_{ij}\right)$$

2.7 Power in the Fluid: Actuator Disk Theory

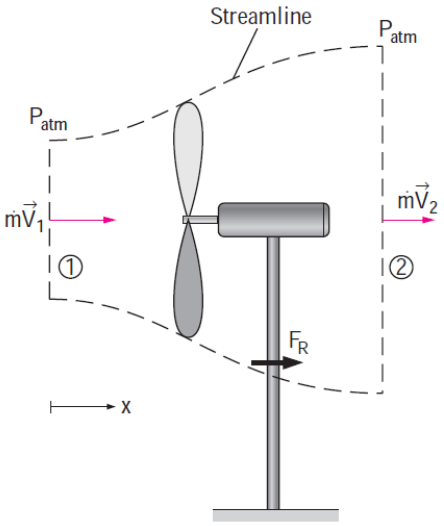

A fluid is *exerting* a force F_R (or thrust T) on the turbine when it *extracts* energy from the flow. Figure on the right shows how the mass flow $\dot{m}$ is slowed down consequently [35].

$$F_R = \dot{m}(V_2 - V_1)$$

A slightly different approach is to consider the Bernoulli equation leading up to the turbine $(1 \rightarrow 3)$ and immediately after the turbine $(4 \rightarrow 2)$, as shown in the figure below.

$$\frac{P_1}{\rho g} + \frac{V_1^2}{2g} + z_1 = \frac{P_3}{\rho g} + \frac{V_3^2}{2g} + z_3 \; and \; \frac{P_4}{\rho g} + \frac{V_4^2}{2g} + z_4 = \frac{P_2}{\rho g} + \frac{V_4^2}{2g} + z_4$$

$$z_1 = z_2 = z_3 = z_4, \qquad V_3 = V_4, \qquad P_1 = P_2 = P_{atm}$$

$$\rightarrow \frac{1}{2}\rho(V_2^2 - V_1^2) = P_4 - P_3 \; and \; \dot{m} = \rho A V_3 \rightarrow V_3 = \frac{V_1 + V_2}{2}$$

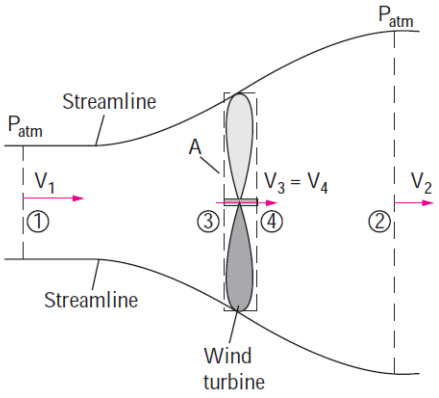

The slowing down of the velocity can also be expressed through an *axial interference factor* $a < 1$ leading to $V_3 = (1-a)V_1$ and thus $V_2 = (1-2a)V_1$ and $\dot{m} = \rho A V_1(1-a)$ as shown on the figure on the left.

$$\begin{aligned} P &= \dot{m} \cdot \frac{1}{2}(V_1^2 - V_2^2) \\ &= \rho A V_1(1-a) \cdot \frac{1}{2}(V_1^2 - V_1^2(1-2a)^2) \\ &= 2\rho A V_1^3 a(1-a)^2 \end{aligned}$$

This leads to a maximum limit of power possible to extract from the fluid when $a = 1/3$ known as the **Betz's** Limit. The efficiency η in this case.

$$\eta_{Betz's\ Limit} = \frac{P}{P_{max}} = \frac{16}{27} \approx 0.593$$

Note that when interference factor a is higher than the optimal, efficiency ηdecreases. Further increase of a can result in conditions where the depressed pressure field downstream of the turbine can reach evaporation pressure for the fluid and cavitation can occur not just lost performance.

2.8 Airfoil vs Wing: Some Differences

A major difference between an *airfoil* section and a finite *wing* is flow component in the *span-wise* direction. Figure below illustrate this flow motion. On the high-pressure side (bottom surface) the streamlines tend *towards* the tips. On the lower-pressure side (top surface) they tend *away* from the tips [38].

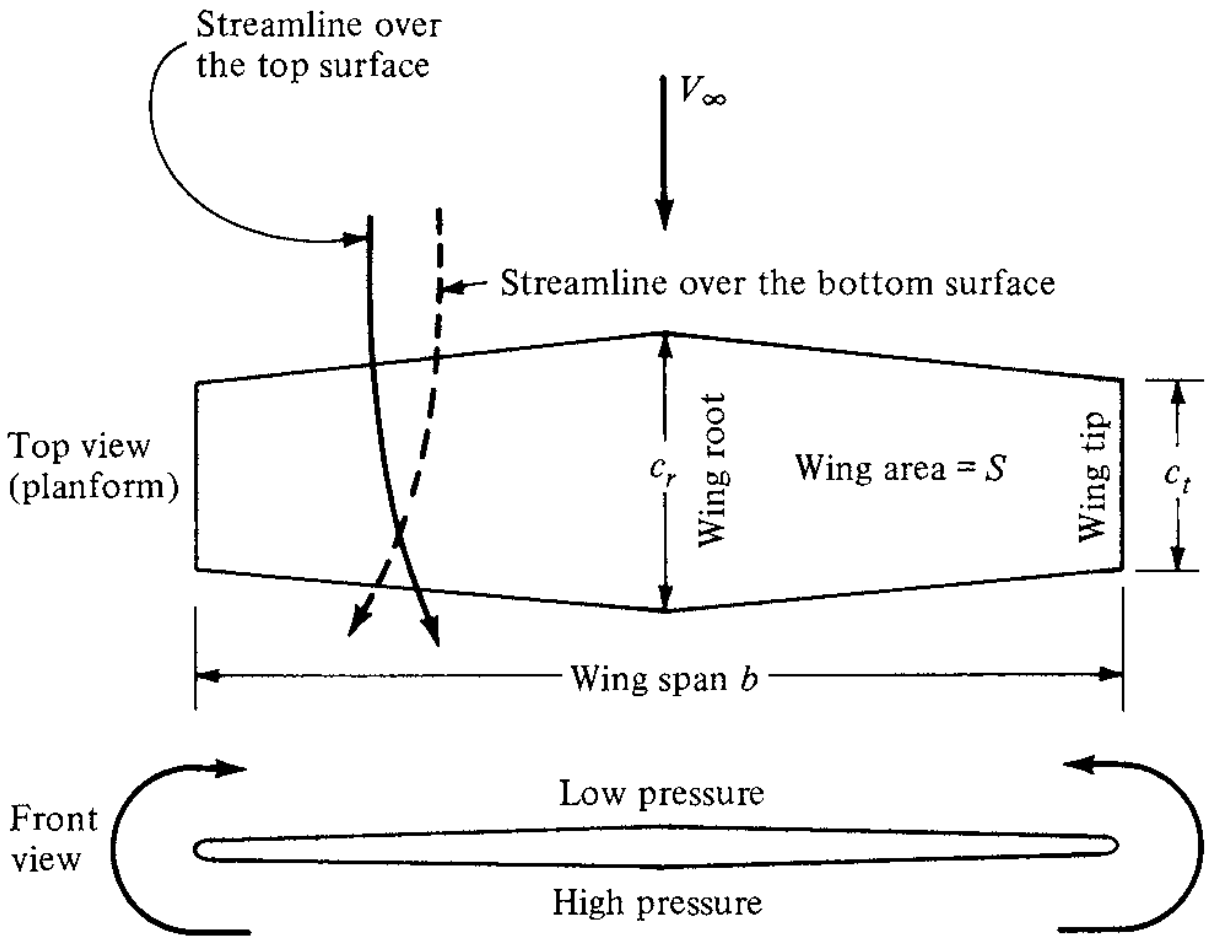

FIGURE 67 FINITE WING. IN THIS FIGURE, THE CURVATURE OF THE STREAMLINES OVER THE TOP AND BOTTOM OF THE WING IS EXAGGERATED FOR CLARITY [38, P. 415]

Imbalances cause leakages resulting in *wing tip vortices* as illustrated by the figure below.

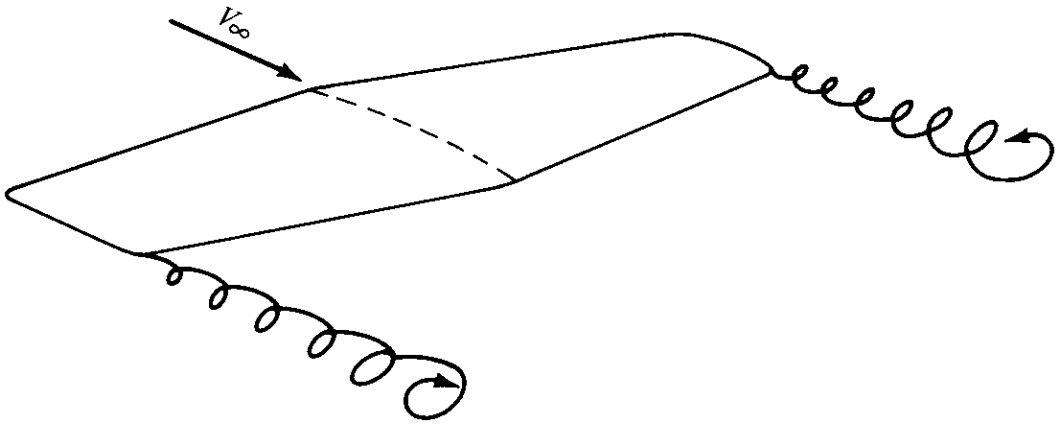

FIGURE 68 SCHEMATIC OF WING-TIP VORTICES [38, P. 416].

Vortices tends to *drag down* the surrounding air and induce a small component on the velocity *downwardly*, known as **downwash** denoted with the symbol *w* in the figure below resulting in a local relative velocity in the vicinity of these vertices with an effective angle of attack α_{eff} that is smaller than the geometric angle of attack α for the local airfoil section as illustrated by figure below.

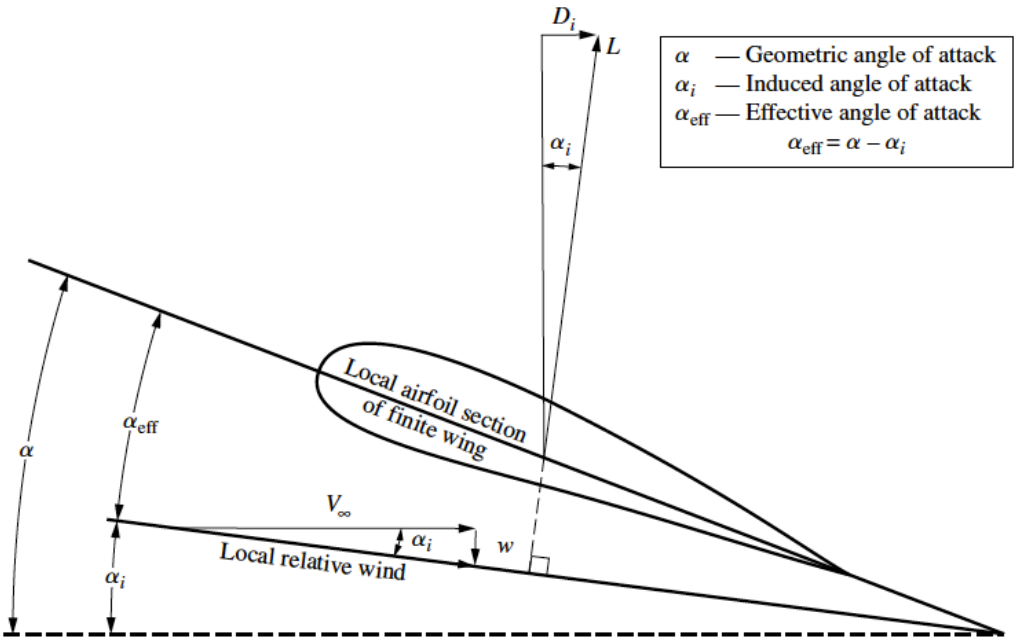

FIGURE 69 EFFECT OF DOWNWASH ON THE LOCAL FLOW OVER A LOCAL AIRFOIL SECTION OF A FINITE WING [38, P. 417]

Lift Coefficient (for an airfoil section or infinite wing)

$$c_l = 2\pi\alpha$$

Lift Slope a_0

$$\frac{dc_l}{d\alpha} = 2\pi = a_0$$

Lift coefficient is linearly proportional to angle of attack (supported by experimental results). The theoretical lift slope is equal to $2\pi\ rad^{-1}\ or\ 0.11\ degree^{-1}$.

Induced Angle of Attack

$$\alpha_i = \frac{C_L}{\pi AR}, \qquad AR = \frac{b^2}{S}, \qquad S = c \cdot b$$

Induced Drag Coefficient (Elliptic Lift Distribution)

$$C_{D,i} = \frac{2\alpha_i}{V_\infty S}\int_{-b/2}^{b/2} \Gamma(y)\, dy = \frac{2\alpha_i \Gamma_0}{V_\infty S}\frac{b}{2}\int_0^\pi \sin^2\theta\, d\theta = \frac{\pi\alpha_i \Gamma_0}{V_\infty S}\frac{b}{2}\cdot\left[-\frac{1}{2}\sin\theta\cos\theta + \frac{1}{2}\theta\right]_0^\theta$$

$$= \frac{\pi\alpha_i \Gamma_0}{V_\infty S}\cdot b \cdot \frac{\pi}{2} = \alpha_i \cdot \frac{\pi b}{2V_\infty S}\cdot \Gamma_0 = \frac{C_L}{\pi AR}\cdot\frac{\pi b}{2V_\infty S}\cdot\frac{2V_\infty S C_L}{b\pi}$$

$$\rightarrow C_{D,i} = \frac{C_L^2}{\pi AR}$$

Induced Drag Coefficient is 1) proportional to the square of lift coefficient C_L^2 and 2) inverse proportional to aspect ratio AR. Induced drag is the price of lift.

Induced Drag Coefficient (General Lift Distribution)

$$C_{D,i} = \frac{C_L^2}{\pi eAR}, \qquad e = (1+\delta)^{-1}, \qquad \delta = \left[1 + \sum_2^N n\left(\frac{A_n}{A_1}\right)^2\right], \qquad \delta \geq 0, e \leq 1$$

Lift Slope a

$$\frac{dc_l}{d\alpha} = \frac{dC_L}{d\alpha_{eff}} = \frac{dC_L}{d(\alpha - \alpha_i)} = a_0$$

$$C_L = a_0(\alpha - \alpha_i) + const \rightarrow C_L = a_0\left(\alpha - \frac{C_L}{\pi AR}\right) + const$$

$$\frac{dC_L}{d\alpha} = a = \frac{a_0}{1 + a_0/\pi AR} \rightarrow a = \frac{a_0}{1 + (a_0/\pi AR)(1 + \tau)}$$

Figure below comparing c_l (airfoil) to C_L (wing). Note how the curves intersect at $\alpha = -3°$ but has different lift slopes ($a_0 > a$). Figure on the next page compares c_d to C_D. For the finite wing, an (lift) induced drag coefficient $C_{D,i}$ is added to the profile drag c_d.

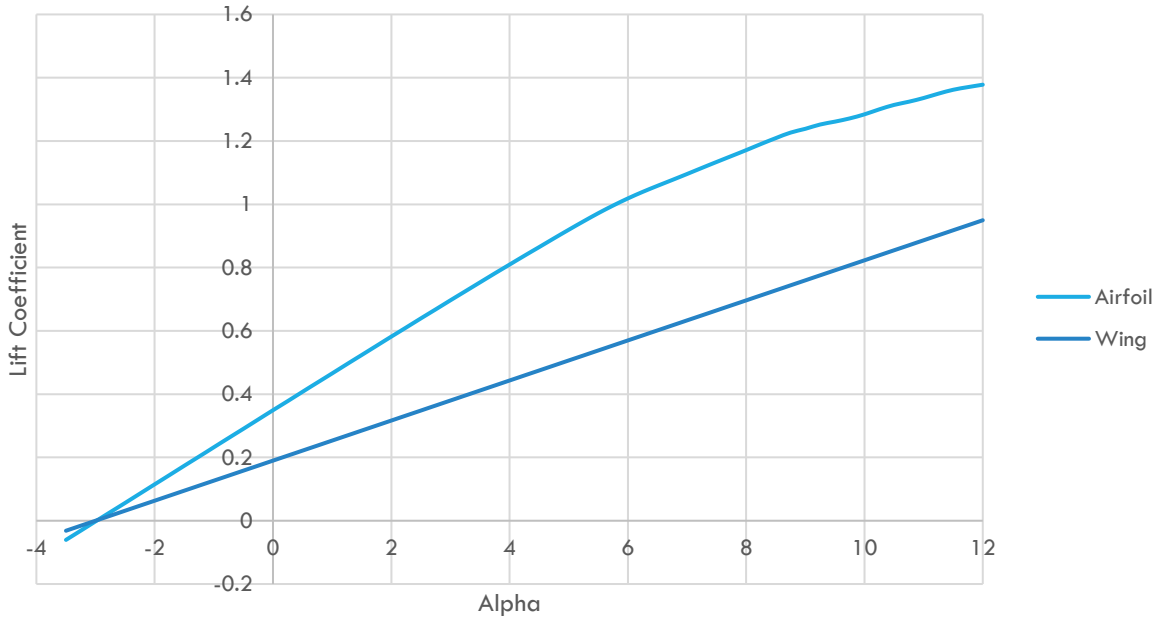

FIGURE 70 COMPARING LIFT COEFFICIENT

Zero-lift angle of attack $\alpha_{L=0}$

$$\alpha_{L=0} = -3^{\circ}$$

Lift Slope a_0

$$a_0 = \frac{0.9 - 0}{5^{\circ} - (-3^{\circ})} = \frac{0.9}{8} = 0.1125\ per\ degree\ or\ 6.446\ per\ radian$$

Induced Drag Factor

$$\delta = 0.01$$

Span Efficiency Factor

$$e = \frac{1}{1 + \delta} = \frac{1}{1 + 0.01} = 0.99$$

Lift Slope a, assuming $\tau = \delta$

$$a = \frac{a_0}{1 + \frac{a_0}{\pi AR}(1 + \tau)} = \frac{6.446}{1 + \frac{6.446}{\pi \cdot 2.67}(1 + 0.01)} = 3.63\ per\ radian, \qquad AR = \frac{8}{3} \approx 2.67$$

$$a = 3.611 \cdot \frac{2\pi}{360} = 0.0633\ per\ degree$$

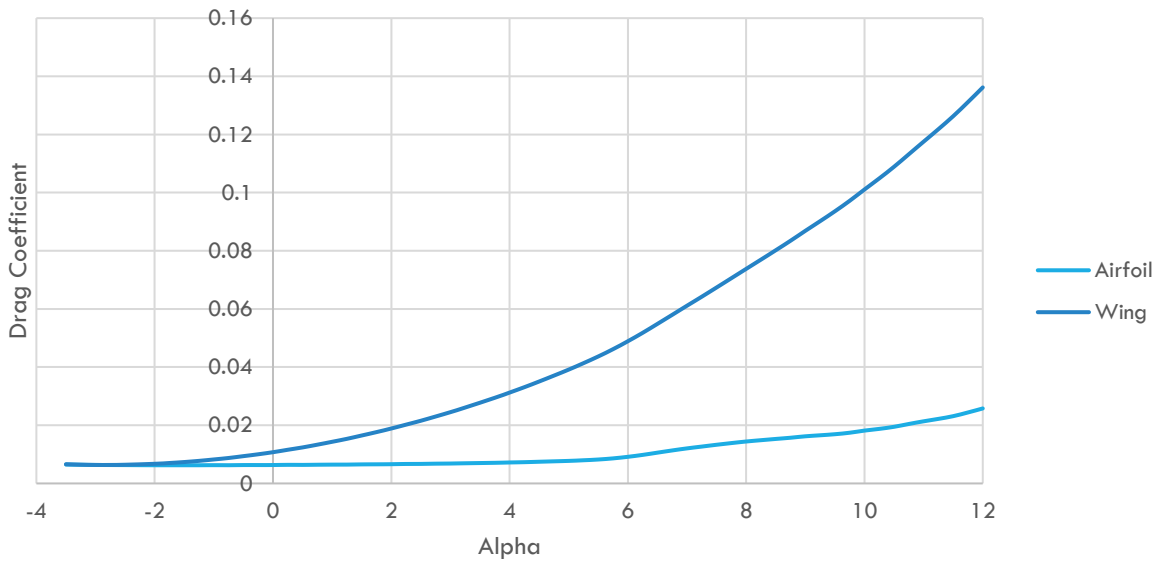

FIGURE 71 COMPARING DRAG COEFFICIENT

Linear Lift Curve

$$C_L = a(\alpha - \alpha_{L=0}) = 0.0633 \cdot \left(5^\circ - (-3^\circ)\right) = 0.506$$

Induced Angle of Attack

$$\alpha_i = \frac{C_L}{\pi AR} = \frac{0.506}{\pi \cdot 2.67} = 0.0605\ rad\ or\ 4.426^\circ$$

Effective Angle of Attack

$$\alpha_{eff} = \alpha - \alpha_i = 5^\circ - 3.464^\circ = 1.536^\circ$$

Lift Coefficient (at α_{eff})

$$c_l = a_0\left(\alpha_{eff} - \alpha_{L=0}\right) = 0.1125 \cdot \left(1.551^\circ - (-3^\circ)\right) = 0.506$$

Induced Drag Coefficient

$$C_{D,i} = \frac{C_L^2}{\pi eAR} = \frac{0.506^2}{\pi \cdot 0.99 \cdot 2.67} = 0.0309$$

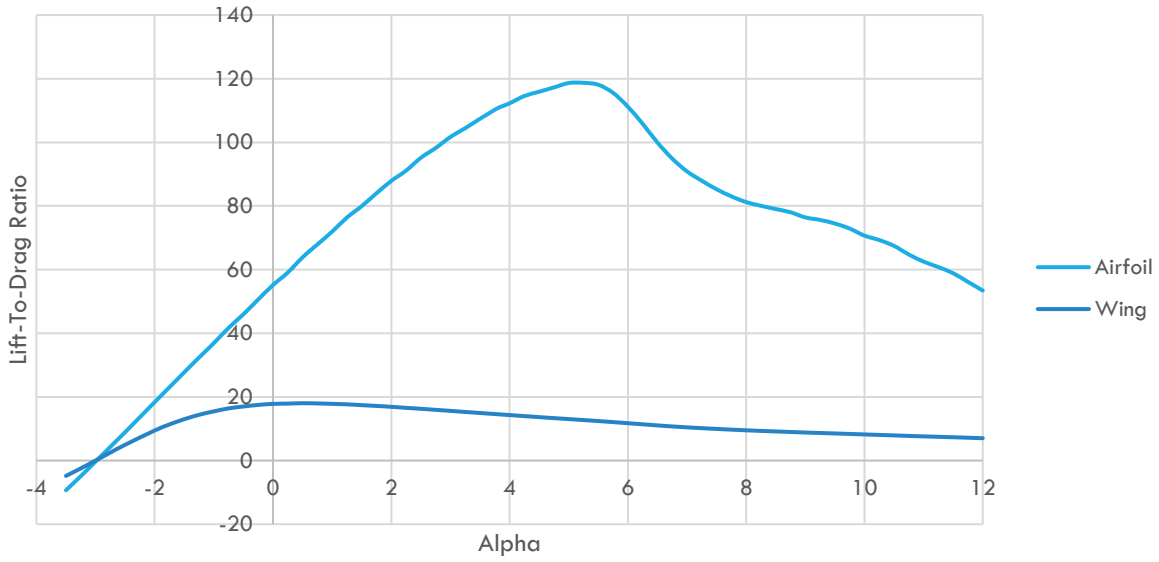

FIGURE 72 COMPARING LIFT-TO-DRAG RATIO

Combining the two figures on the previous pages we can plot the *lift-to-drag ratio* C_L/C_D in the figure above. The optimum is where the highest lift is achieved for the lowest drag. Note how this optimum is shifted towards lower α for the finite wing.

2.9 Crosswind Kite Power: Loyd's Formulation

Loyd defines a **kite** as "an aerodynamic vehicle restrained by a tether". It produces a lift $\vec{L}$ and a drag $\vec{D}_K$ moving through the fluid. The wing is characterized by a *wing area* A, a *lift coefficient* C_L and a *lift-to-drag ratio* $\vec{L}/\vec{D}_K$. A kite moving through the fluid can generate **power** by either *pulling a load* (on the ground, i.e., ground-gen) or by *driving a turbine* (on the kite, i.e., fly-gen). The **force** that the kite pulls with equals the tether tension $\vec{T}$ and the **velocity** the load is pulled by is $\vec{V}_L$, power is the product of *force* and *velocity*. When a kite, flying *traverse* to the flow, is running a turbine onboard experiencing an *apparent velocity* $\vec{V}_A$, the kite produces power by slowing down this apparent velocity and *add* a force or thrust $\vec{D}_P$ to the total drag of the kite. And again, power is the product of force and velocity [16].

Loyd proposes a *simplified analysis*, ignoring the kite weight, tether weight and drag, assuming constant velocity and only considering specific operational conditions. **Power** generated is expressed as follows.

$$P = P_w \cdot A \cdot C_L \cdot F$$

F is a function *specific* to the *mode* and P_w is *power density* in the fluid flow

$$P_w = \frac{1}{2}\rho V_w^3$$

ρ *density* of the fluid and V_w magnitude of *incoming velocity*

Loyd classifies three kite modes and denotes three different F functions for each mode. *Simple kite* mode F_S and two different *crosswind* modes *lift powered* F_C and *drag powered* F_D. The latter is the focus of this project.

Figure below shows the superiority of the *crosswind* modes when compared to the *simple* kite mode. It also shows the optimal power out at the corresponding *velocity ratio* and *drag ratio* for **lift** and **drag** powered mode, respectively.

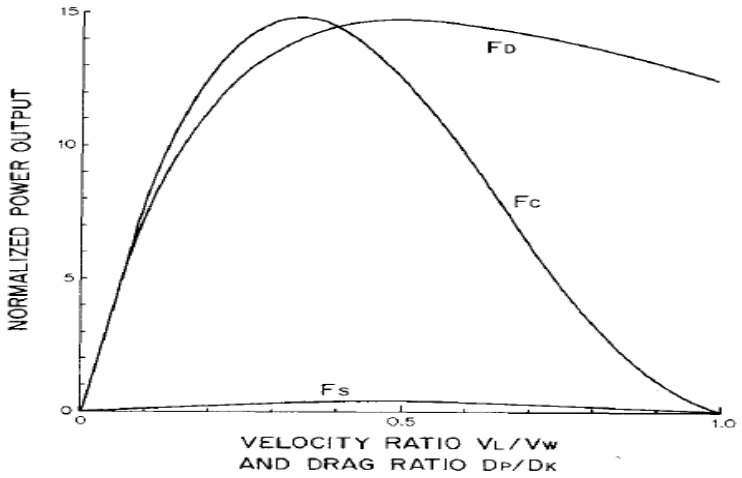

FIGURE 73 RELATIVE POWER FROM CROSSWIND KITES AND SIMPLE KITE WITH L/D_K OF 10

Though the drag powered mode is the focus, it is useful to understand the lift powered mode in comparison with the drag powered mode. The simple kite mode is of lesser interest, it is still useful to understand the simple mode in comparison to the crosswind modes. For completion however, all three modes are briefly presented.

2.9.1 Simple Kite

The kite is facing into the wind and remains static if the tether is restrained. The force that the kite pulls with equals the tether tension $\vec{T}$ and the velocity the load is pulled with is $\vec{V}_L$, power is the product of force and velocity.

$$P = T \cdot V_L$$

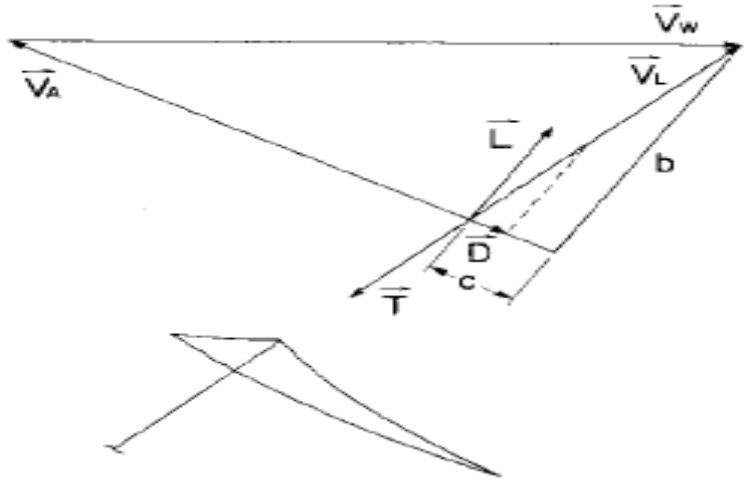

FIGURE 74 FORCES AND VELOCITIES ON A WEIGHTLESS SIMPLE KITE

Triangle $\vec{T}$, $\vec{L}$ and $\overrightarrow{D_K}$

$$T = L \cdot \sqrt{1 + \frac{1}{(L/D_K)^2}}$$

Lift

$$L = \frac{1}{2}\rho C_L A V_A^2$$

(A is wing area)

Triangle $\overrightarrow{V_L}$, b and c

$$\frac{b}{V_L} = \frac{L}{T}$$

Gives b and c only depending on V_L and (L/D_K). (Note b and c are perpendicular).

$$b = \frac{V_L(L/D_K)}{\sqrt{(L/D_K)^2 + 1}}, \qquad c = \frac{V_L}{\sqrt{(L/D_K)^2 + 1}}$$

Then

$$V_w = \sqrt{b^2 + (V_A + c)^2}$$

Using

$$V_L = V_w \frac{V_L}{V_w}$$

Then F_S depends only on V_L/V_w and L/D_K

$$F_S = \frac{V_L}{V_w} \cdot \frac{\left\{\sqrt{1 + \frac{1}{(L/D_K)^2} - (V_L/V_w)^2} - \frac{(V_L/V_w)}{(L/D_K)}\right\}^2}{\sqrt{1 + \frac{1}{(L/D_K)^2}}}$$

Figure below show relative power F_S for L/D_K from 5 to 50. $F_{S,max}$ varies from 0.30 to 0.37.

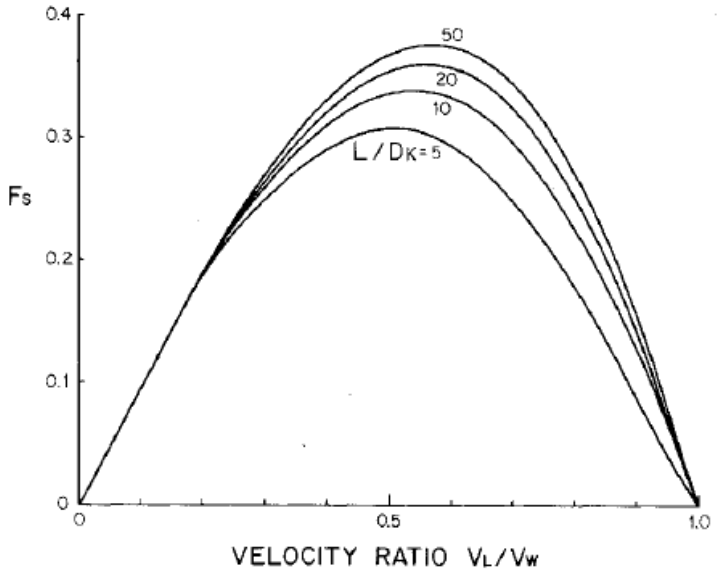

FIGURE 75 RELATIVE POWER FROM SIMPLE KITE

2.9.2 Lift Powered

If the lift is used to extend or pull the tether the effective wind speed at the kite is $\vec{V}_w - \vec{V}_L$ as illustrated by the figure below.

$$V_C = (V_w - V_L) \cdot \frac{L}{D_K} \approx V_A$$

When L/D_K is large and $\vec{V}_A$ and $\vec{V}_C$ is approximately equal in magnitude.

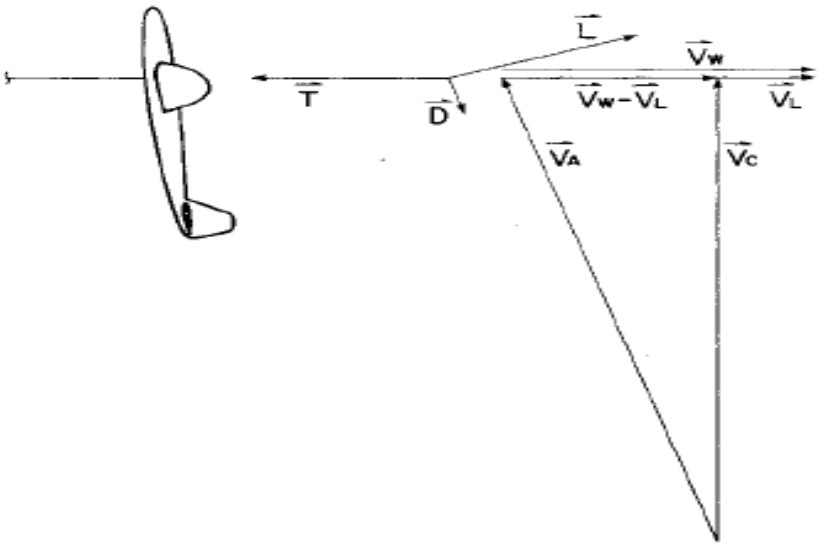

FIGURE 76 FORCES AND VELOCITIES ON A WEIGHTLESS LIFT POWERED KITE

Lift

$$L = \frac{1}{2}\rho C_L A \cdot (V_w - V_L)^2 \cdot (L/D_K)^2$$

Power

$$P = L \cdot V_L$$

Then F_C only depends on V_L/V_w and L/D_K

$$F_C = \left(\frac{L}{D_K}\right)^2 \left(\frac{V_L}{V_w}\right)\left(1 - \frac{V_L}{V_w}\right)^2$$

And

$$F_{C,max} = \frac{4}{27}\left(\frac{L}{D_K}\right)^2$$

At

$$V_L = \frac{1}{3}V_w$$

2.9.3 Drag Powered

By placing the generator on the kite instead of pulling a load on the ground an added drag $\vec{D}_P$ is added to the total drag $\vec{D}$ beside the kite drag $\vec{D}_K$. And $\vec{V}_L = 0$ (no pulling).

$$P = D_P V_A$$

Apparent velocity

$$V_A = V_w \cdot \frac{L}{D_P + D_K}$$

Then F_D only depends on D_P/D_K and L/D_K

$$F_D = \left(\frac{L}{D_K}\right)^2 \frac{(D_P/D_K)}{(1 + D_P/D_K)^3}$$

And

$$F_{D,max} = \frac{4}{27}\left(\frac{L}{D_K}\right)^2$$

At

$$D_P = \frac{1}{2} D_K$$

Figure below illustrate the crosswind drag power mode viewed from above. Note that total drag $\vec{D}$ is the sum of kite drag $\vec{D}_K$ and turbine drag $\vec{D}_P$. Loyd assumed incoming velocity $\vec{V}_w$ much smaller than crosswind velocity $\vec{V}_C$ and approximates $\vec{V}_A \approx \vec{V}_C$.

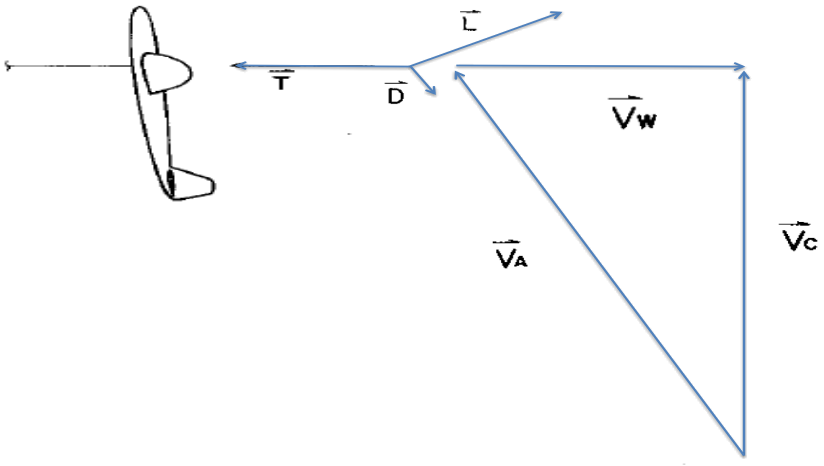

FIGURE 77 FORCES AND VELOCITIES ON A WEIGHTLESS DRAG POWERED KITE

Figure below shows the flight path for the kite in the *detailed analysis*. For airborne kite, gravity is a greater concern. In this project the kite can rely on the buoyancy of the seawater, and we can in practice nearly ignore the gravitational effect. The table at bottom of the page show calculation of some commercial scale kites and the potential power outs.

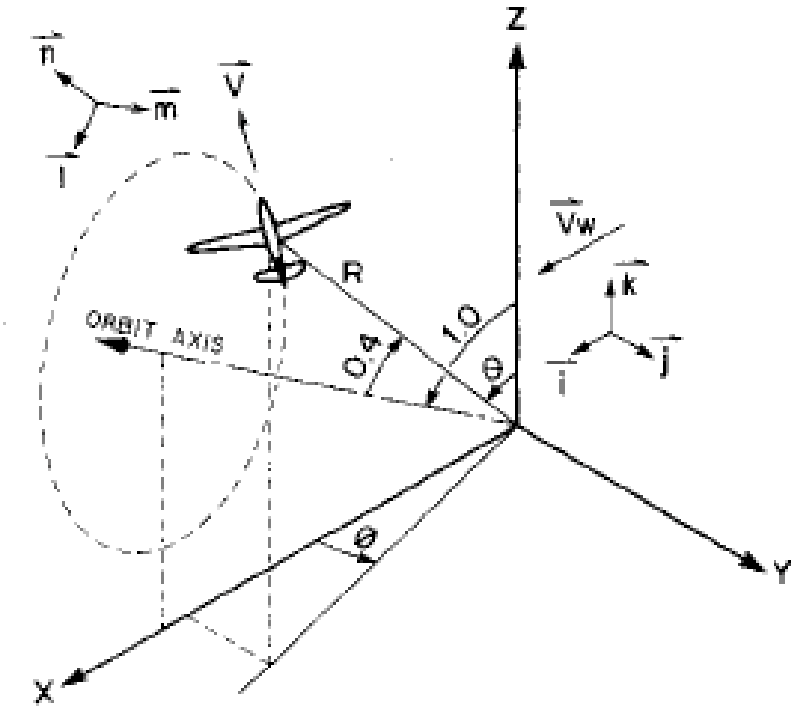

FIGURE 78 COORDINATE USED FOR DETAILED ANALYSIS

TABLE 4 EXAMPLE OF CALCULATION

Example	I	II	III
Kite			
Wing area, m^2	576	1000	2000
Lift-to-drag ratio	20	40	40
Strength-to-weight ratio	10	10	10
Coefficient of lift	1	1	1
Tether			
Length, m	400	1200	1200
Working stress, MPa	345	345	345
Density, Mg/m^3	8	8	8
Coefficient of drag	0.04	0.04	0.04
Wind			
Speed, m/s	10	10	10
Result of calculation			
Average power output, MW	6.7	19	45
Peak tether tension, MN	3.2	10.6	22.2

2.10 Potsdam Propeller as Turbine

Before simulating a **hydrokinetic turbine**, it is useful to simulate a validated case with known experimental data. The *Potsdam Propeller Test Case* (**PPTC**) was chosen for this purpose [39]. The **PPTC** was performed with a *controllable pitch propeller* **VP1304** using a towing tank. *Thrust* and *torque* was reported in *Open Water Test Report* **SVA 3752** [40].

2.10.1 Potsdam Propeller Test Case (**PPTC**)

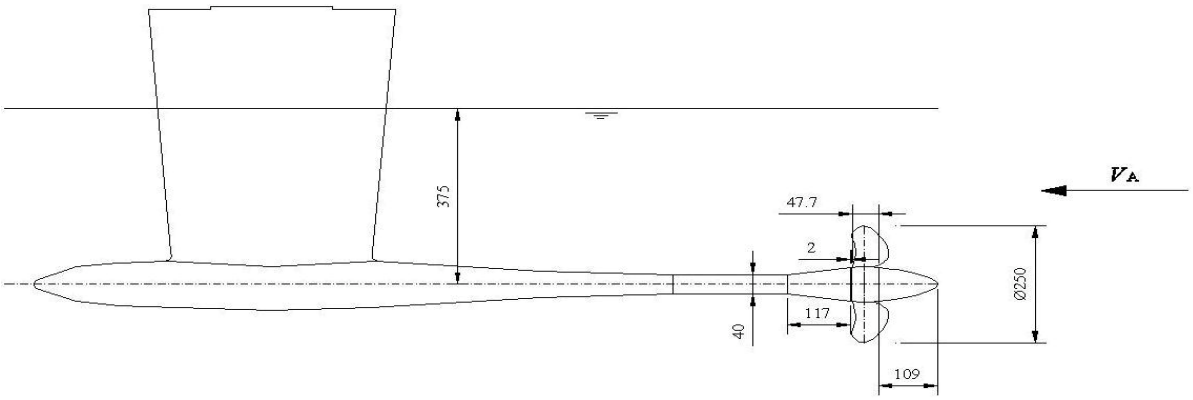

Five different velocities from $2-5\ m/s$ was used with three mesh refinement levels. With the given water density $\rho = 1\,000\ kg/m^3$, kinematic viscosity $\nu = 1e-6\ m^2/s$ and rotational speed $n = 15\ s^{-1}$, *thrust*, *torque* and *advance coefficient* was calculated together with the open water *efficiency* η_0 with the formulas below.

Advance Coefficient

$$J = \frac{V_A}{n \cdot D}, \qquad D: Diameter$$

Thrust Coefficient

$$K_T = \frac{T}{\rho \cdot n^2 \cdot D^4}, \qquad T: Thrust$$

Torque Coefficient

$$K_Q = \frac{Q}{\rho \cdot n^2 \cdot D^5}, \qquad Q: Torque$$

Open Water **Efficiency**

$$\eta_0 = \frac{J}{2\pi} \cdot \frac{K_T}{K_Q}$$

Based on the Loyd formulation we now perform some calculations using the **PPTC** propeller as our turbine for this project. We calculate the power output given the turbine of this size and estimate the corresponding kite size needed to support the given turbine size. The figure on top show the optimal rotational speed at $J = 1.3$. The figure on the bottom shows the propeller with the stem in front used in the kite simulations.

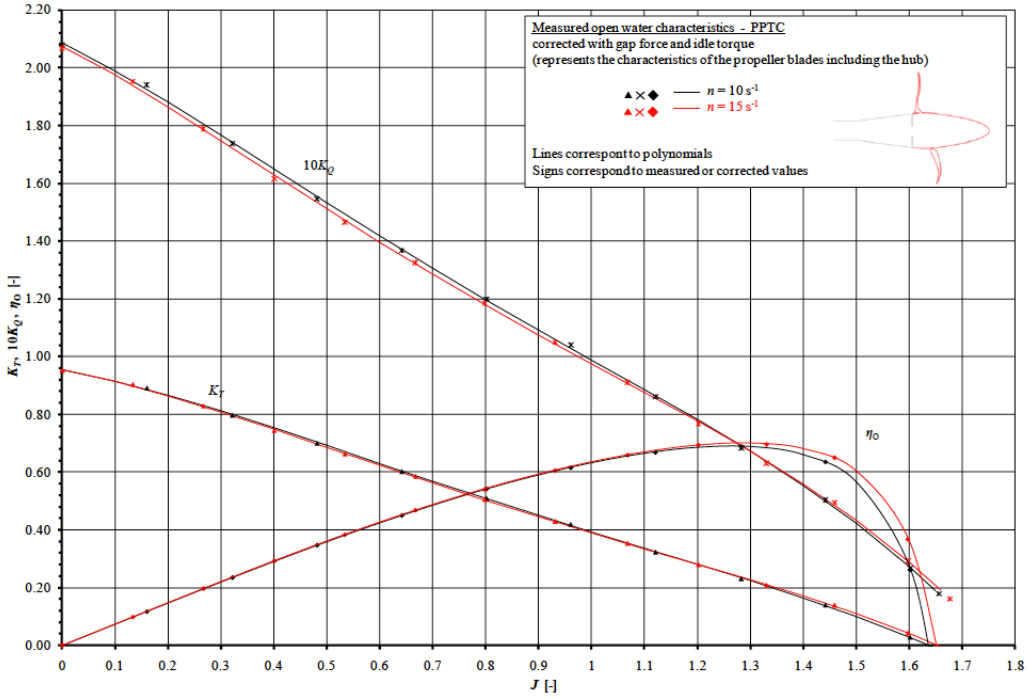

FIGURE 79 OPEN WATER CHARACTERISTICS OF VP1304 [40]

FIGURE 80 PROPELLER VP1304 AS TURBINE WITH FRONT MOUNTED STEM [41]

Propeller Diameter

$$D = 0{,}25\ m$$

Cross-section Area

$$A = \frac{\pi}{4} D^2 = 0{,}049\ m^2$$

Ocean current velocity

$$V_w = 2.0 \frac{m}{s}$$

Apparent Velocity

$$V_A = \frac{L}{D} \cdot V_w = 10 \cdot 2.0 \frac{m}{s} = 20 \frac{m}{s}, \qquad \frac{L}{D} = \frac{L}{D_K + D_P} = 10$$

From the figure on top of the previous page:

$$J_{optimal} = \mathbf{1.3} \rightarrow n = \frac{V_A}{J \cdot D} = \frac{20}{1.3 \cdot 0.25} = 61.53\ s^{-1}, \qquad \omega = 387 \frac{rad}{s}$$

$$K_{T,opt} = \mathbf{0.24} \rightarrow T = K_T \cdot \rho \cdot n^2 \cdot D^4 = 3.55\ kN = D_P$$

Lift

$$L = 10 \cdot (D_K + D_P) = 10 \cdot (7.10 + 3.55)\ kN = 106.5\ kN$$

Lift-to-drag for Kite (wing without the turbine)

$$\frac{L}{D_K} = \frac{106.5}{7.10} = 15$$

Optimal Power Drag to Kite Drag

$$D_P = \frac{1}{2} D_K$$

Water density and Betz's Limit

$$\rho = 1\,000 \frac{kg}{m^3}, \qquad C_p = \frac{16}{27}$$

Potential

$$P = \frac{1}{2} \rho A V_A^3 = \frac{1}{2} \cdot 1\,000 \cdot 0{,}049 \cdot 20^3\ kW = 196\ kW$$

Drag Powered

$$P_{Drag} = C_p \cdot P = \frac{16}{27} \cdot 196\ kW = 116\ kW$$

Turbine Drag (or Thrust)

$$D_P = \frac{P_{Drag}}{V_A} = \frac{116\ \ kW}{20\ m/s} = 5.82\ kN$$

Kite Drag

$$D_K = 2 \cdot D_P = 11.6\ kN$$

Kite Lift

$$\frac{L}{D_K} = 15 \rightarrow L = 15 \cdot D_K = 174.5\ kN$$

Lift Coefficient[1]

$$C_L = \frac{L}{\frac{1}{2}\rho V^2 A} = 1.0$$

Wing Area

$$\rightarrow A = \frac{L}{\frac{1}{2}\rho V^2 \cdot C_L} = \frac{174.5}{\frac{1}{2} \cdot 1000 \cdot 20^2 \cdot 1.0} m^2 = 0.873\ m^2 = S$$

Wing Span

$$\text{AR} = \frac{b^2}{S} = \frac{8}{3} \rightarrow b = \sqrt{\frac{8}{3} \cdot 0.873\ m^2} = 1.53\ m, \qquad c = 0.571\ m$$

(assuming an Aspect Ratio $AR = 8/3$) [2]

Using the PPTC propeller as the turbine, a kite with a wingspan about $1.53\ m$ is needed to drive a turbine of $0.25\ m$ in diameter. Assuming $2\ m/s$ incoming velocity, a $20\ m/s$ velocity is felt by the kite (and the turbine). According to Loyd the optimum output is when the turbine drag is half the kite drag. The power out of $116\ kW$ is the upper limit before other losses like mechanical and electrical losses are accounted for. This concludes the *theory* section. We now move on to the *validation* of the propeller and the kite.

[1] Lloyd assumed $C_L = 1$ in table 1 "Examples of calculations" based on C-5A profile.

[2] Minesto use $AR = 8/3$ for its Deep Green kite.

3 Validation of Propeller[3]

With some indication of the power out potential for a turbine of mentioned size we now turn to the validation of the simulation tool using the mentioned test case.

3.1 Computational Setup

The **OpenFOAM** version 8 *Propeller Tutorial* was used as a starting point. Geometry of the propeller imported from the **PPTC** webpage into **Inventor** [39]. Geometry for inner, middle, and outer cylinder was drawn and **.obj** files were generated for both mesh and propeller.

3.1.1 Geometry

The inner-cylinder was fitted around the propeller tip. The middle-cylinder is meant to capture the wake region where turbulence is dissipating. The outer-cylinder captures the computational domain. About 5 times the propeller diameter ($250\ mm$) was set before the propeller and $20D$ behind. The total length of the domain is $6.25\ m$.

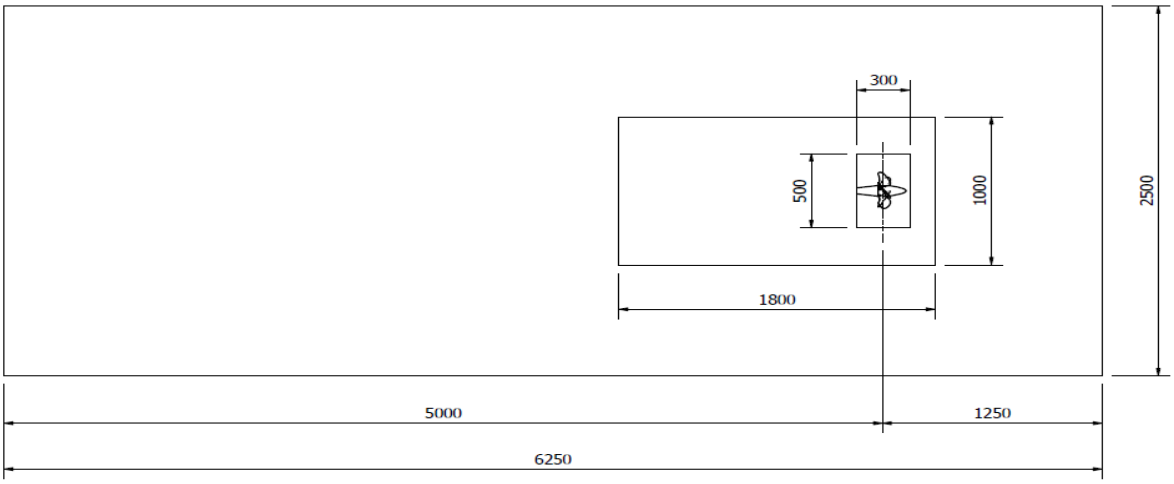

FIGURE 81 MODIFIED GEOMETRIES FROM THE PROPELLER TUTORIAL.

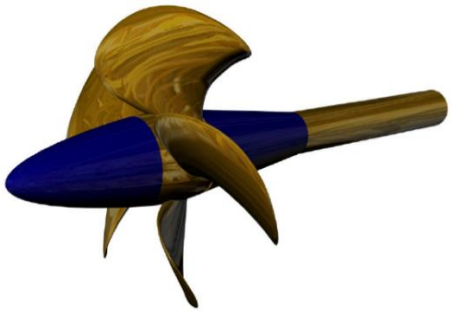

FIGURE 82 GEOMETRIES OF THE PROPELLER GIVEN IN PPTC SMP'11 WORKSHOP [48]

[3] 'Validation of propeller' and some of the theory section was previously submitted as 'Verification of Potsdam Propeller Test Case' a compulsory assignment in MSK600 Spring 2021.

3.1.2 Mesh

To generate the background mesh, **blockMesh** was used with 25 cells in x direction and 10 in y and z. The mesh was then refined with **snappyHexMesh** using different refinement level for inner-, middle- and outer-cylinder. The finest level of refinement was reserve for the propeller surface. Zero level refinement in the outer-cylinder; level 1 refinement in the middle and level 2 in the inner-cylinder and level 5 on the surface of the propeller. Refining the background mesh then further refined the mesh. Stepping up from (25 10 10) (i.e., coarse) to (50 20 20) (i.e., medium) to (100 40 40) (i.e., fine).

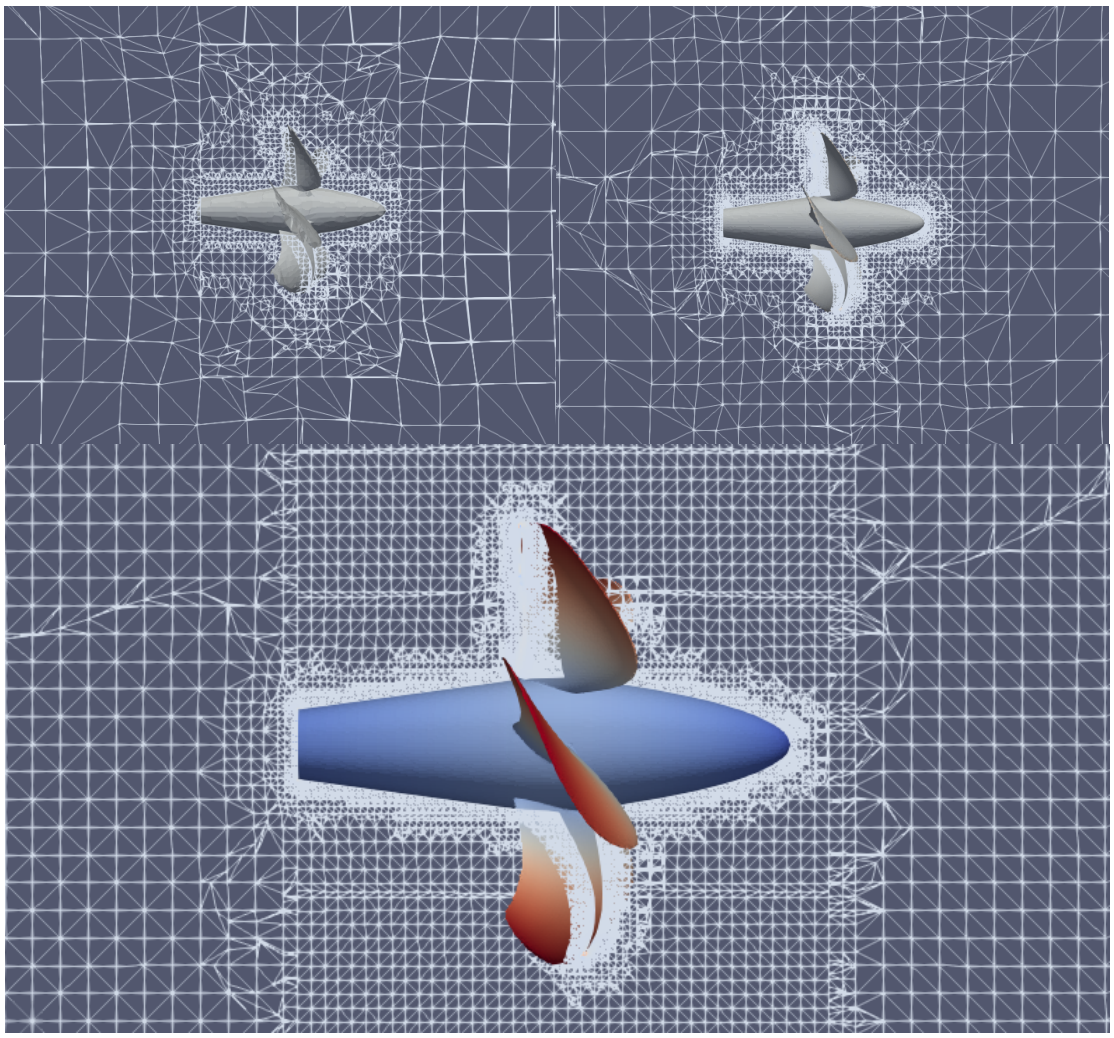

FIGURE 83 MESH REFINEMENTS, THE UPPER LEFT IS THE COARSER MESH, UPPER RIGHT IS MEDIUM AND THE LOWER IS THE FINEST MESH. NOTE THE INNER-CYLINDER REGION HAS ONE LEVEL OF REFINEMENT ABOVE THE UNREFINED BACKGROUND MESH AND THAT THE FINEST REFINEMENT WAS RESERVED FOR THE SURFACE.

3.1.3 AMI

To simulate a rotating propeller an *Arbitrary Mesh Interface* (**AMI**) was defined. By encapsulating the propeller tip inside the inner-cylinder and patches shared in the interface between inner and middle-cylinder could be defined. Using **dynamicMeshDict** in the system folder the rotation speed and direction of the inner cylinder was defined. By rotating the inner-cylinder, the propeller also rotates.

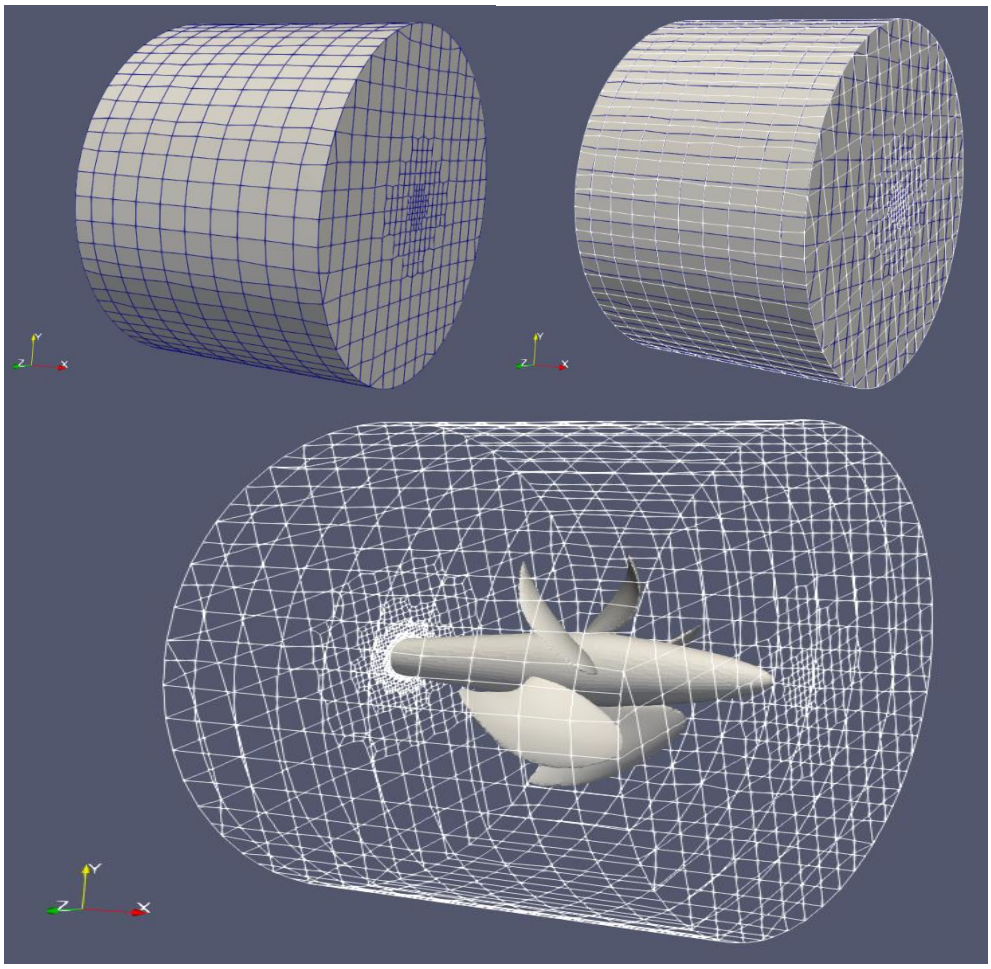

FIGURE 84 AMI, UPPER LEFT IS THE SLAVE (STATIC) PATCH, UPPER RIGHT IS THE MASTER (DYNAMIC) PATCH, LOWER SHOWS THE PROPELLER INSIDE THE MASTER PATCH.

3.1.4 Solver

To solve the *transient* Potsdam Propeller Test Case the **foamPimple** solver was used. The **PIMPLE** algorithm is a combination of the Semi-Implicit Method for Pressure Linked Equations (**SIMPLE**) and the Pressure Implicit with Splitting of Operators (**PISO**) procedures [34]. SIMPLE is a 'guess and correct' procedure until convergence is achieved. The PICO add an extra correction step to hasten the convergence and can be assumed achieved at each time step after a single iteration. For thrust and torque to stabilize, a simulation with a sufficient time length is necessary. With 15 rotations per second, it was assumed that 0,1 s should suffice.

3.1.5 Initials

The **0 folder** contains all the initial values for the variable we are solving for. Values for k and ω were calculated for each incoming velocity U_{ref} using the above-mentioned recommendation for initial values. The characteristic length $L = 0{,}1\ m$ is the propeller chord length at $r/R = 0{,}7$. Table below is summery.

TABLE 5 INITIAL VALUES FOR INCOMING VELOCITY U_{ref}, k AND ω

$U_{ref}[m/s]$	Re	$\ell[m]$	Ti	$k[m^2/s^2]$	$\omega[s^{-1}]$
2,0	200 000	0,007	0,03479	0,00726	22,22
3,0	300 000	0,007	0,03307	0,01477	31,69
4,0	400 000	0,007	0,03191	0,02443	40,76
4,5	450 000	0,007	0,03144	0,03002	45,19
5,0	500 000	0,007	0,03103	0,03620	49,56

It is useful to remember that with any numerical calculations the initial values are useful guesses and will mostly determine the speed of the convergence. Imprecise chosen initial values will most likely lead to unnecessary timely and costly calculation but not always to divergence and no solution.

3.2 Thrust and Torque

Function Object '**forces**' in OpenFOAM was used to extract thrust and torque. A *python* script was used to post-process the *force.dat* file. An *average* of the last 100 values was used for the calculations. The time length of the simulation seems to be sufficient for thrust and torque to stabilize. Figures below are a few samples.

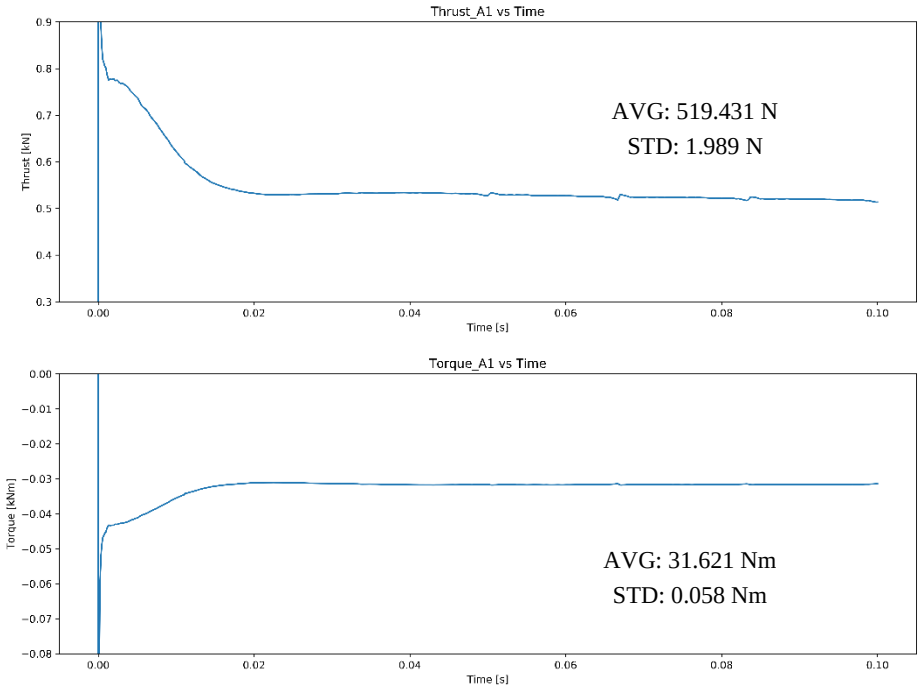

FIGURE 85 THRUST AND TORQUE FOR A1

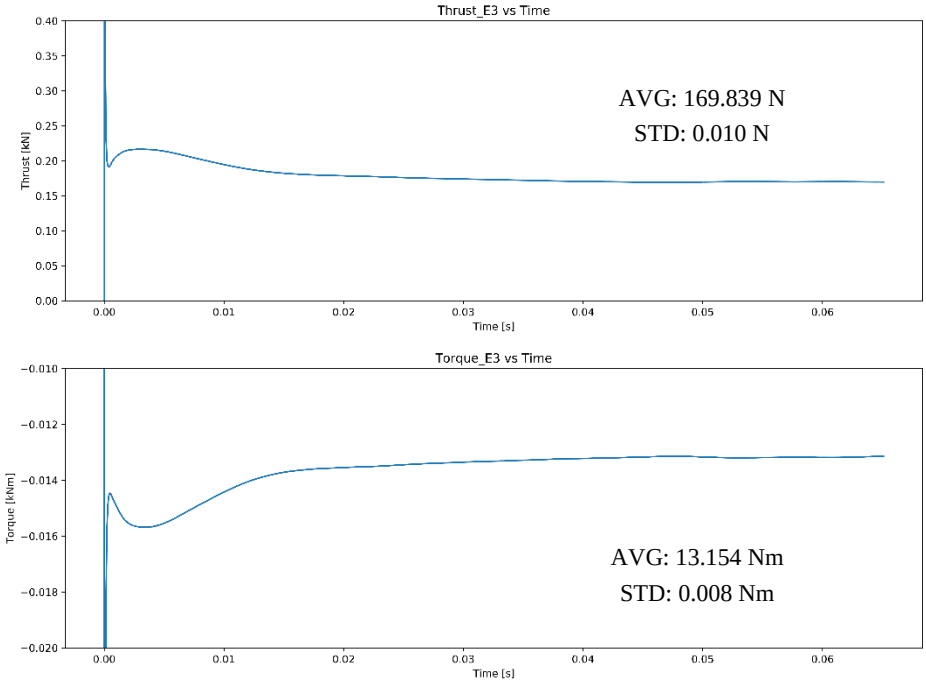

FIGURE 86 THRUST AND TORQUE FOR E3

3.3 $K_T, 10K_Q$ and μ_0

With data from *forces.dat* and using the formulas given by the test case the figure below was generated. Index 0 is the experimental data; index 1-3 is the three level of mesh refinement.

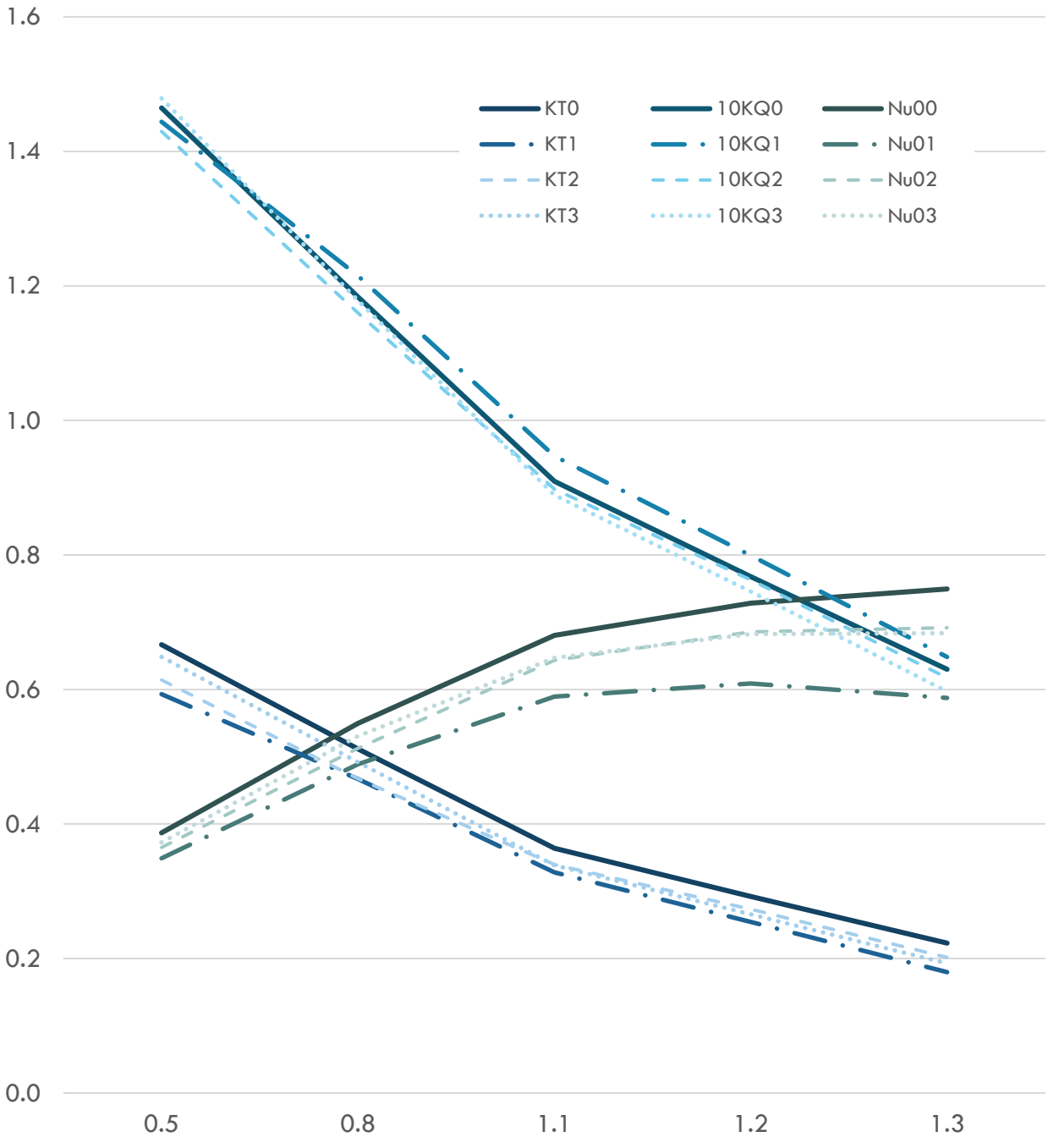

FIGURE 87 COMPARISONS OF EXPERIMENTAL DATA TO FOAM

3.4 Velocity Field

The reasonably good agreement between the simulated and measured velocity field is a good indication of the simulation's ability to capture the flow condition immediately around the propeller [41]. The figures on the following two pages are a small sample.

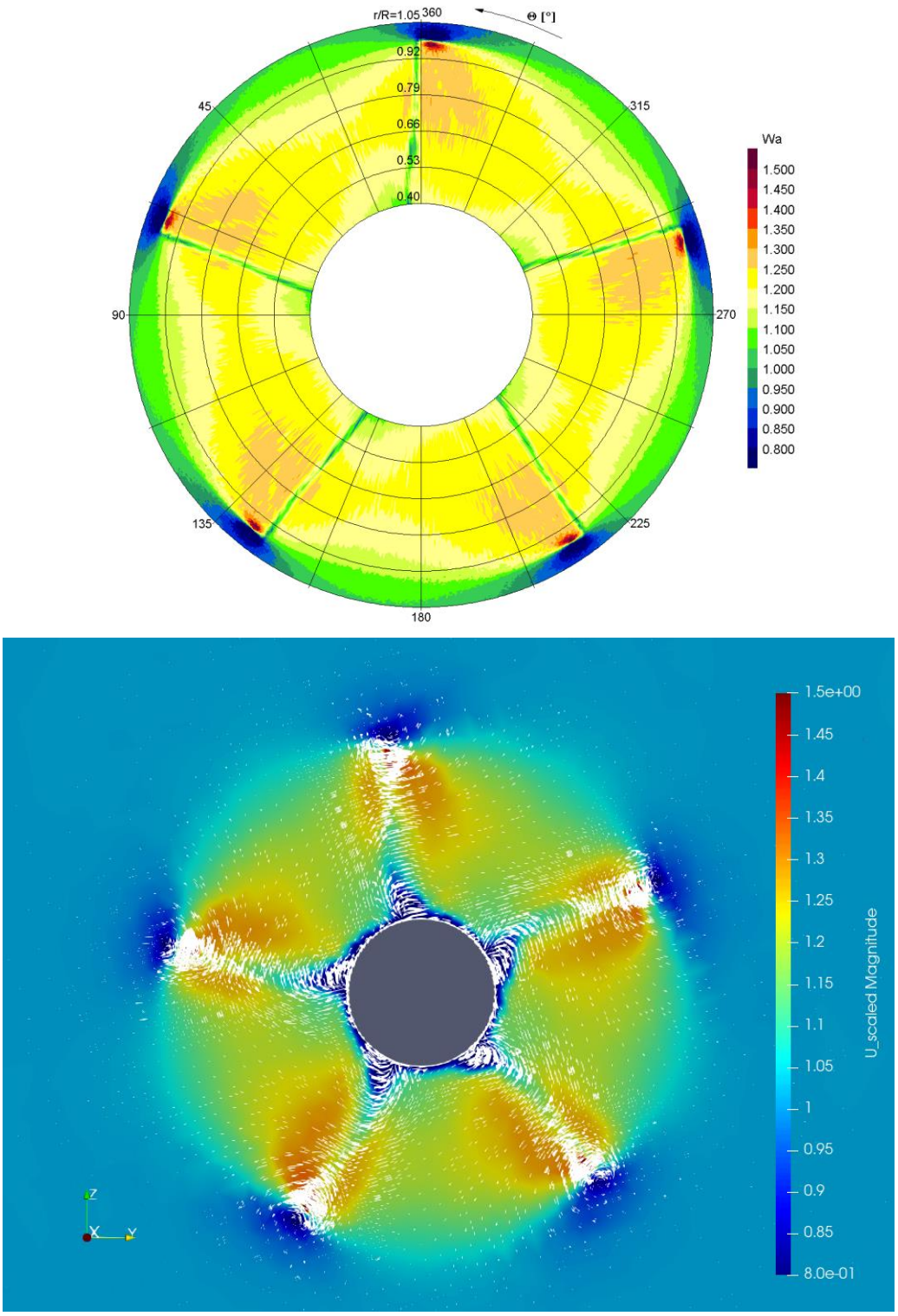

FIGURE 88 AXIAL VELOCITY COMPONENTS, X/D = 0.10. PPTC (TOP) AND FOAM (BOTTOM)

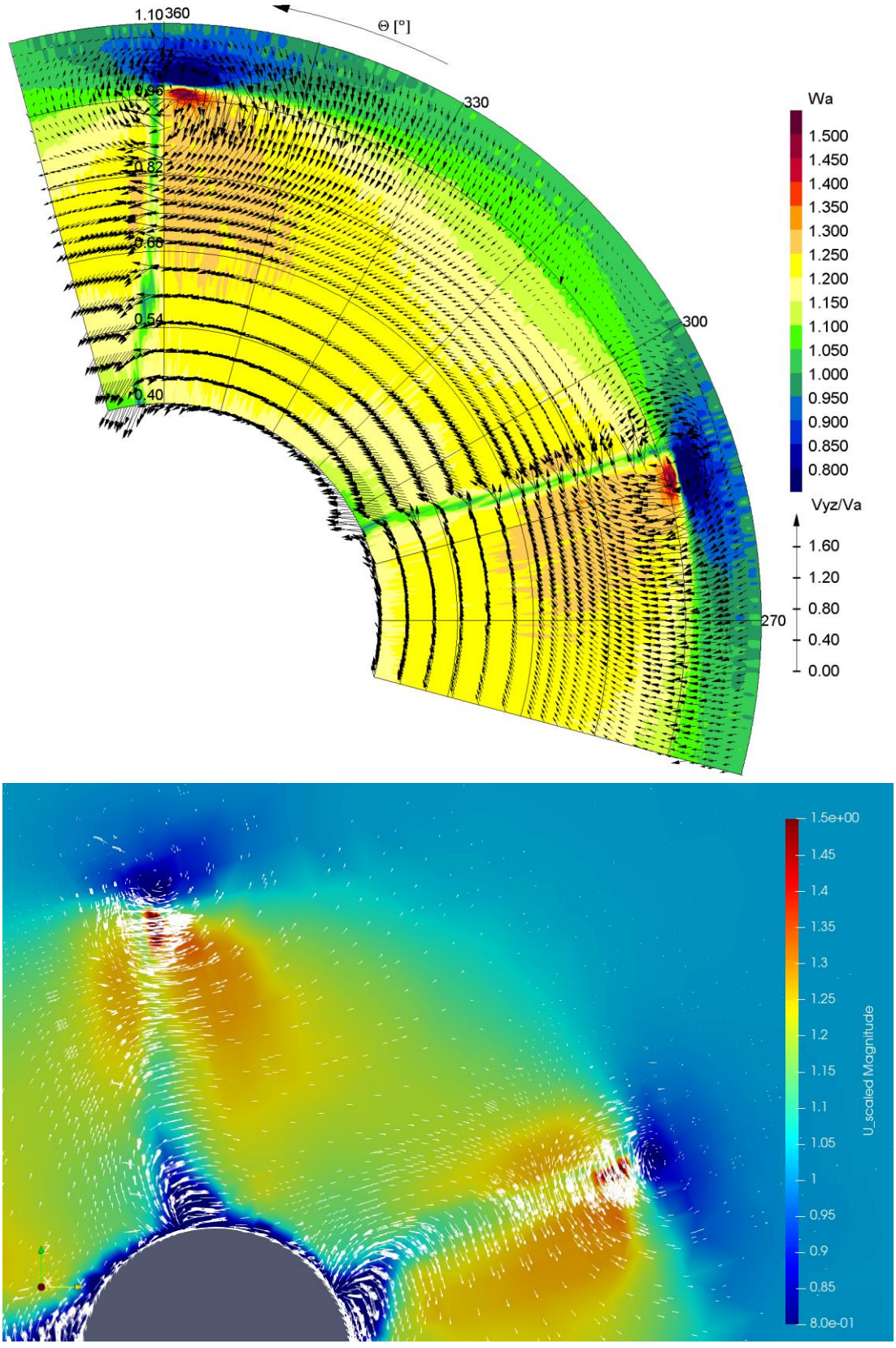

FIGURE 89 VELOCITY COMPONENTS, X/D = 0.11. PPTC (TOP) AND FOAM (BOTTOM)

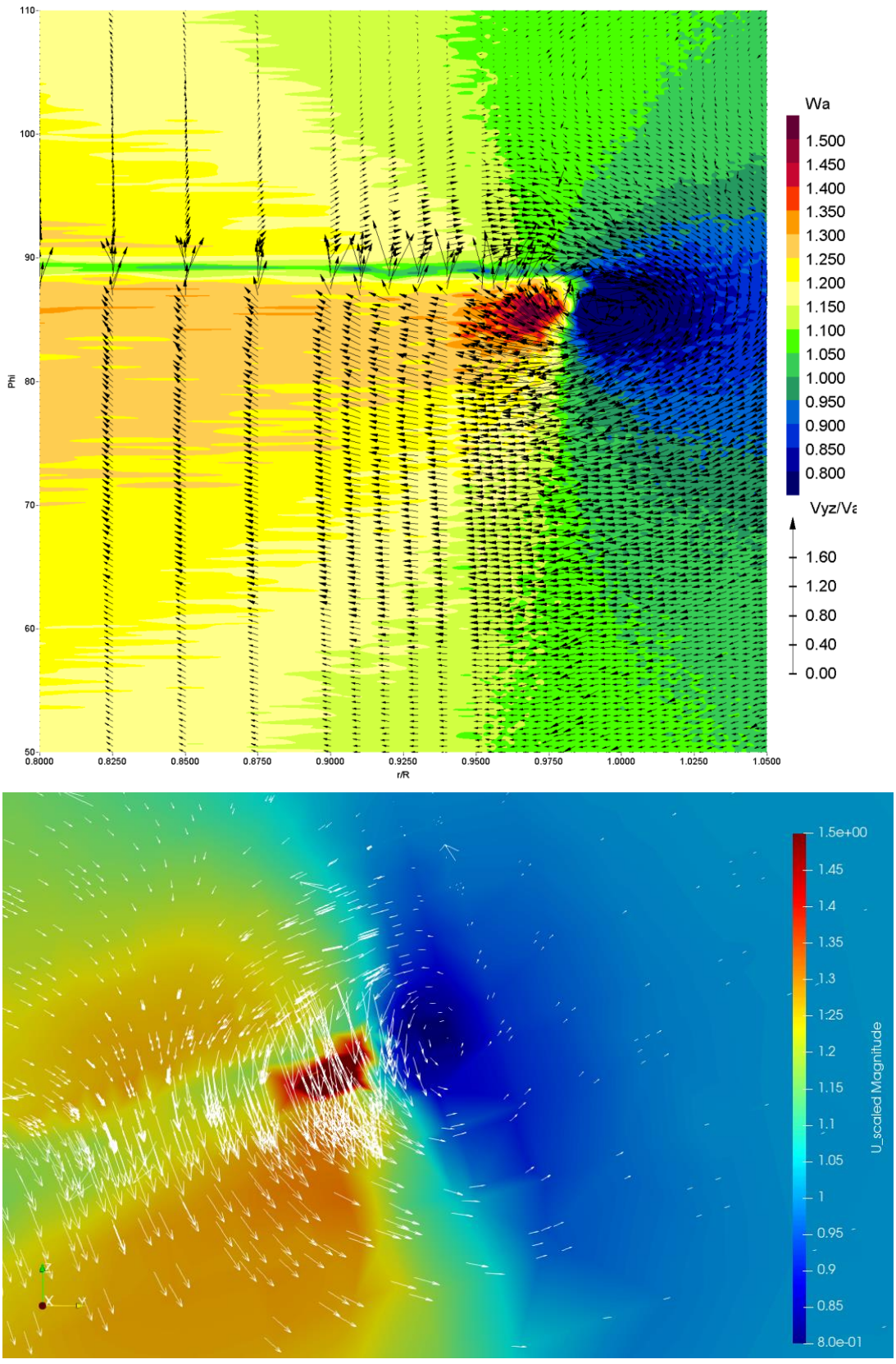

FIGURE 90 DETAILED VELOCITY FIELD, X/D = 0.11. PPTC (TOP) AND FOAM (BOTTOM)

3.5 Wake Field

"Plot over line" filter in **Paraview** was used to plot wake field. Datapoints was extracted as **.csv** format. Simulation agrees well with data at the trailing edge at closer distance (see figure below) and do not seem to be able to capture the vortex generation farther downstream (see figure on the next page).

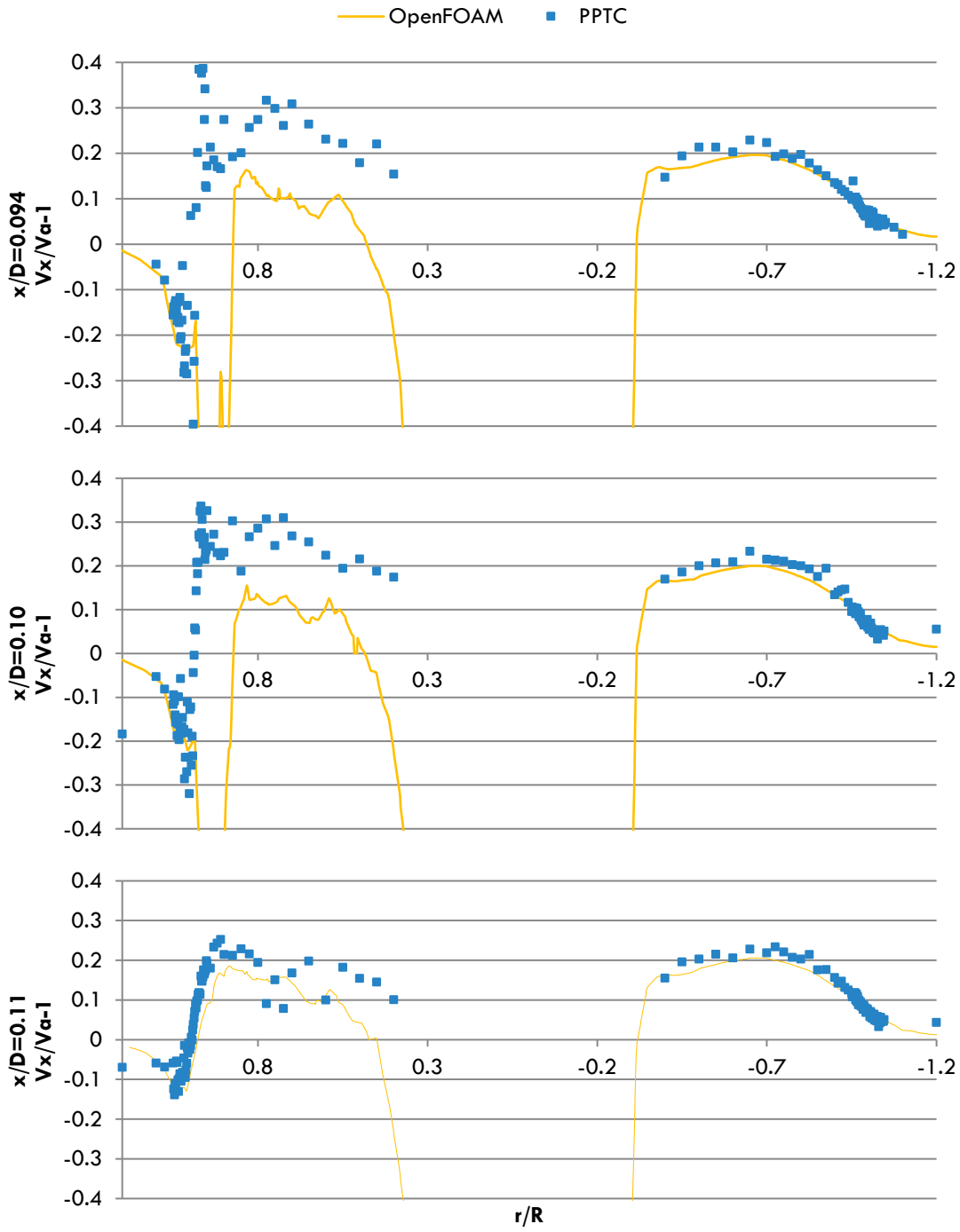

FIGURE 91 WAKE FIELD DOWNSTREAM AT DIFFERENT DISTANCES. COMPARING SIMULATION TO EXPERIMENTAL DATA.

On the other hand, simulation capture more satisfactory the flow on the opposite side of the trailing edge father downstream (see left side of the figure below). Note that the y-axis measure velocity-defect due to the propeller blades.

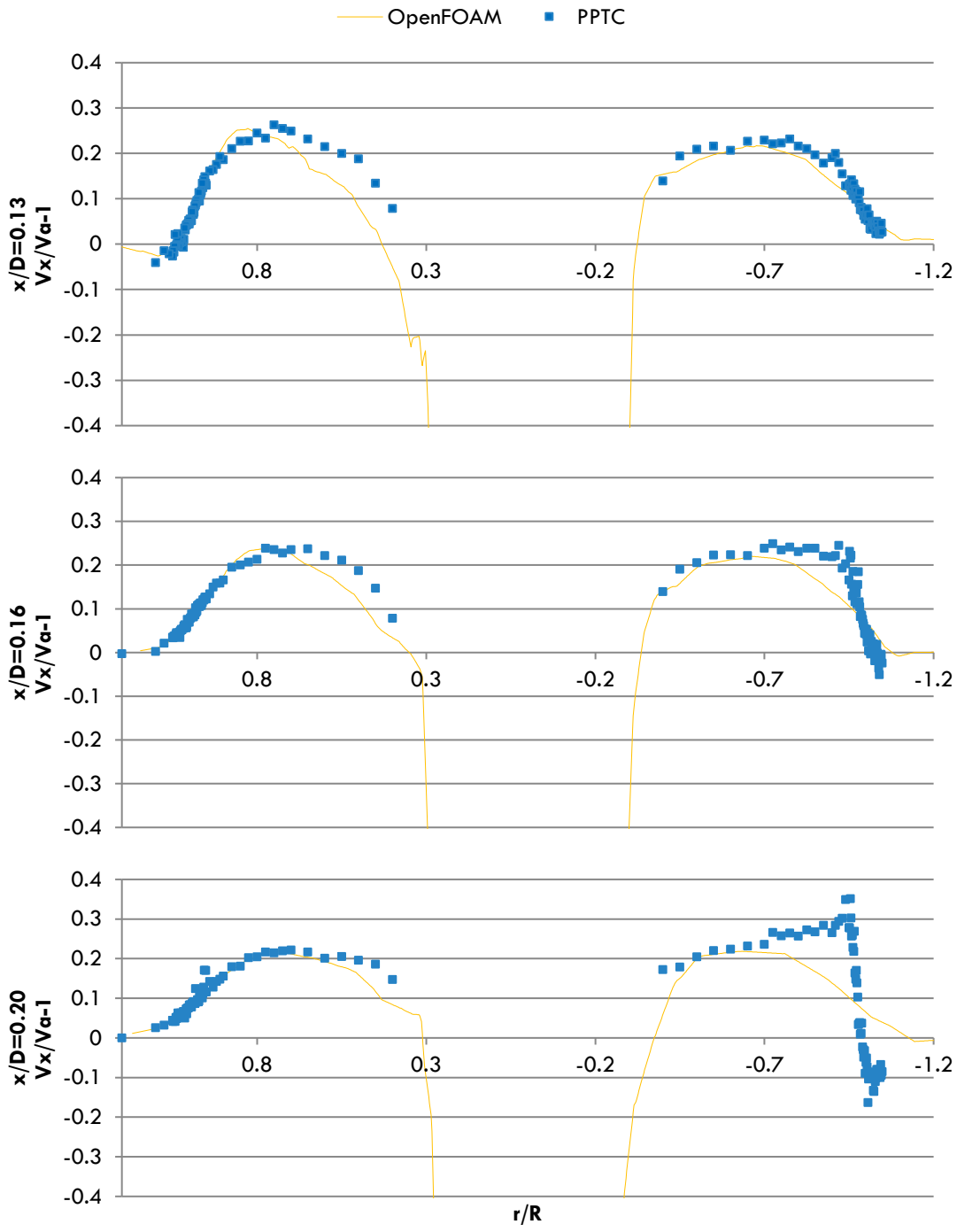

FIGURE 92 WAKE FIELD DOWNSTREAM AT DIFFERENT DISTANCES. COMPARING SIMULATION TO EXPERIMENTAL DATA.

The same measurement can also be presented along a circle at a radius form center of rotation, “Plot On Intersection Curves” filter was used to extract the datapoints from Paraview. Figure below present velocity-defect at a given distance downstream on circles with different radius.

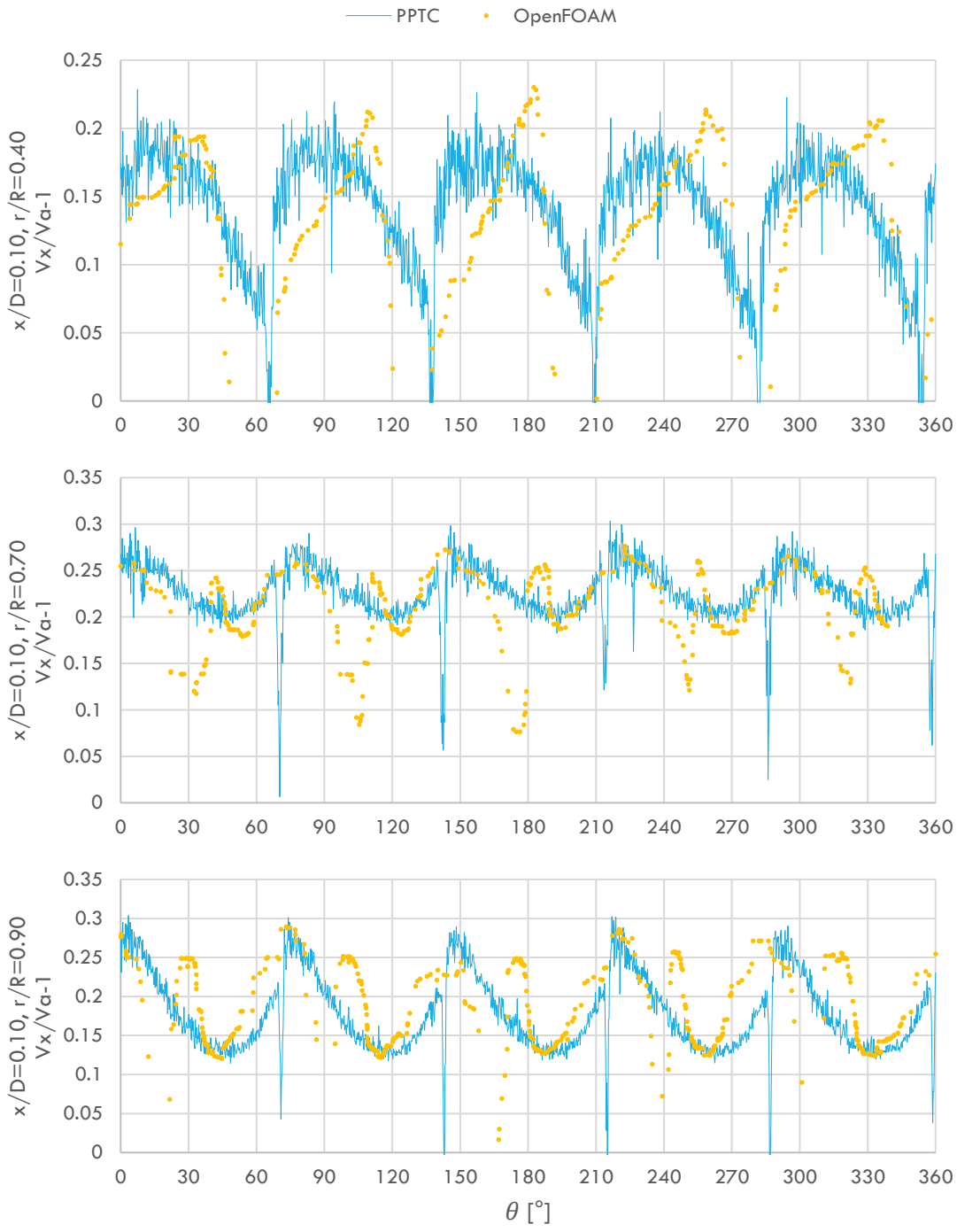

FIGURE 93 WAKE FIELD AT DIFFERENT RADIUS. COMPARING SIMULATION TO EXPERIMENTAL DATA.

Simulation agrees reasonably well with experimental data at closer distance. Father downstream the discrepancy appears to be increasing. Simulation seems to underpredict consistantly comparing to the experimental measurements (see figure below).

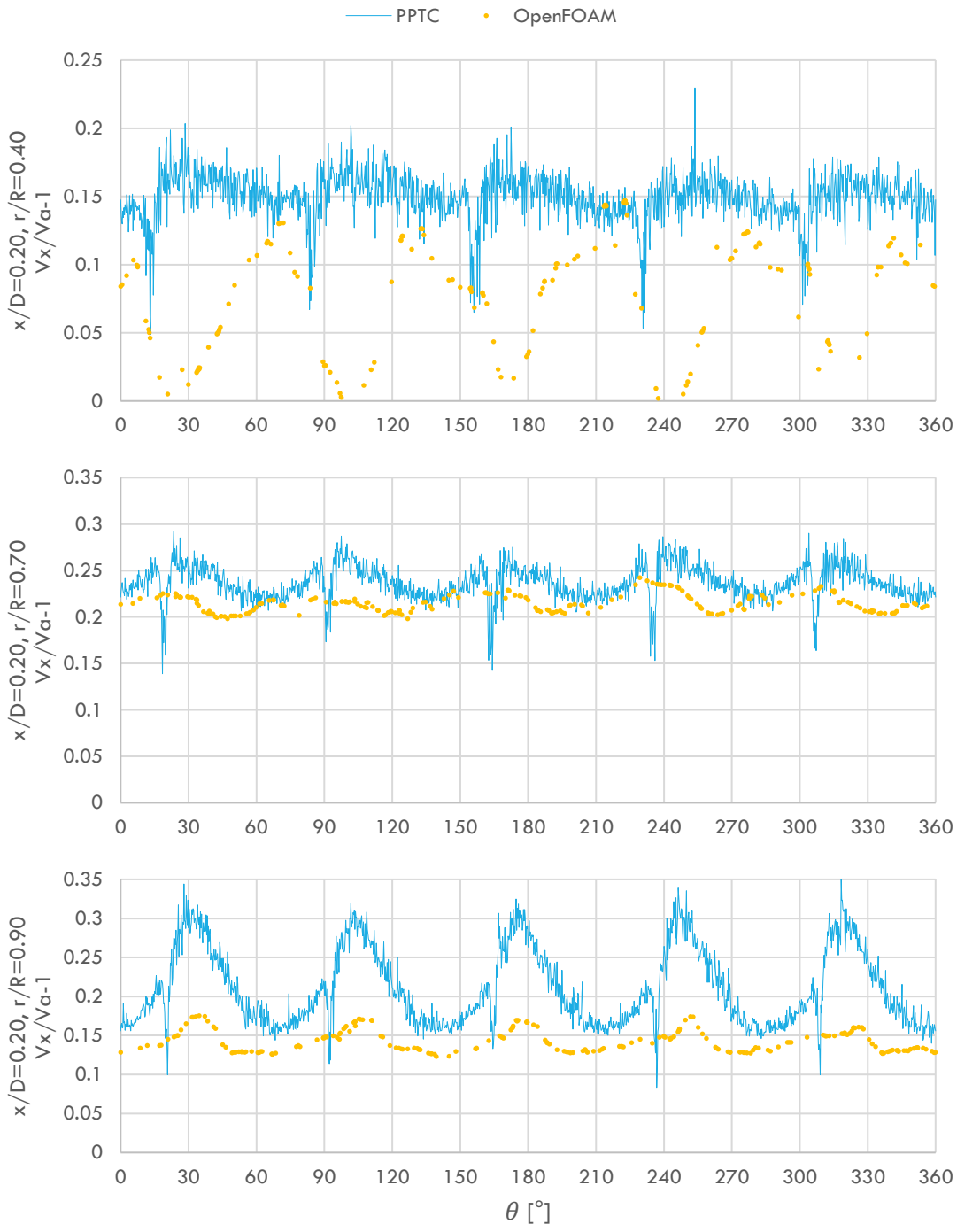

FIGURE 94 WAKE FIELD AT DIFFERENT RADIUS. COMPARING SIMULATION TO EXPERIMENTAL DATA.

3.6 Streamlines and Glyphs

Streamlines and glyphs is a useful way to visualize the flow. The two figures below illustrate the *depressed* **pressure** field and *enhanced* **velocity** field immediately after the propeller in agreement with the *actuator disk theory*. Note that the velocity field shown in the bottom figure is the magnitude. The slowing down occurs in the axial direction in front of the propeller when the flow is guided around the blades to generating lift to turn the blades in the tangential direction (remember that the cross-section of a turbine blade is an airfoil). When a propeller function as a turbine (i.e., produces power) the flow is *restricted*, and the fluid exerts a *thrust* on the propeller.

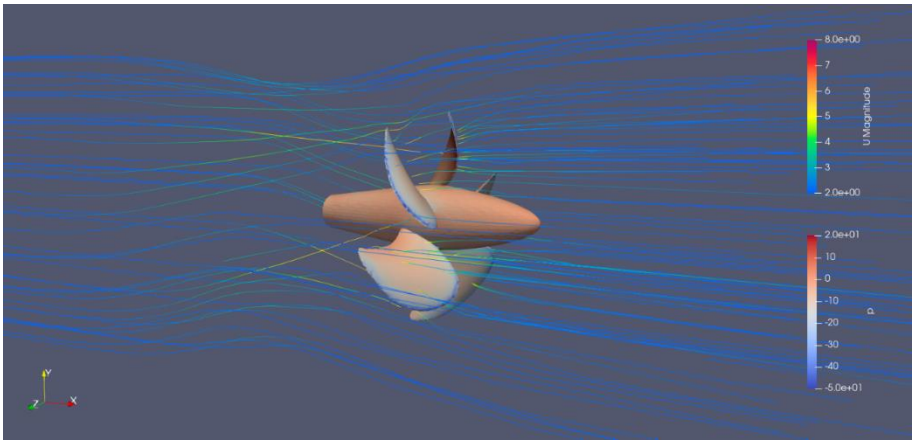

FIGURE 95 STREAMLINES GENERATED BY A SEED CLOUD UPSTREAM OF THE PROPELLER

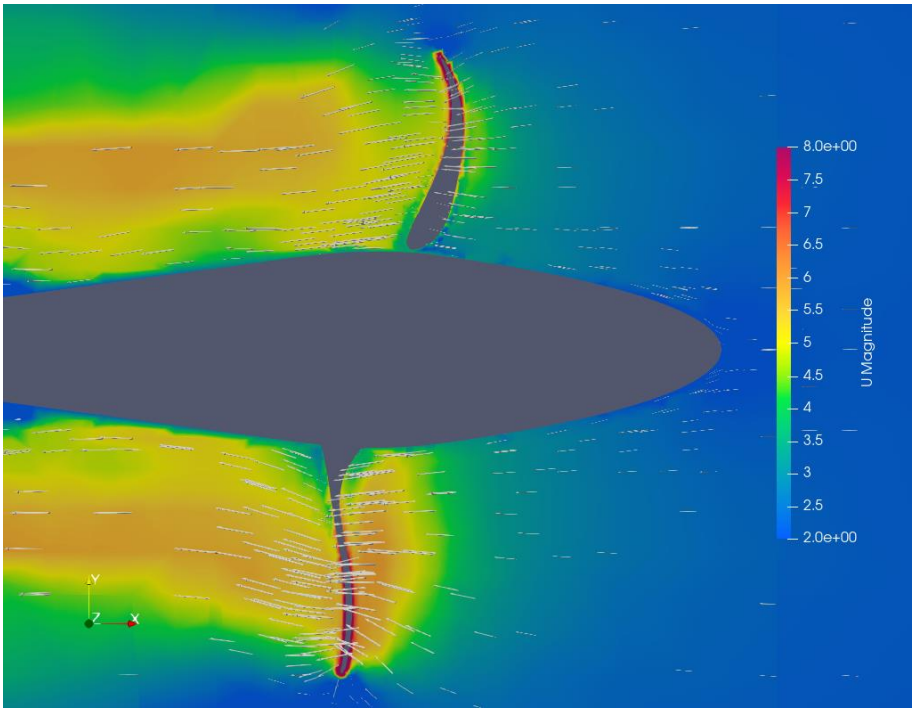

FIGURE 96 GLYPHS ADDED TO VISUALIZE VELOCITY FIELD AROUND THE PROPELLER BLADES.

4 Validation of Kite

This section is divided into three sub parts. The first is a 2D simulation of the **NACA63415** airfoil profile. It is useful to compare these results to the **XFOIL** code since it is thoroughly explored in other experimental and numerical studies. The second is a 3D simulation of the wing with the dimension calculated in the theory. That third is a 3D simulation of the kite (i.e., propeller and wing together).

4.1 2D Simulation – Airfoil

XFOIL code is based on the *panel method* and generate useful information on the *surface* of the airfoil without any information about the flow condition in the *field* surrounding the airfoil. Consequently, the computational power is significantly lower than **FOAM** but can give good information about *pressure coefficient* c_p, *lift coefficient* c_l and *drag coefficient* c_d for different *Reynold's Numbers* Re, *Mach Numbers* Ma and.N_{crit}.

4.1.1 XFOIL

4.1.1.1 Pressure Coefficient - c_p

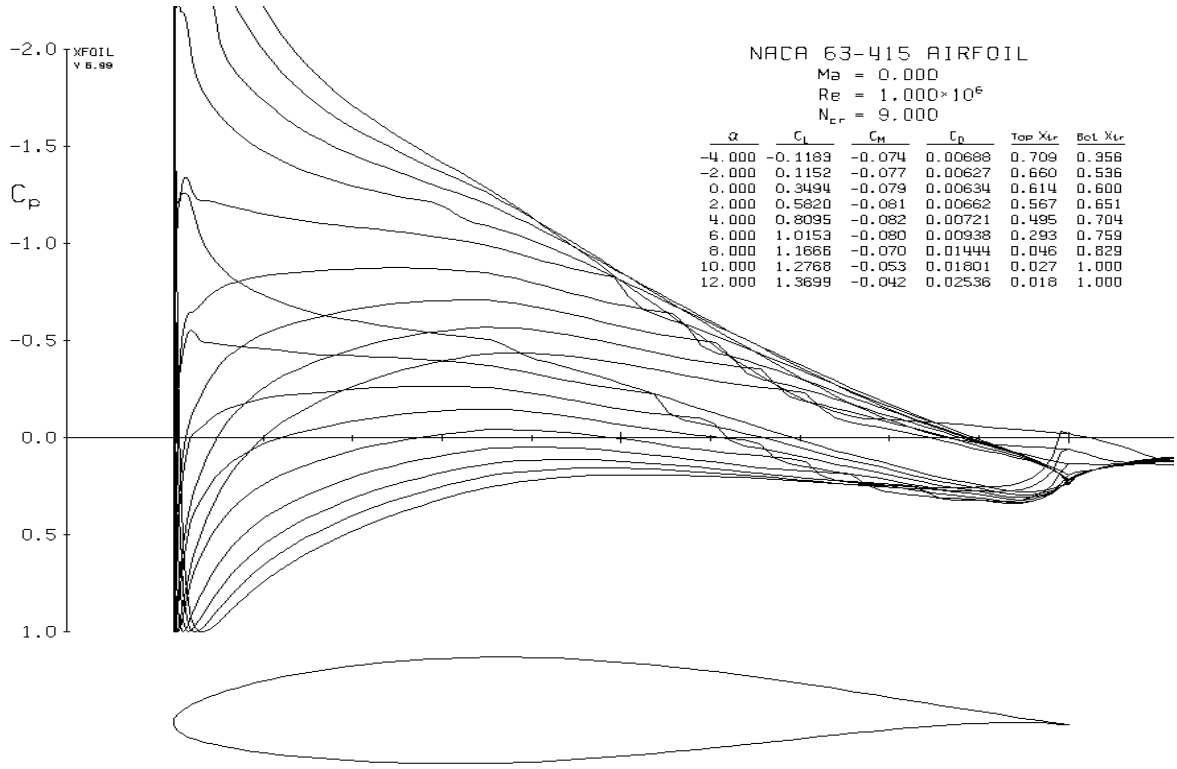

FIGURE 97 PRESSURE COEFFICIENT - c_p FOR $Re = 1e6$ AND ANGLE OF ATTACK α FROM $-4°$ TO $12°$ WITH $2°$ INCREMENTS.

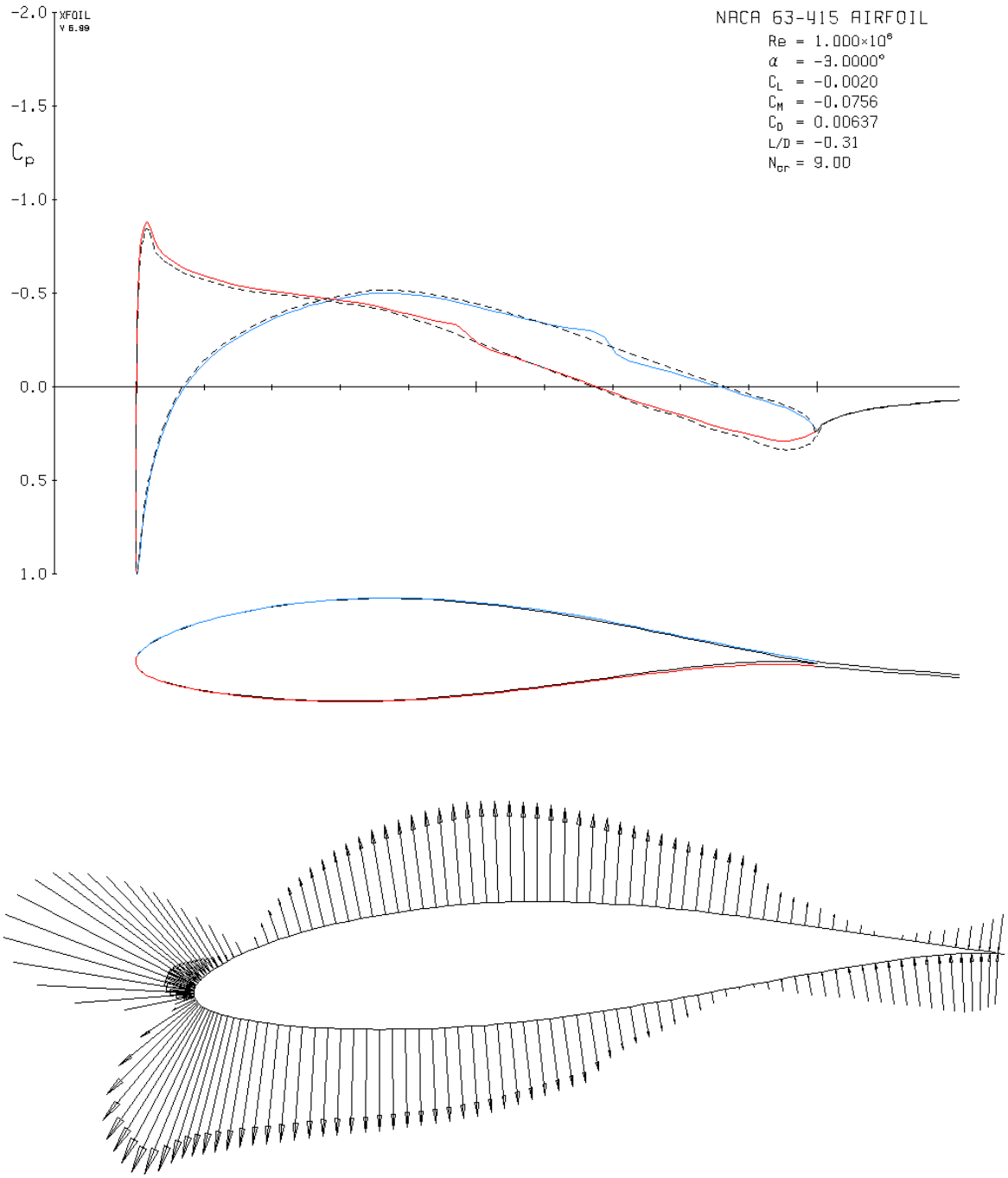

FIGURE 98 PRESSURE COEFFICIENT - c_p. REYNOLD'S NUMBER $Re = 1e6$ AND ANGLE OF ATTACK $\alpha = -3°$

Figure above illustrate the *pressure coefficient distribution* along the chord length. $\alpha_{L=0} = -3°$ is the so-called zero-lift angle of attack described in the theory. The next two figures show $\alpha = 0°$ and $\alpha = 5°$ (where lift-to-drag ratio supposed to reach its maximum). The bottom of the figures is the *vector representation* of the same distribution. Blue represents the *suction* (low pressure) side and red the *pressure* side. The *dotted lines* represent the *inviscid* flow simulation.

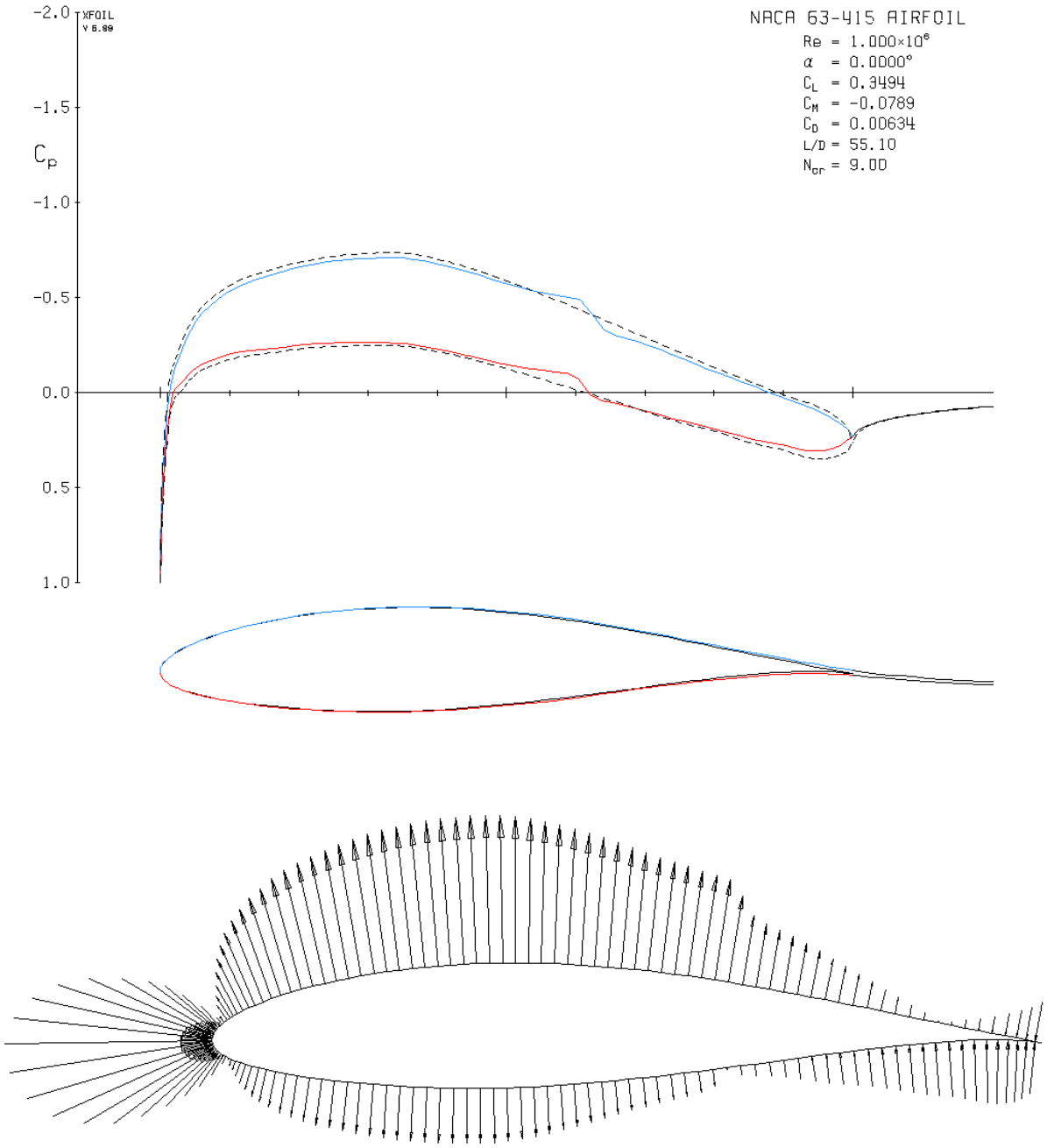

FIGURE 99 PRESSURE COEFFICIENT - c_p. REYNOLD'S NUMBER $Re = 1e6$ AND ANGLE OF ATTACK $\alpha = 0°$

XFOIL is a useful tool when the profile is known and information about flow condition is what we want to know more about XFOIL is also a useful tool in reverse, when the flow condition is known, and we want to know what profile that have those desired characteristics. This project only make use of the former, but the latter may be useful in future works.

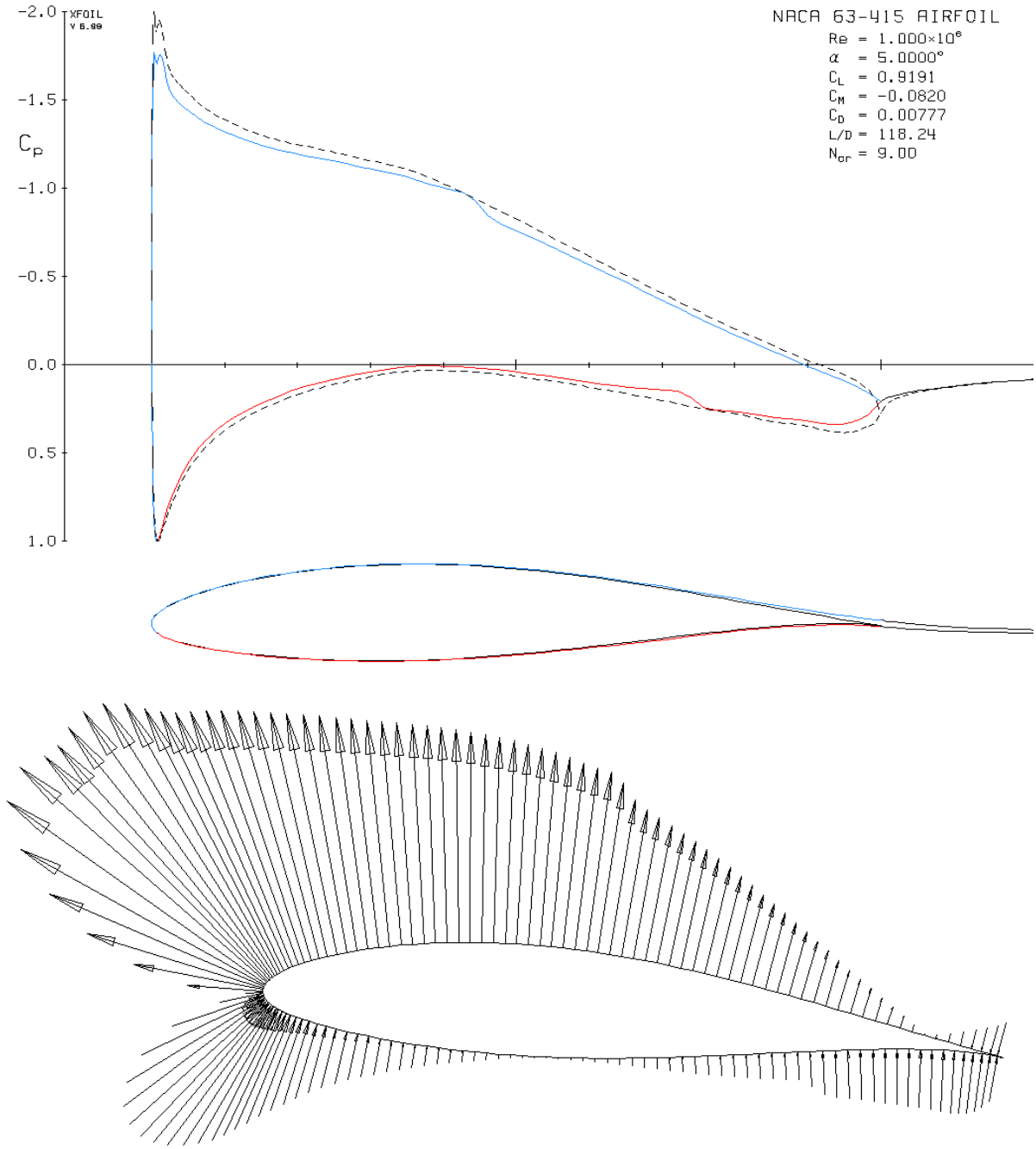

FIGURE 100 PRESSURE COEFFICIENT - c_p. REYNOLD'S NUMBER $Re = 1e6$ AND ANGLE OF ATTACK $\alpha = 5°$

An often-used validation method is to compare the pressure coefficient of the XFOIL code is compared to simulation or experiment as was done originally in [27] and more recently in [28]. Not explicitly done for this project, but the '*plot over intersection*' filter in **paraview** would be a useful tool.

4.1.1.2 Polar Plot

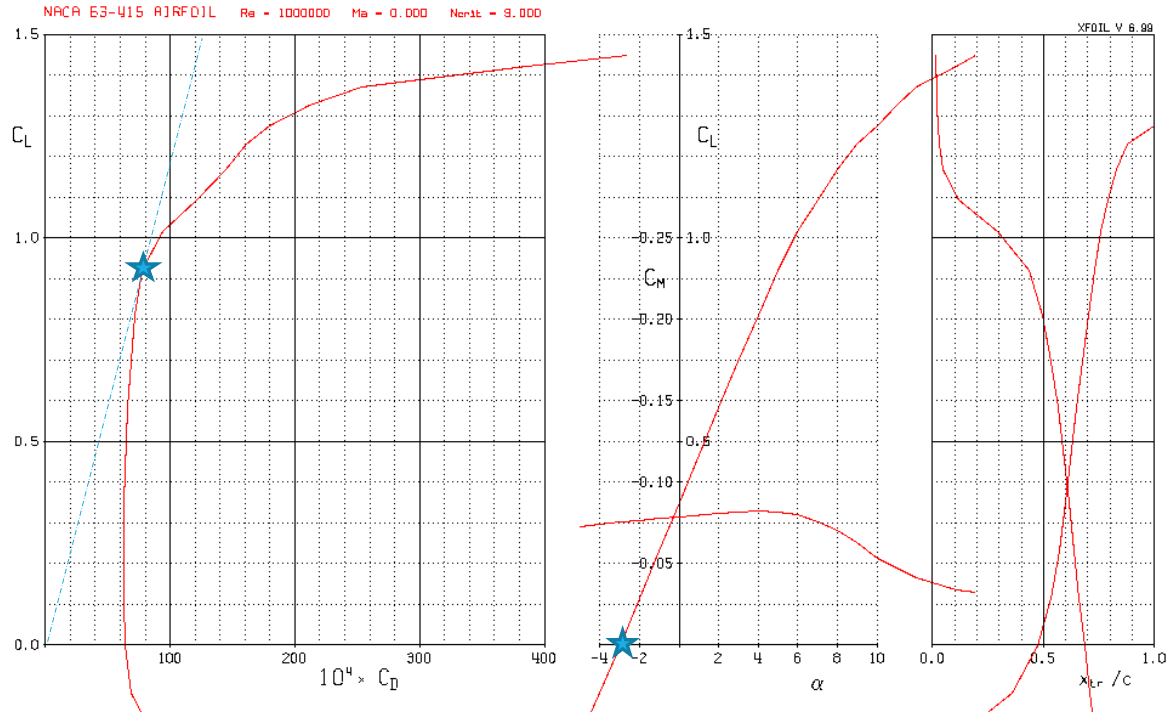

FIGURE 101 POLAR PLOT. (LEFT) c_l VS c_d. (MID) c_l AND c_m VS α. (RIGHT) TRANSITION ALONG THE CHORD LENGTH

Figure above shows the *lift coefficient* c_l, *drag coefficient* c_d and *moment coefficient* c_m. On the left *lift* is plotted against *drag*. The blue line is added to indicate the optimal *lift-to-drag ratio*, where it tangentially touches the red curve. In the middle *lift* and *moment* is plotted against *angle of attack* α. The blue star marks the *zero-lift angle of attack* $\alpha_{L=0}$. Where c_l reaches its maximum value is known as the *stall point* (not visual in the figure above). On the right, the *transition point* x_{tr} (from laminar to turbulent flow region) along the chord length is plotted against *lift coefficient* c_l. The *downward* sloping curve is the *top* surface, the *upward* sloping curve is the *bottom* surface. This information was exported and compared with the simulated values. The more useful way to plot this information is rather with angle of attack α along the x-axis for both c_l, c_d and c_l/c_d. The focus of the 2D simulation is to *extract* lift and drag coefficients to be *validated* against the XFOIL data. The first figure on the next page is the accumulation of XFOIL simulation for multiple Re. The second is a zoomed in version to better illustrate the *optimal* lift-to-drag ratio. Note how the optimal lift-to-drag ratio shifts to lower α for increasing Re. By widening the α range to 25°, the *stall point* is now visible at the max c_l.

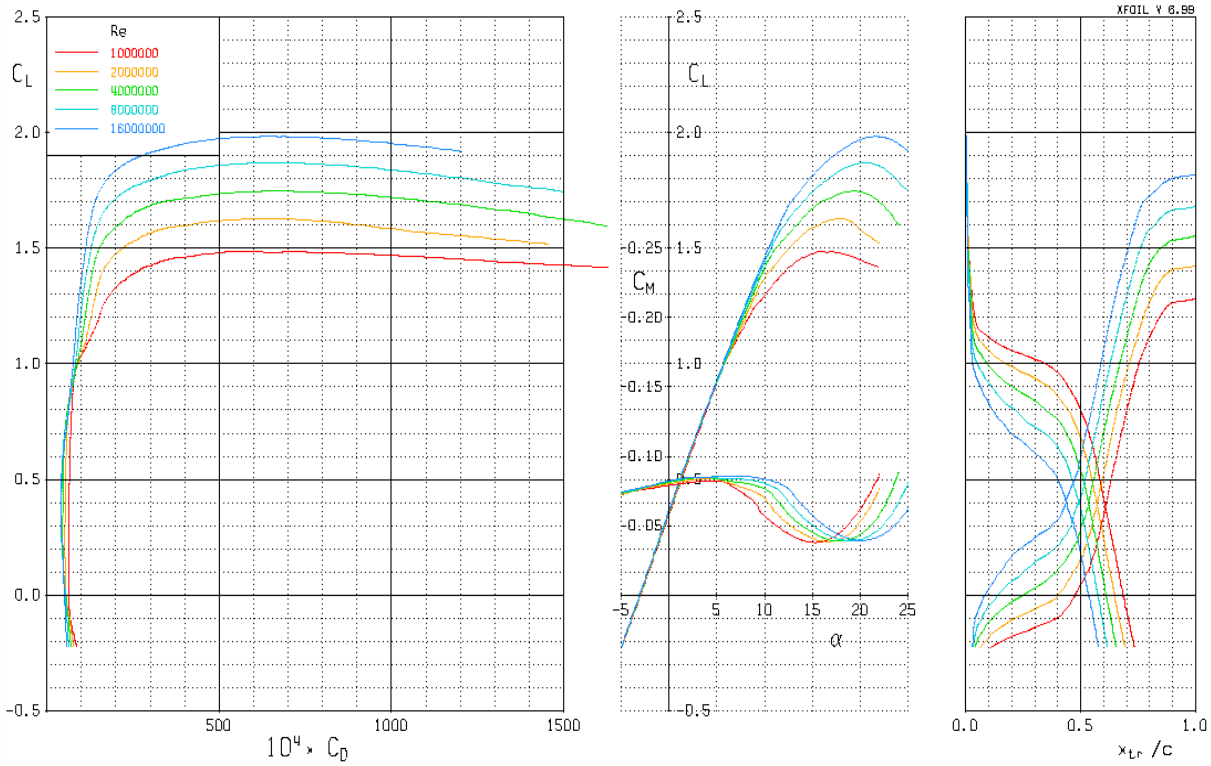

FIGURE 102 POLAR PLOTS FOR MULTIPLE Re

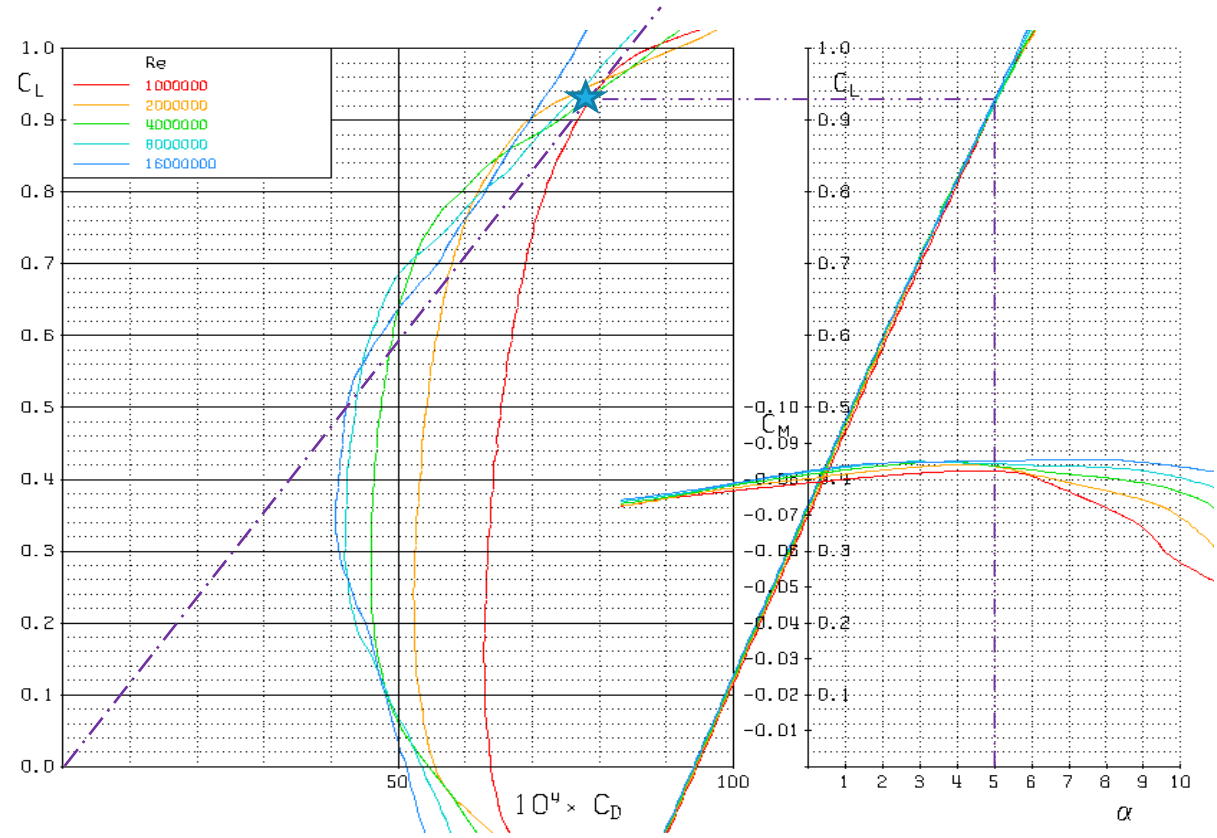

FIGURE 103 ZOOMED IN POLAR PLOT FOR MULTIPLE Re

4.1.2 Computational Setup

The **OpfenFOAM** version 8 *wingMotion Tutorial* was used as a starting point. The coordinates for the **NACA63415** profile were downloaded from **UIUIC** *Airfoil Coordinates Database* [31]. The profile was extruded in Inventor to produce **.obj** files to be used with **sufraceFeaturesDict**, **extrudeMeshDict** and **snappyHexMeshDict** in OpenFOAM. kLowReWallFucntion for k, omegaWallFunction for ω and nutkWallFunction for ν_t was used. Initial values are summarized in the table on the next page.

4.1.2.1 Geometry

Like the propeller simulation the domain size was kept though a rectangular geometry was adopted instead of cylinders. A refinement box around the airfoil was used to step up the refinement level intermediately before the final surface refinement.

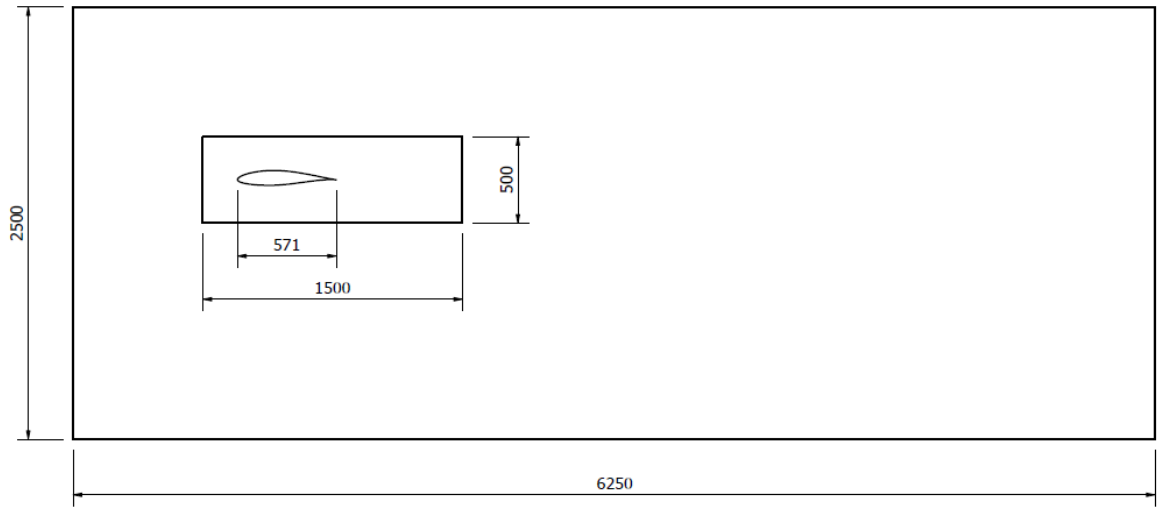

Background mesh was first generated with **blockMesh** using 50 cells in x direction, 20 and 24 in y and z direction, respectively. This was about the medium mesh used for the propeller simulation. Level 3 was used inside the refinement box and level 6 was used on the airfoil section surface in **snappyHexMesh**. 7 *layers* was also *added* with the final layer 0.7 of the surrounding mesh size and 1.35 expansion ratio. The cell count is 331 along the airfoil.

4.1.2.2 Mesh

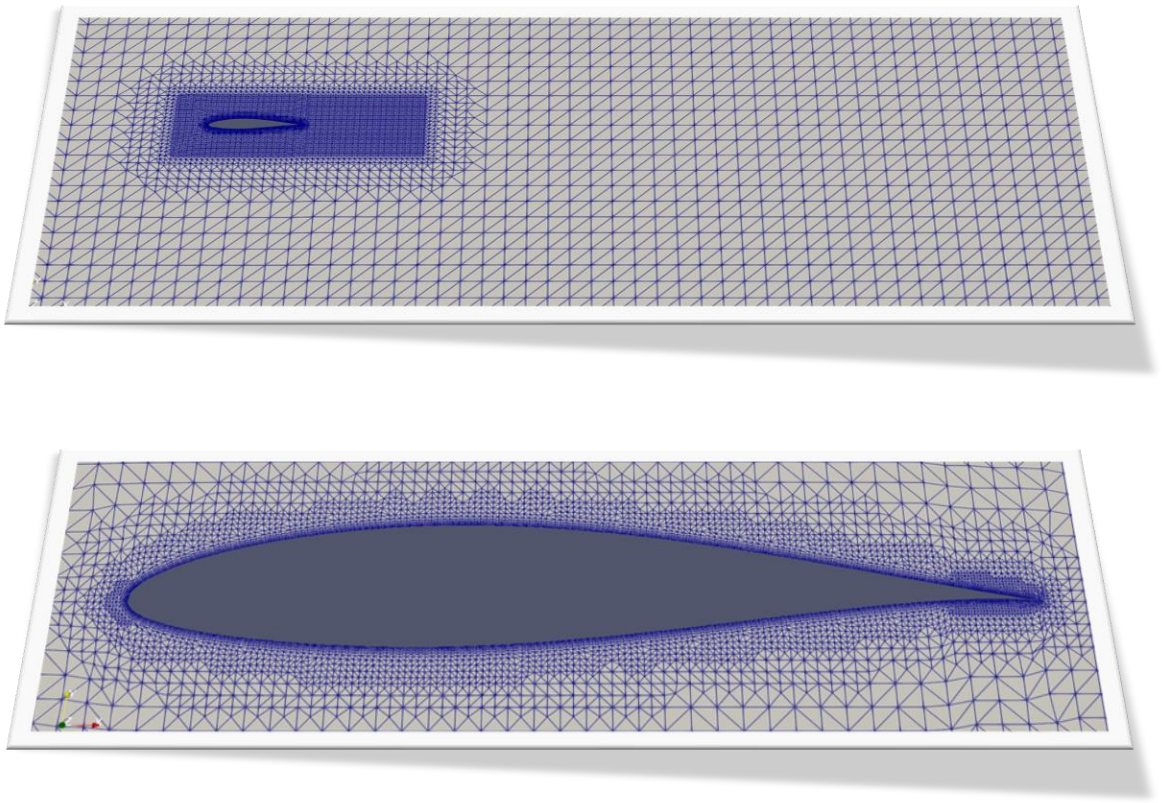

4.1.2.3 Solver

To solve this *steady-state* 2D airfoil case the **foamSimple** solver was used.

4.1.2.4 Initials

As before the **0 folder** contains all the initial values for the variable we are solving for. Values for Re, k and ω were calculated for each apparent velocity V_A. The characteristic length is now the chord length, $L = 0{,}571\,m$. Table below is summery. Rotation speed $w\,[rad/s]$ is included here but not used until the last sub part, 3D simulation of Kite.

TABLE 6 INITIAL VALUES FOR V_A, Re, k, ω, AND w

$V_A[m/s]$	Re	$k\,[m^2/s^2]$	$\omega\,[s^{-1}]$	$w\,[rad/s]$
23.00	7,983,653	7.9350E-02	4.8272E+04	444.7
20.00	6,942,307	6.0000E-02	3.6501E+04	386.7
10.00	3,471,154	1.5000E-02	9.1252E+03	193.3
5.00	1,735,577	3.7500E-03	2.2813E+03	96.7
2.88	1,000,000	1.2449E-03	7.5735E+02	55.7

4.1.3 Results

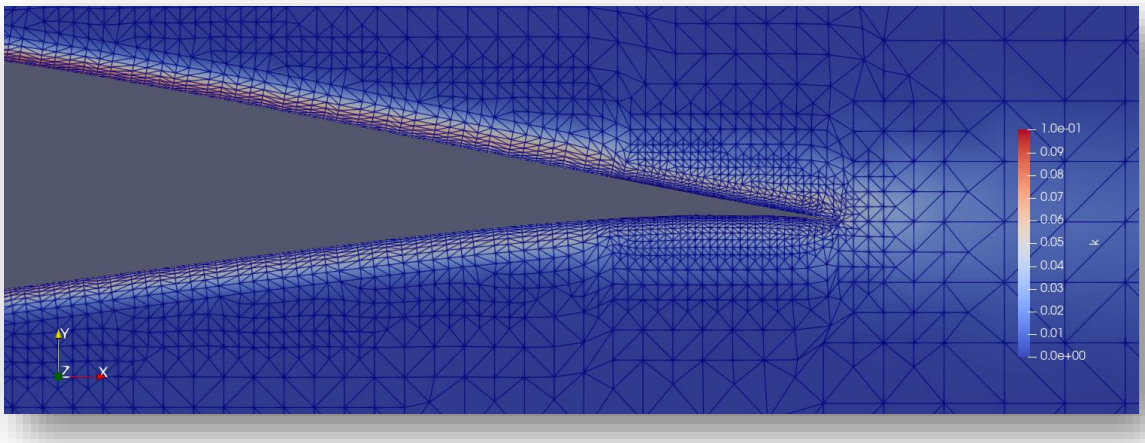

FIGURE 104 TURBULENT KINETIC ENERGY – k

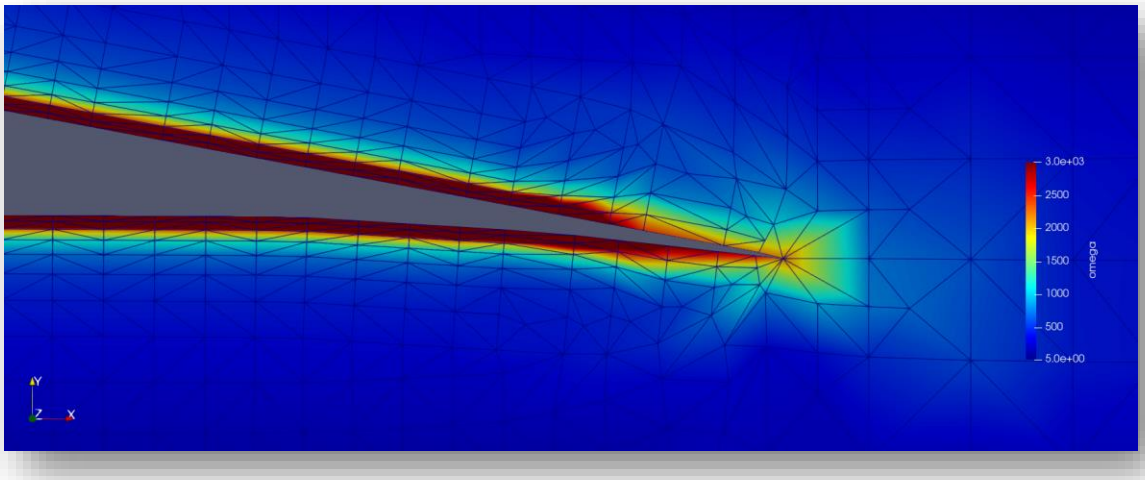

FIGURE 105 TURBULENCE FREQUENCY – ω

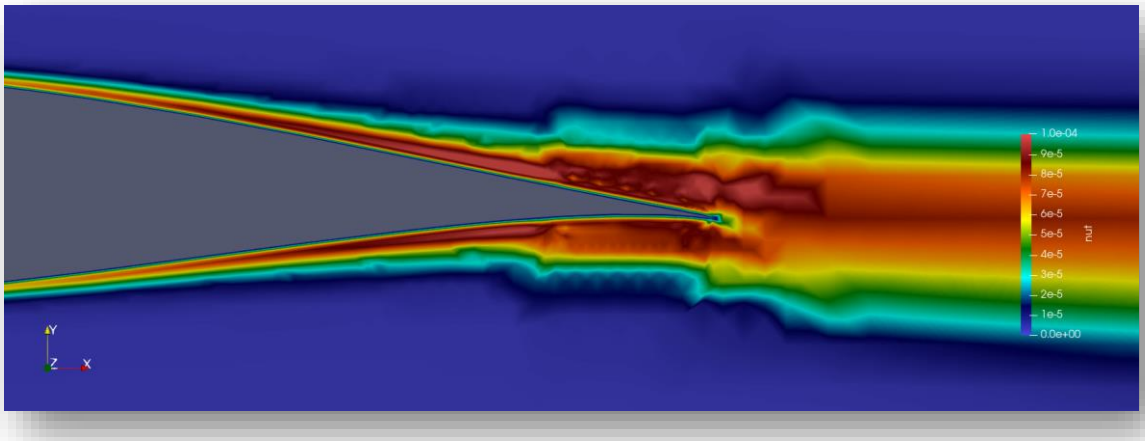

FIGURE 106 TURBULENCE EDDY VISCOSITY – ν_t

For $Re = 1e6$ and $\alpha = 0°$ there is no separation of the flow or recirculation bubbles at the trailing edge. The figures on the previous page show how the no-slip condition between the fluid and the airfoil surface is causing turbulence. The k field show where the turbulence is generated. The ω field shows that the dissipation rate is also highest at the same places. Consequently, the kinetic energy carried in the turbulence seems to dwindle relatively quickly after leaving the trailing edge. The eddy viscosity on the other hand seems to persist farther downstream and do not seem to dissipate significantly for the remainder of the simulation domain. This is most likely the excessively coarse mesh resolution. Since the interest is not so much about the wake field the mesh resolution downstream is structured very low and do not allow for eddy mixing to occur in any meaningful way.

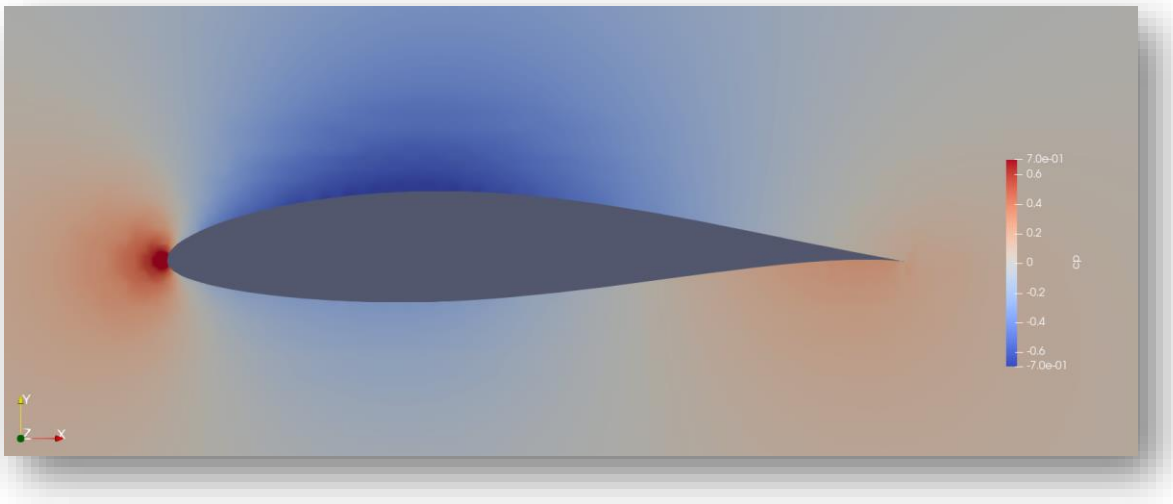

FIGURE 107 PRESSURE COEFFICIENT – c_p

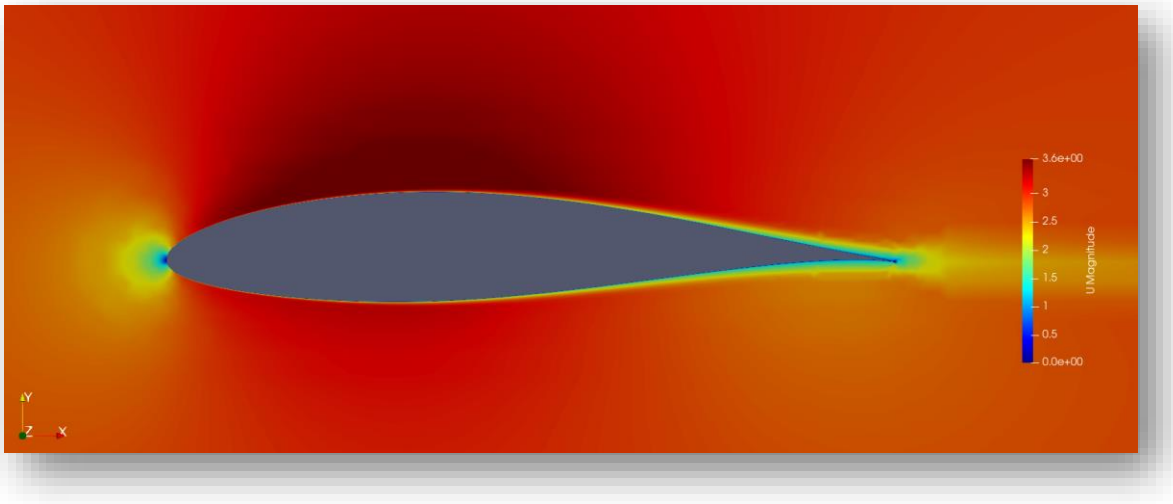

FIGURE 108 VELOCITY MAGNITUDE – U

The pressure and velocity field in the two preceding figures show how lift and drag is generated around an airfoil. The higher velocity on the upper surface causes the pressure to be lower on the suction side of the airfoil. Since the total pressure is constant along a streamline, when dynamic pressure $\frac{1}{2}\rho V^2$ increases the static pressure reduces correspondingly. The figure below shows the y^+ value along the airfoil surface. Highest value is located at the top and bottom where the velocity is highest. When the layers were added during mesh generation, the layers where extruded uniformly along the surface so it makes sense for y^+ to be highest here. Note however that the y^+ value is under 30 for the whole surface. This is not always the case for increasingly higher Re and α.

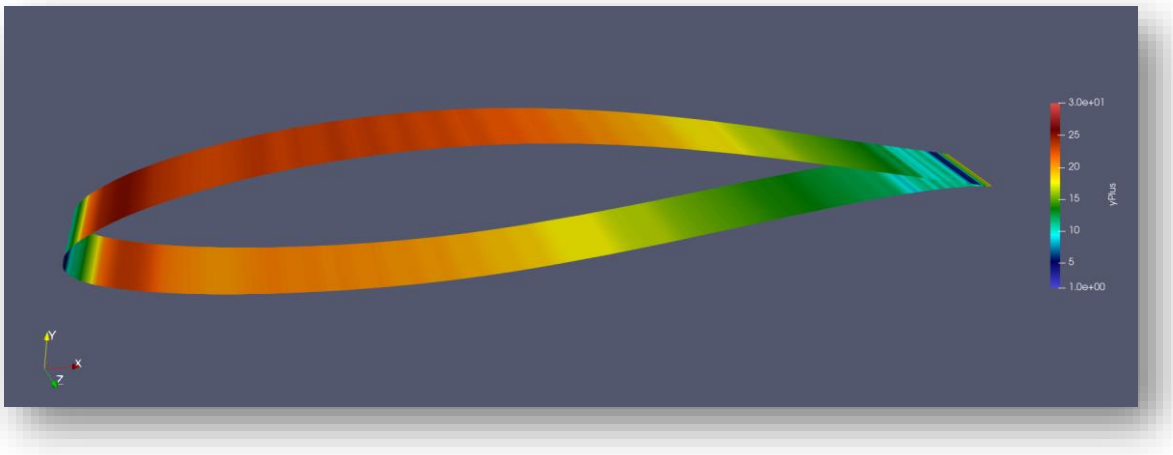

FIGURE 109 YPLUS - y^+

Figure below shows *separation flow* and *recirculation bubble* at the trailing edge when Re and α are sufficiently high. Interesting to note how the k field is higher outside the bubble.

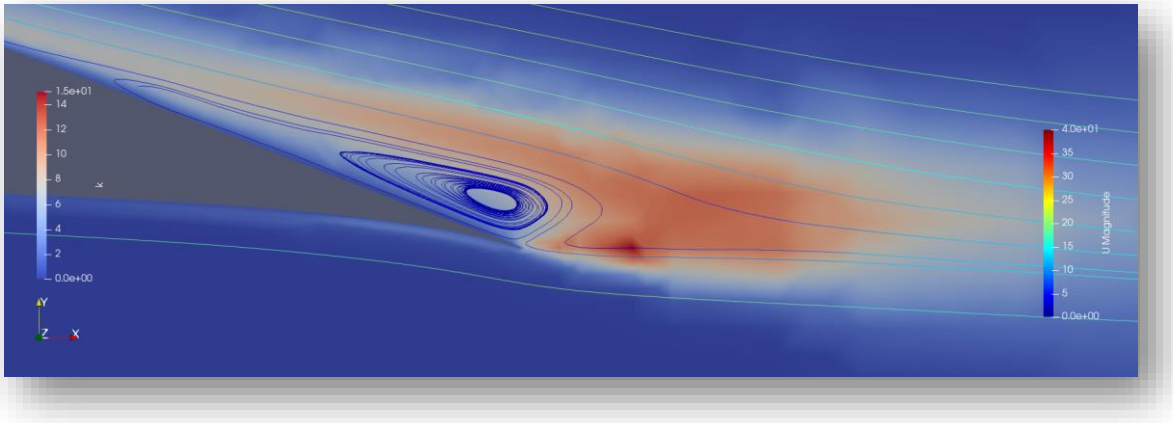

FIGURE 110 TURBULENT KINETIC ENERGY AND VELOCITY STREAMLINES, $Re = 6e6$, $\alpha = 10°$.

4.1.4 Lift Coefficient, Drag Coefficient and Lift-to-Drag Ratio

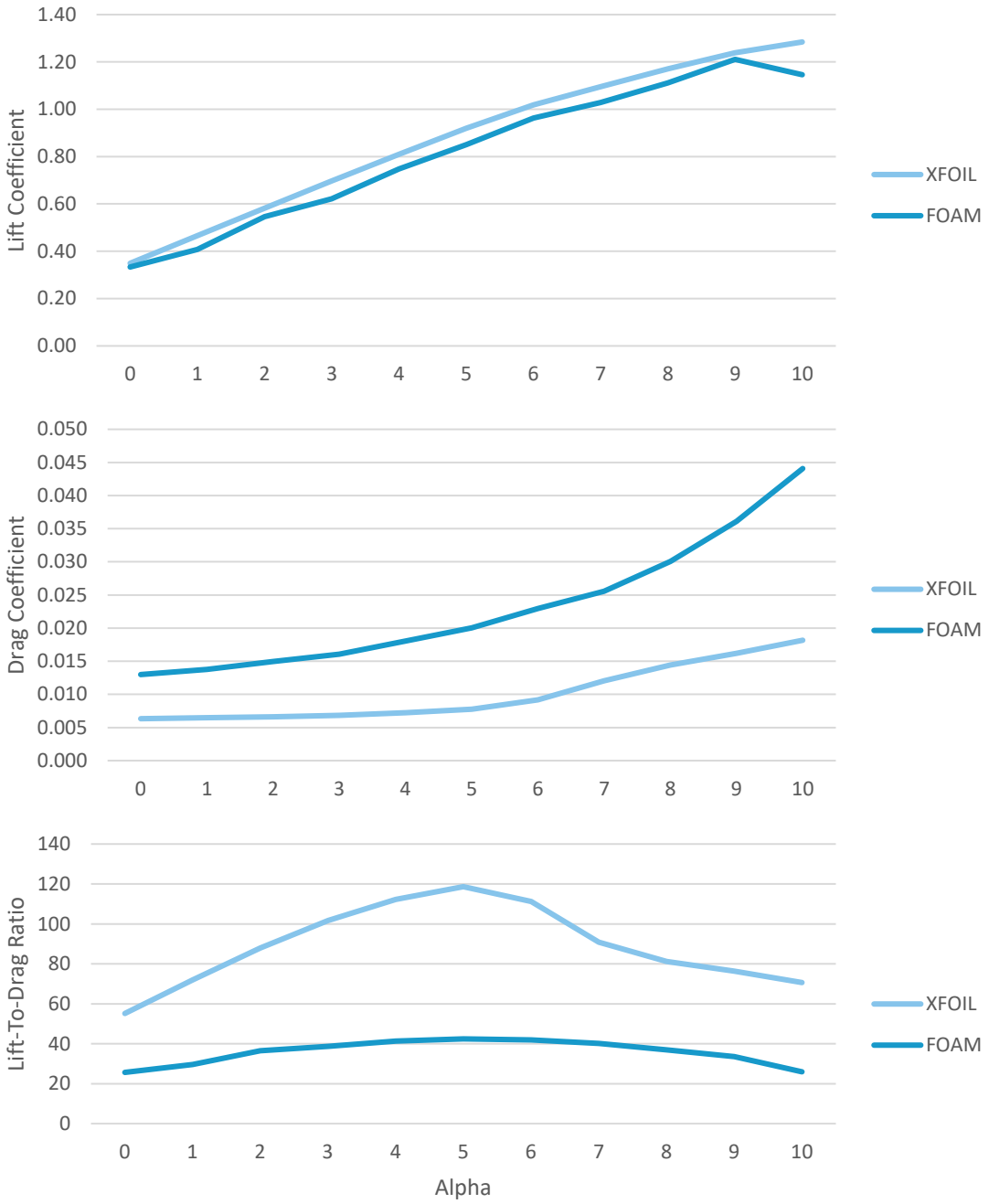

FIGURE 111 COMPARING XFOIL TO FOAM FOR $Re = 1e6$

FOAM agrees well with XFOIL on lift coefficient but seems to over-predict drag coefficient. The discrepancy appears to increase with increasing angle of attack α. The optimal lift-to-drag ratio occur at $\alpha = 5°$ but FOAM predict a third of the XFOIL value.

4.2 3D Simulation – Wing

The same mesh refinement and initial values was used in the 3D simulation as was used in the 2D simulation. The case is still a *steady-state* case and the **foamSimple** was again used. Additional section of **streamlines** over the wing and **wing tip vortices** are included in the results in this sub part.

4.2.1 Computational Setup

4.2.1.1 Geometry

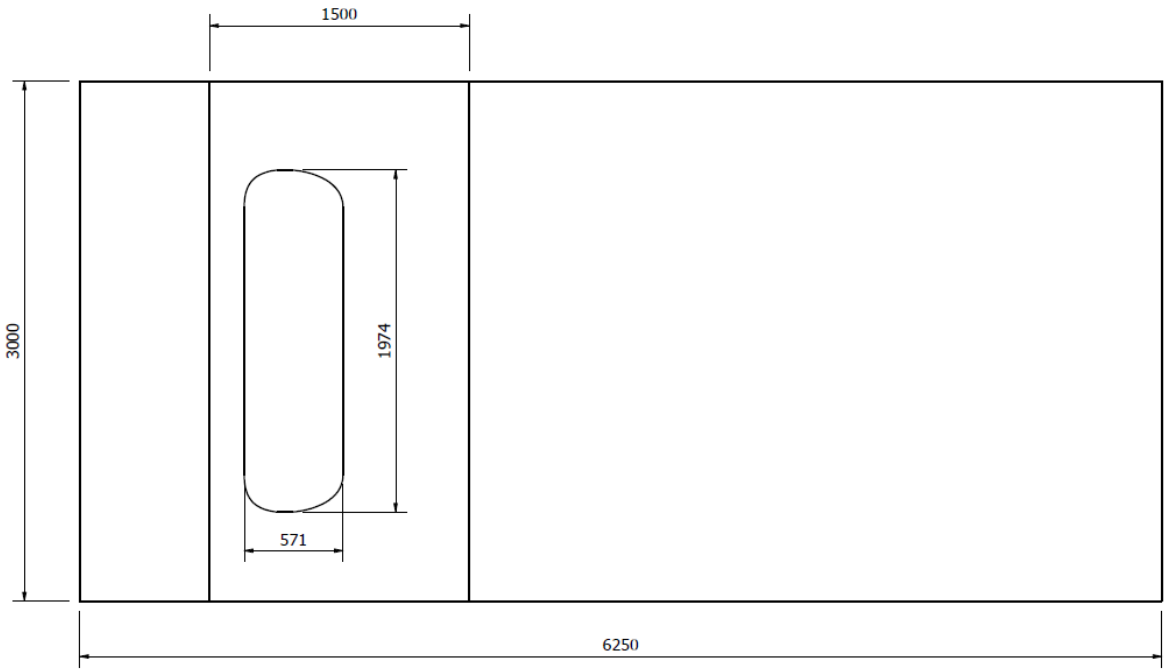

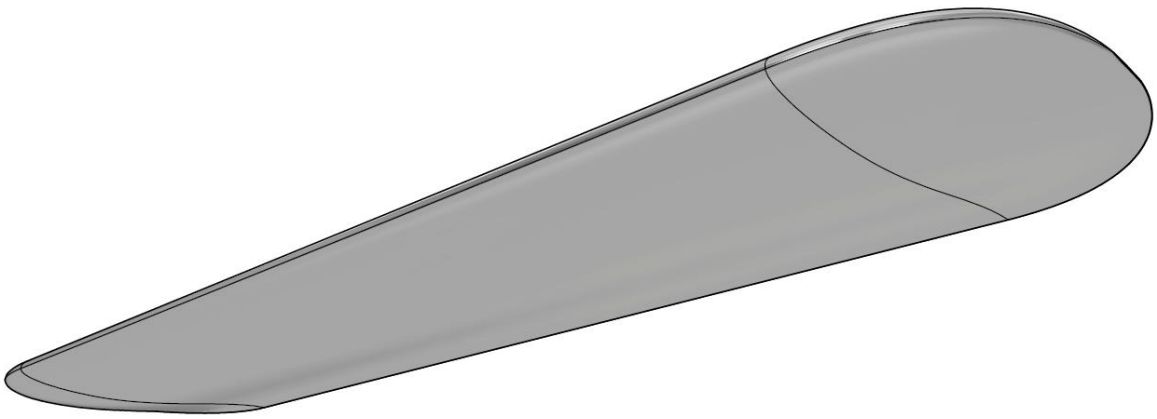

4.2.1.2 Mesh

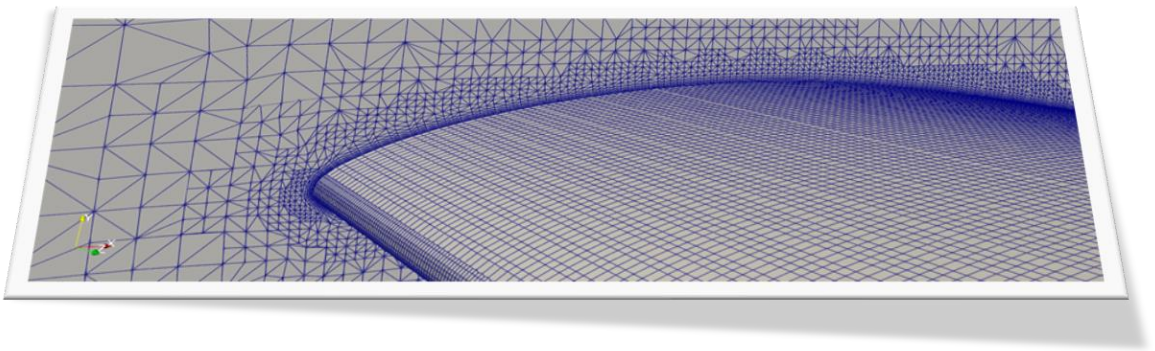

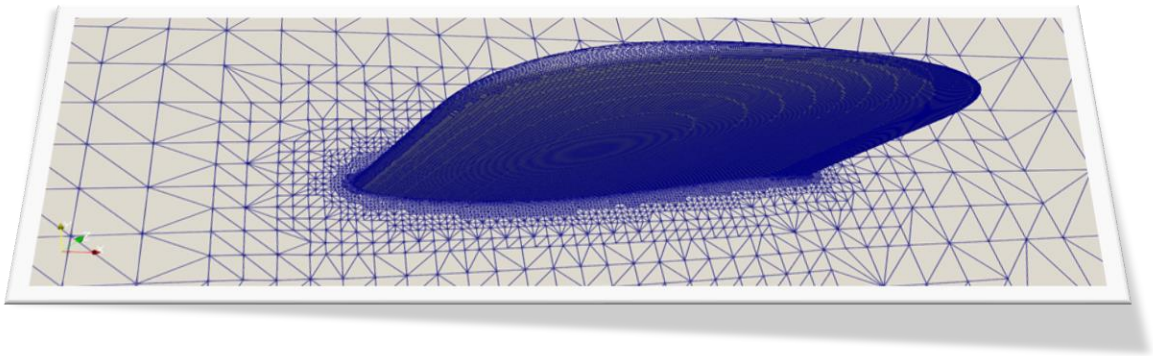

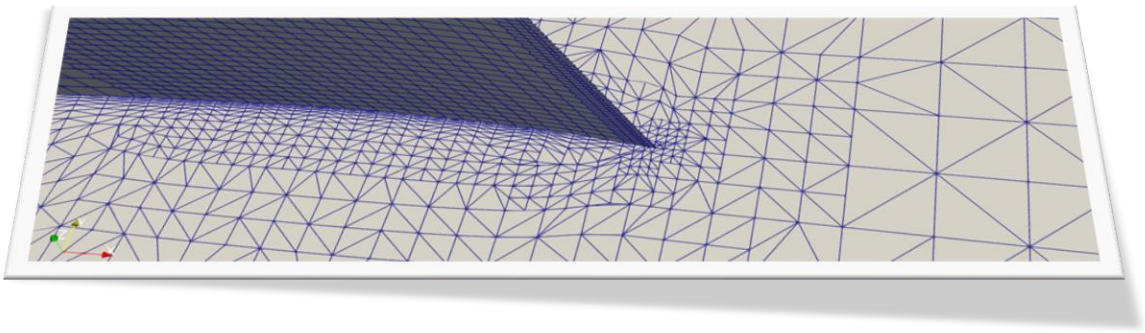

The results shown in the following section seems to repeat the trends shown in the 2D simulation. Note however the slightly higher y^+ values especially around the wing tip. For most of the wing the value is below 300 but above 50 at some spots where the meshing seems to struggle to generate sufficient layers (also 200 at the max). The snappyHexhMesh **log file** indicate only 83.6 % coverage of the layering, which is less than ideal but within acceptable range.

4.2.2 Results

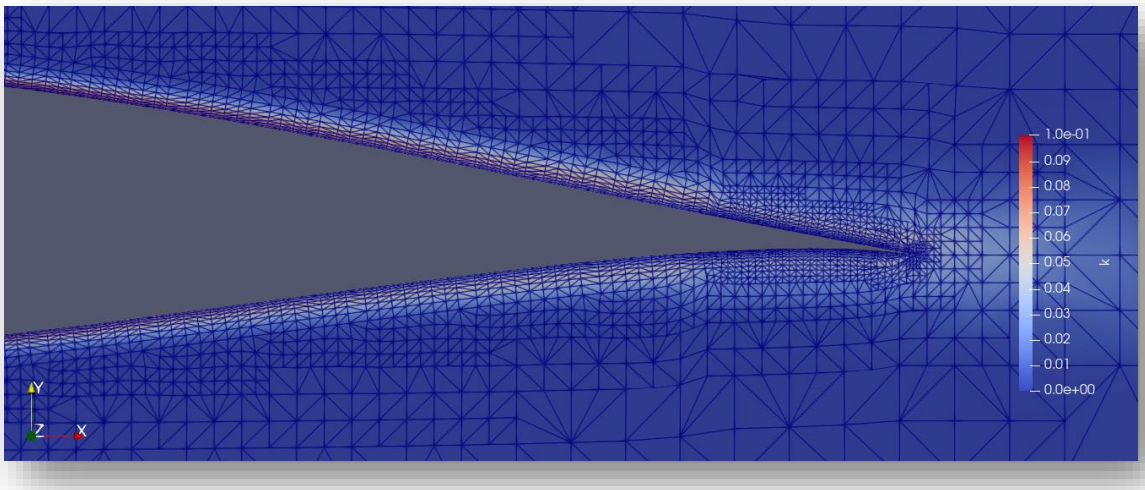

FIGURE 112TURBULENT KINETIC ENERGY – k

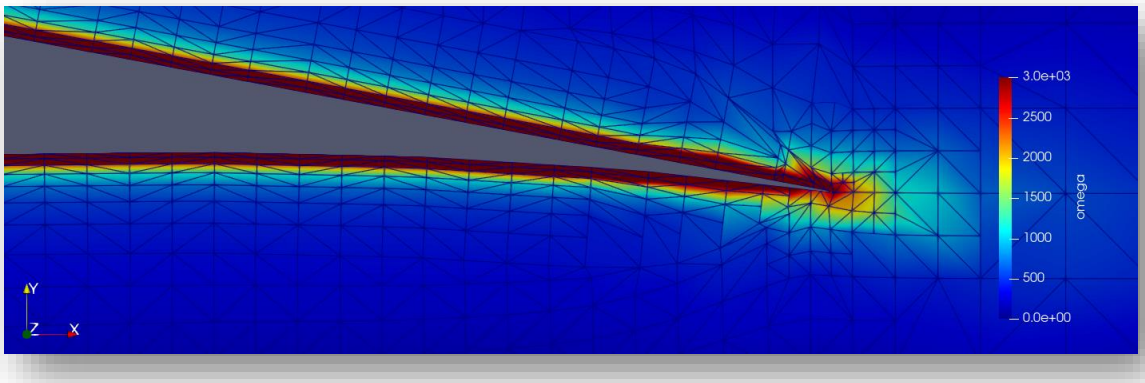

FIGURE 113TURBULENCE FREQUENCY – ω

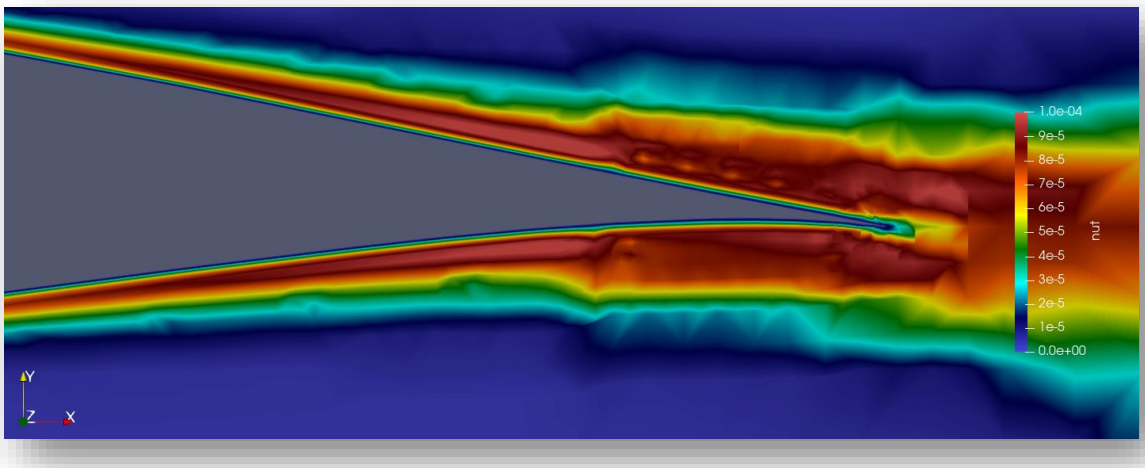

FIGURE 114TURBULENCE EDDY VISCOSITY – ν_t

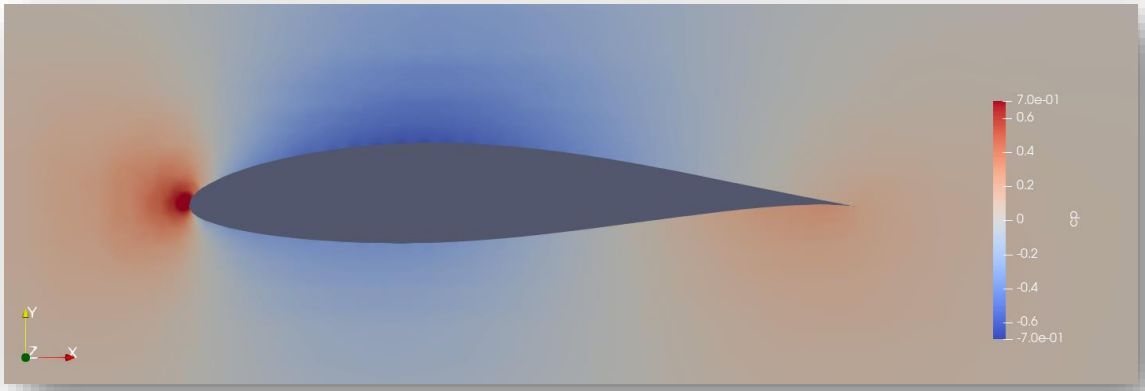

FIGURE 115 PRESSURE COEFFICIENT – c_p

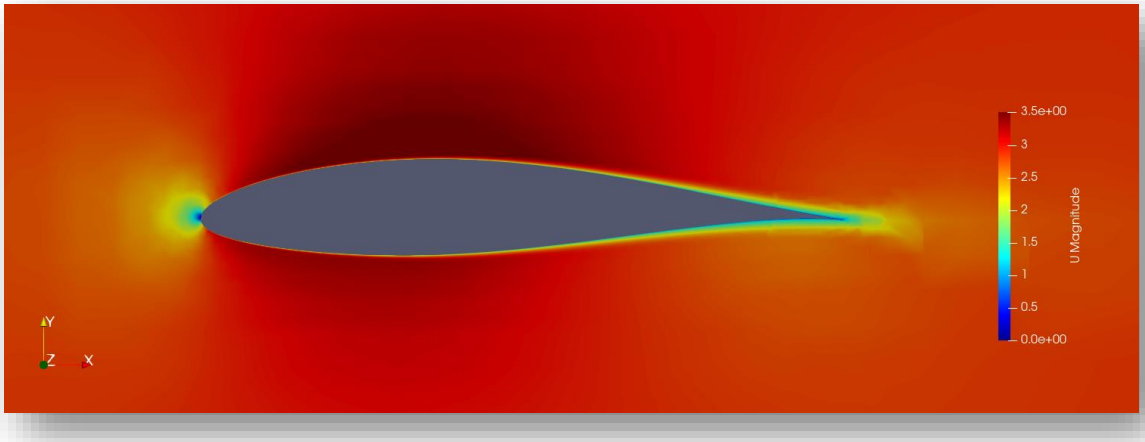

FIGURE 116 VELOCITY MAGNITUDE – U

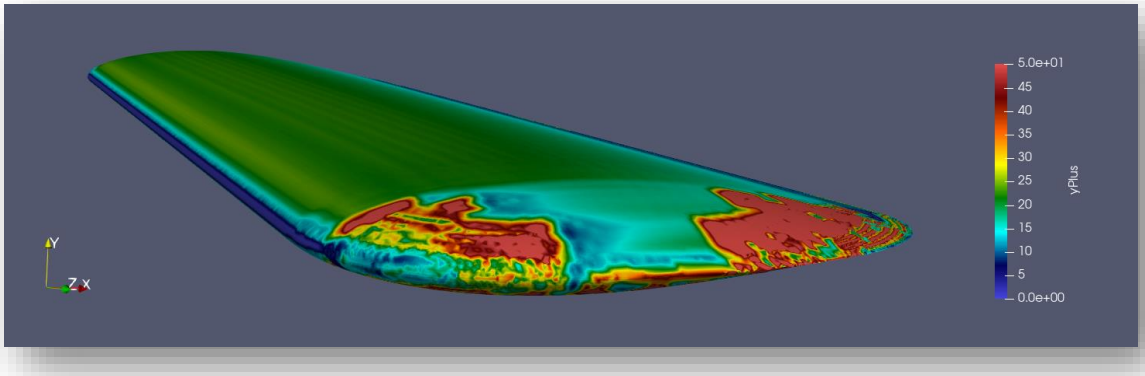

FIGURE 117 YPLUS – y^+

4.2.2.1 Streamlines

$Re = 1e6$ and $\alpha = 10°$. Seed **Line** (-0.35 0.21 +-1.5). Resolution 50.

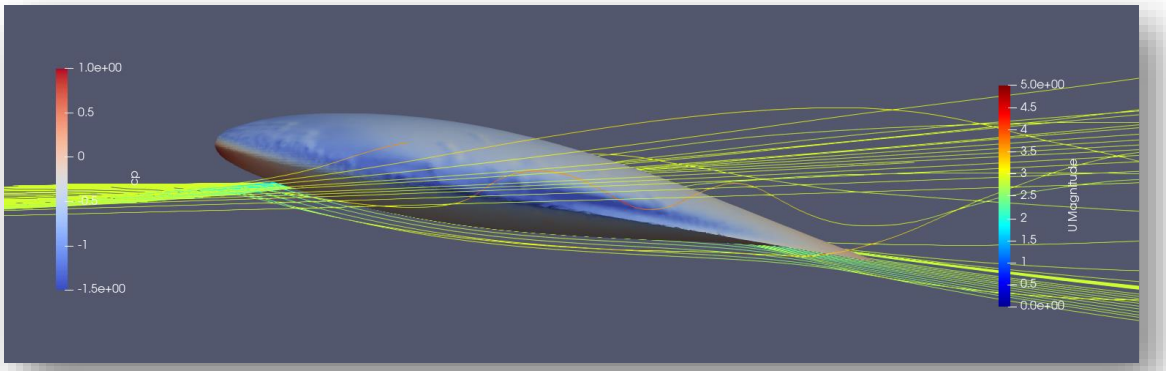

FIGURE 118 SIDE VIEW

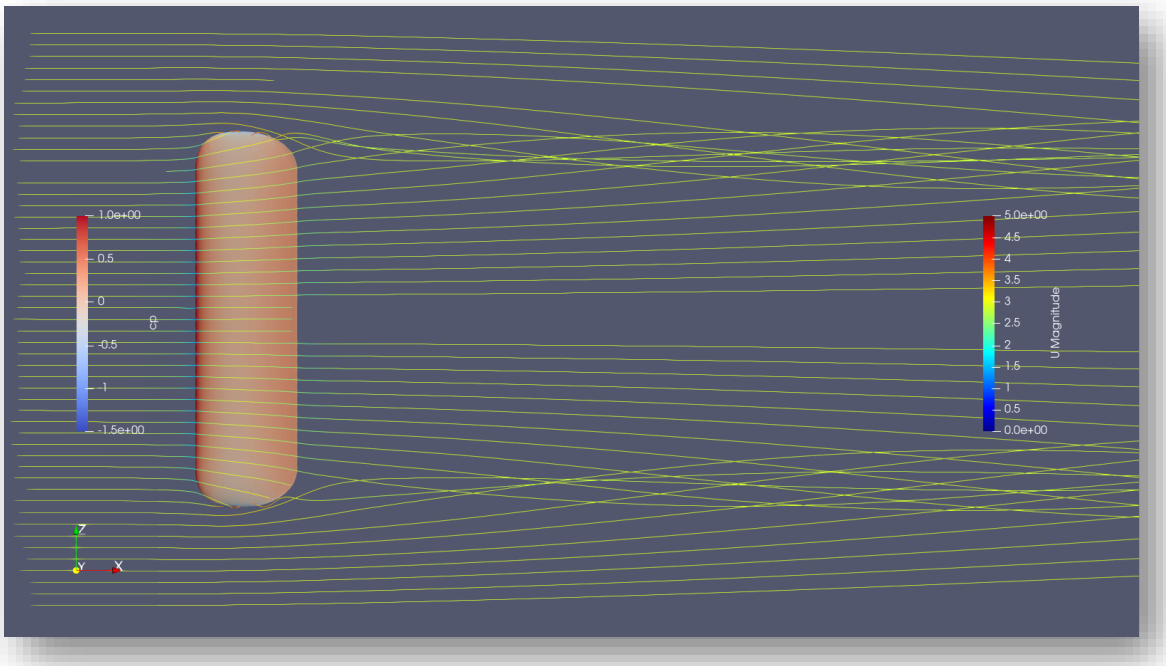

FIGURE 119 BOT VIEW

The two figures above show the spanwise motion of a finite wing. On the pressure side the motion tends towards the wing tips and opposite on the suction side (i.e., away from the tips). These opposing tendencies on each side (i.e., pressure and suction side) of the wing causes vortices to occur at wing tips.

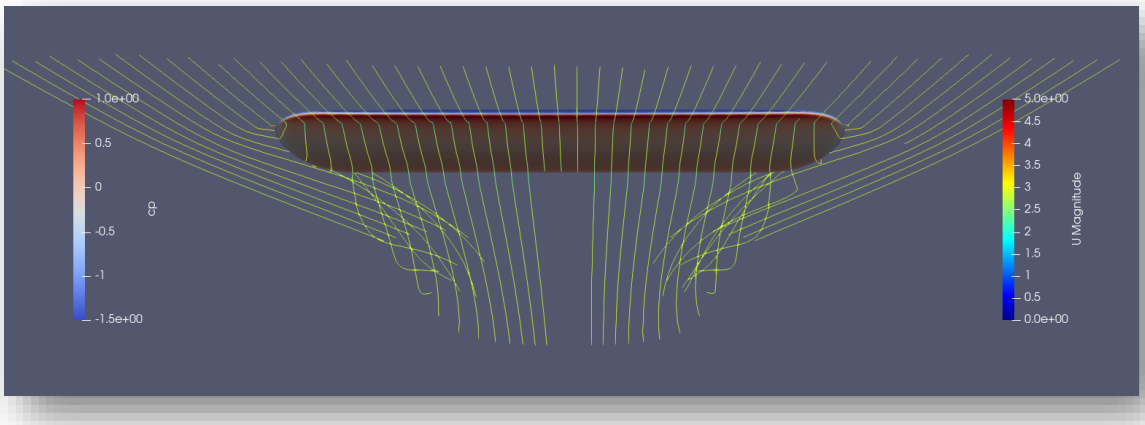

FIGURE 120 BENEATH VIEW

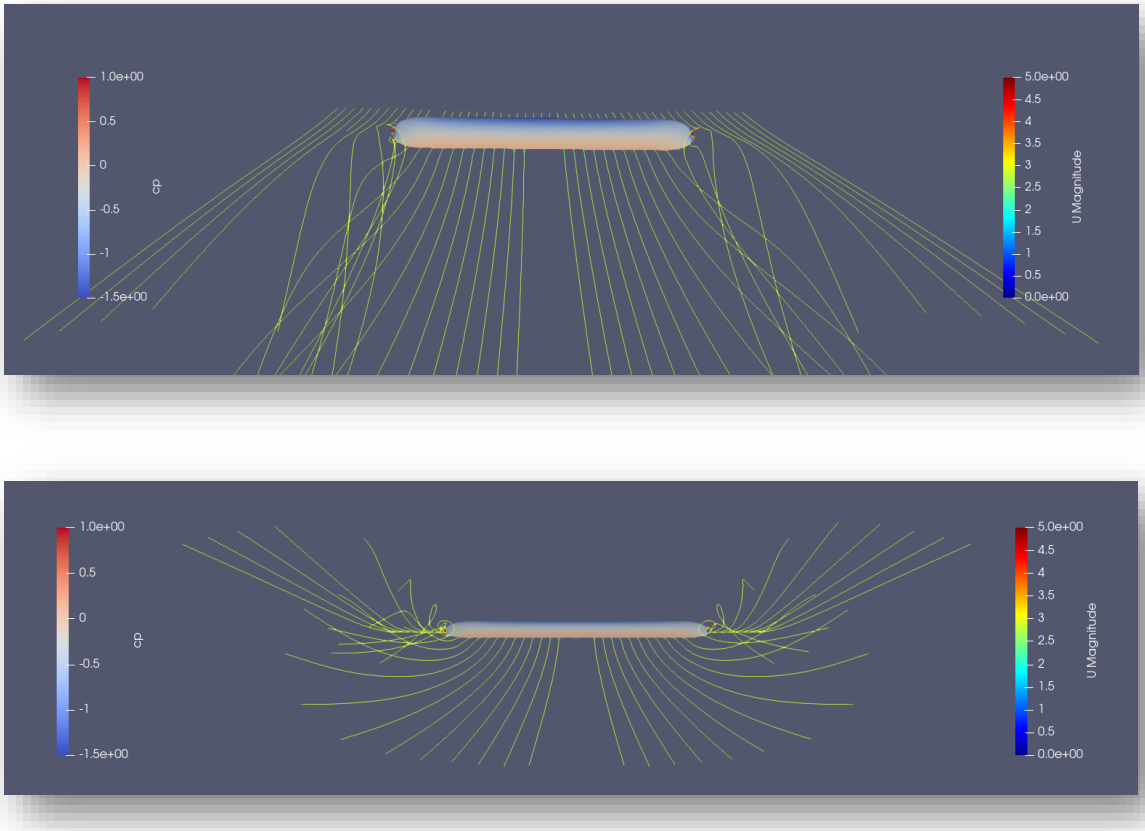

FIGURE 121 BEHIND VIEWS

From beneath and behind these vortices is clearly observed. These spanwise motion, downward downwashes and wing tip vortices are the main causes for the discrepancies between the airfoil and finite wing. Using a seed point instead of a line illustrates this even better in the subsequent images on the following pages.

Seed **Point** (-0.35 0.25 0.9) Radius 0.15. Resolution 50.

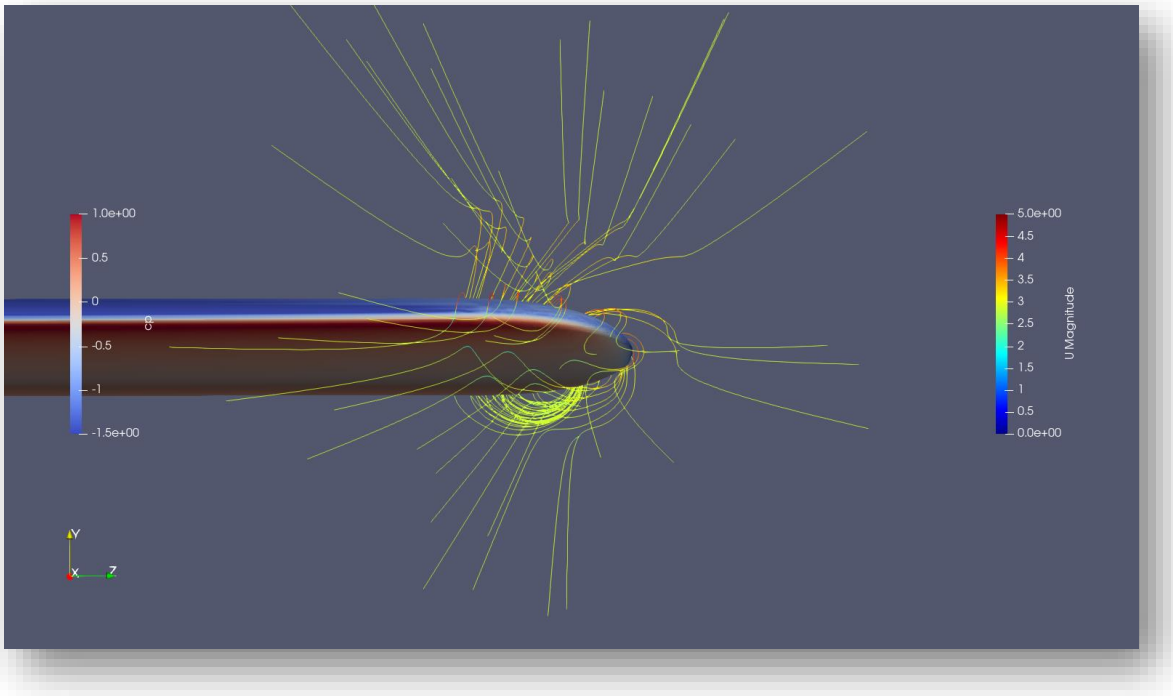

FIGURE 122 FRONT VIEW

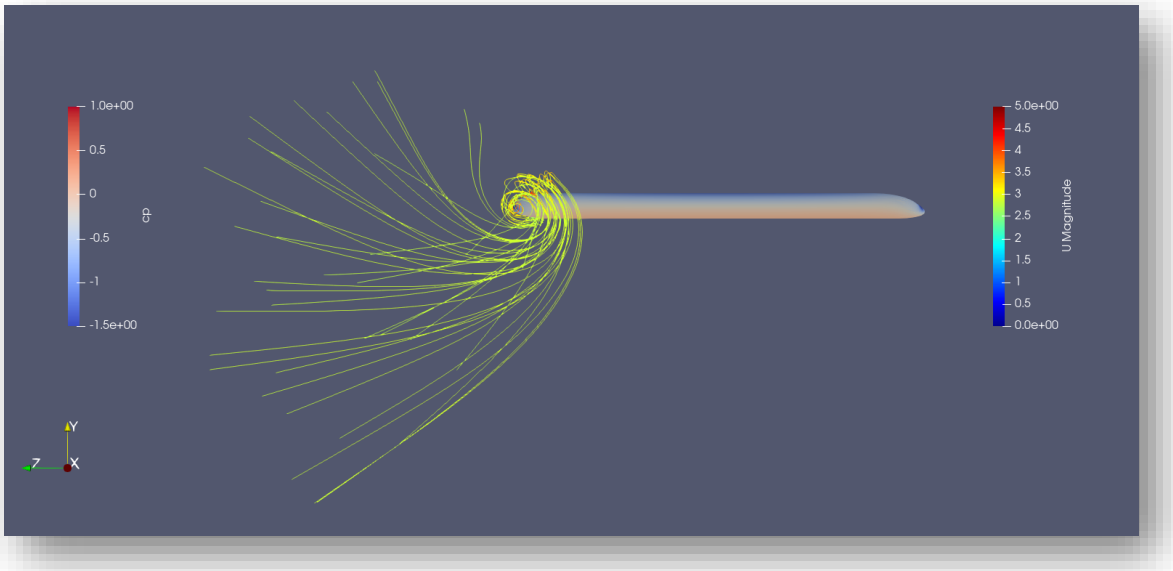

FIGURE 123 BEHIND VIEW

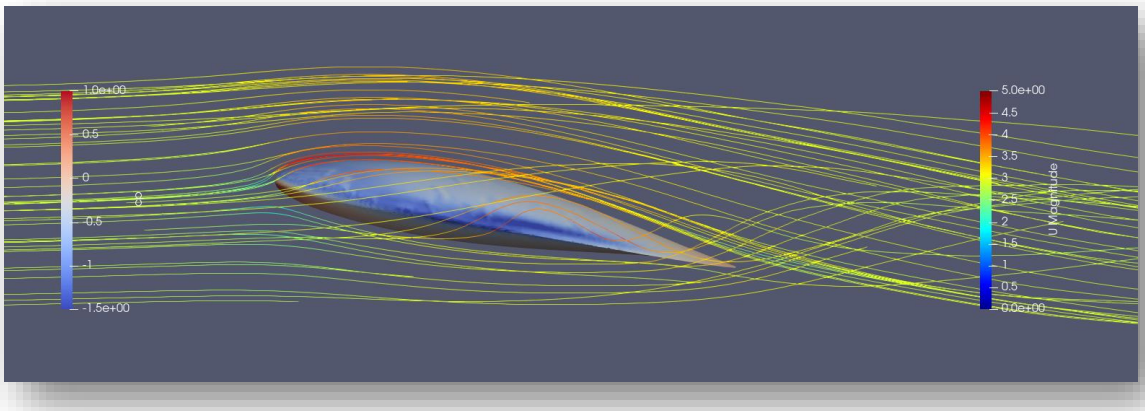

FIGURE 124 SIDE VIEW

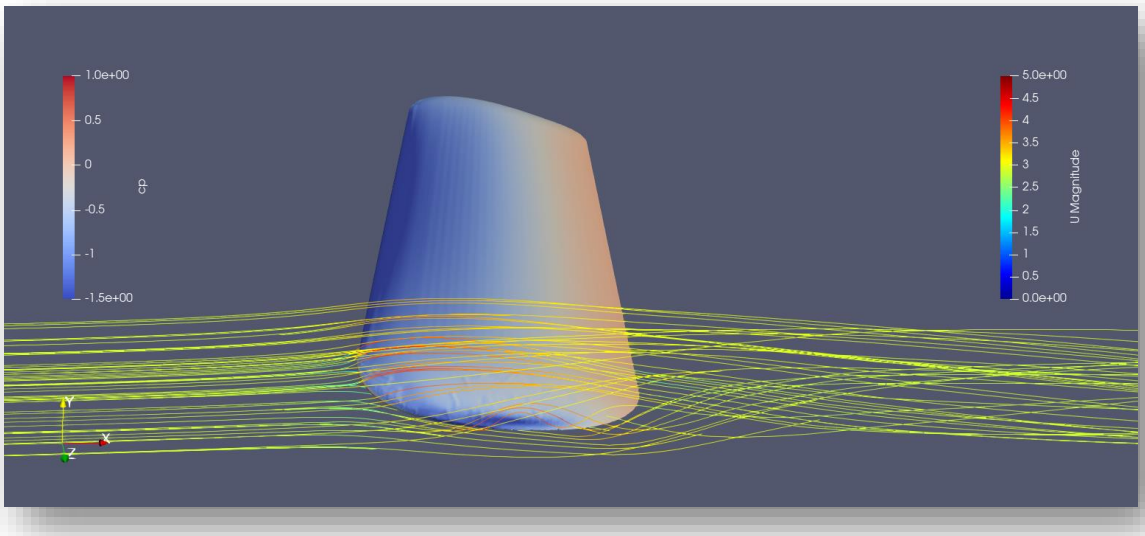

FIGURE 125 TOP VIEW

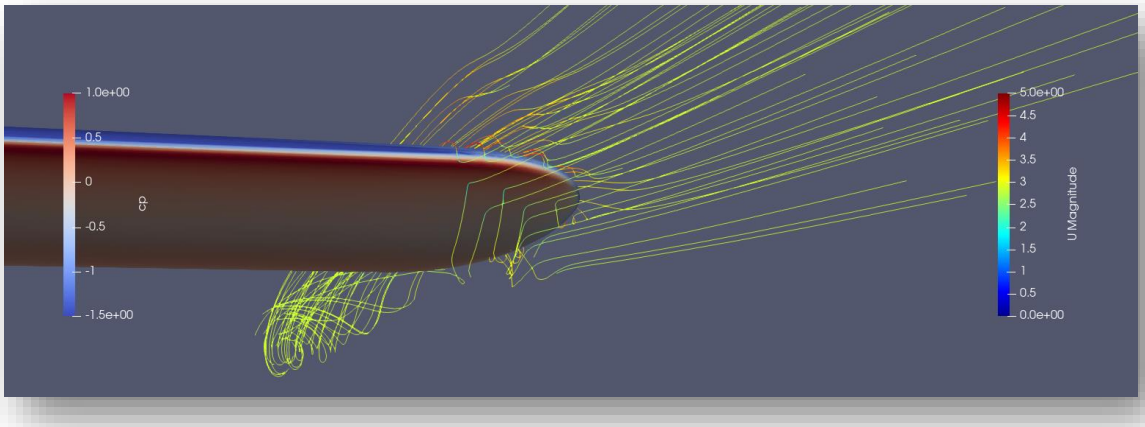

FIGURE 126 BENEATH VIEW

4.2.3 Lift Coefficient, Drag Coefficient and Lift-to-Drag Ratio

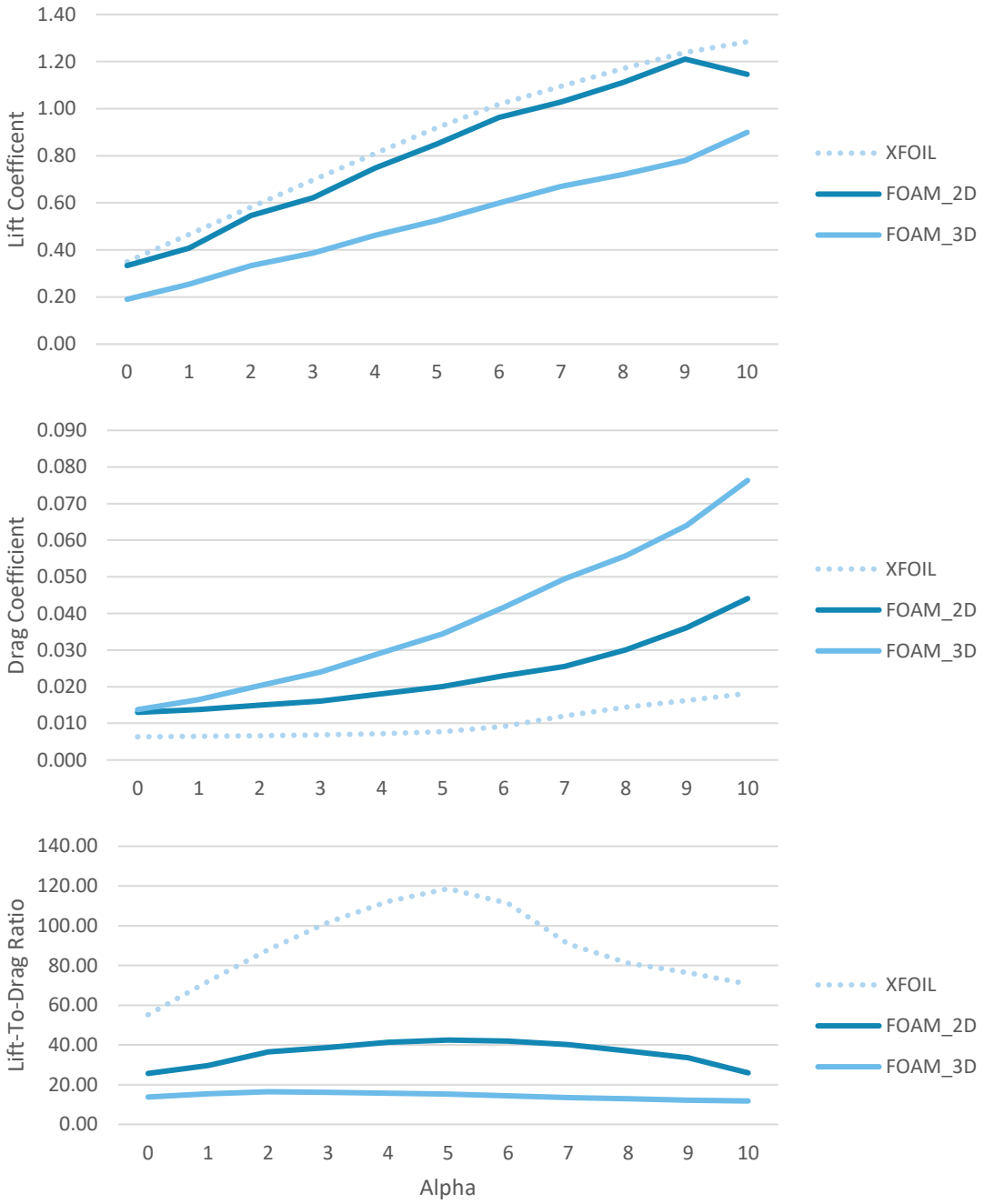

FIGURE 127 COMPARING 2D AND 3D SIMULATION TO XFOIL FOR $Re = 1e6$

4.3 3D Simulation – Kite

As in 3D simulation of the wing. The same set up was used only adding the propeller. The focus in this last sub part is to extract the *thrust* and *torque* from the propeller to generate the *performance* and *power* curve. To solve the *transient* case **foamPimple** was used.

4.3.1 Computational Setup

4.3.1.1 Geometry

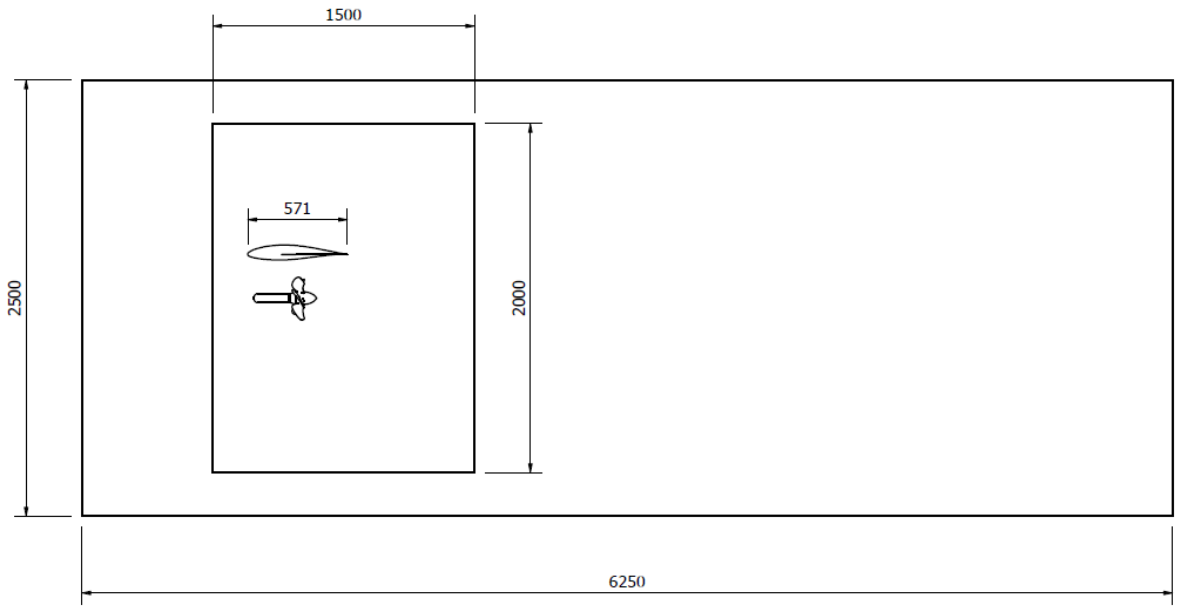

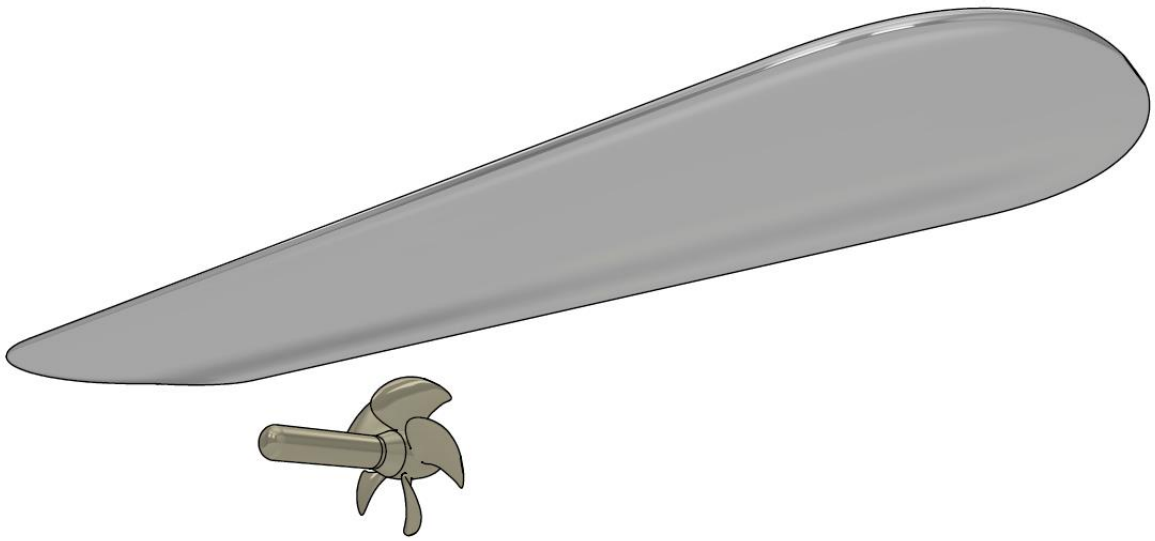

4.3.1.2 Mesh

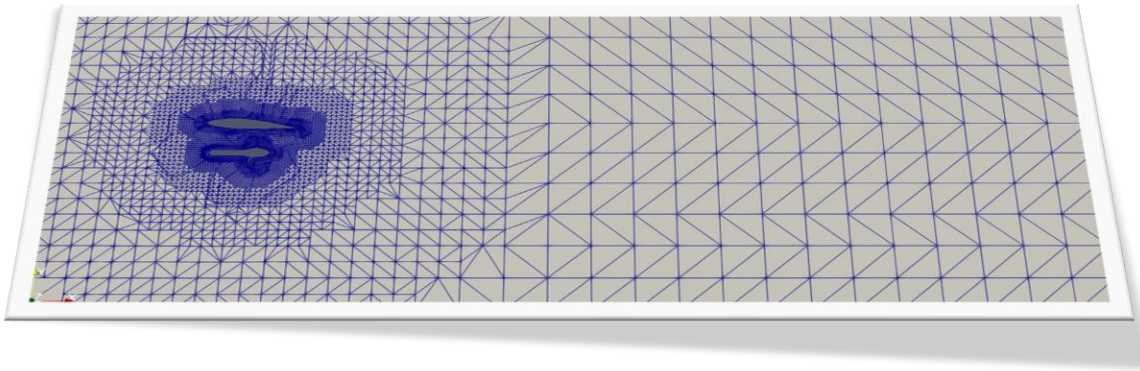

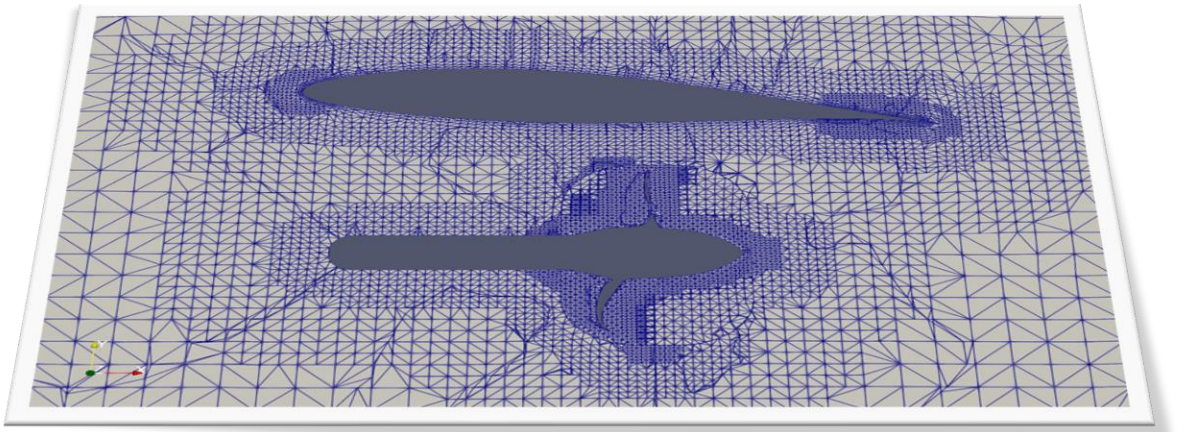

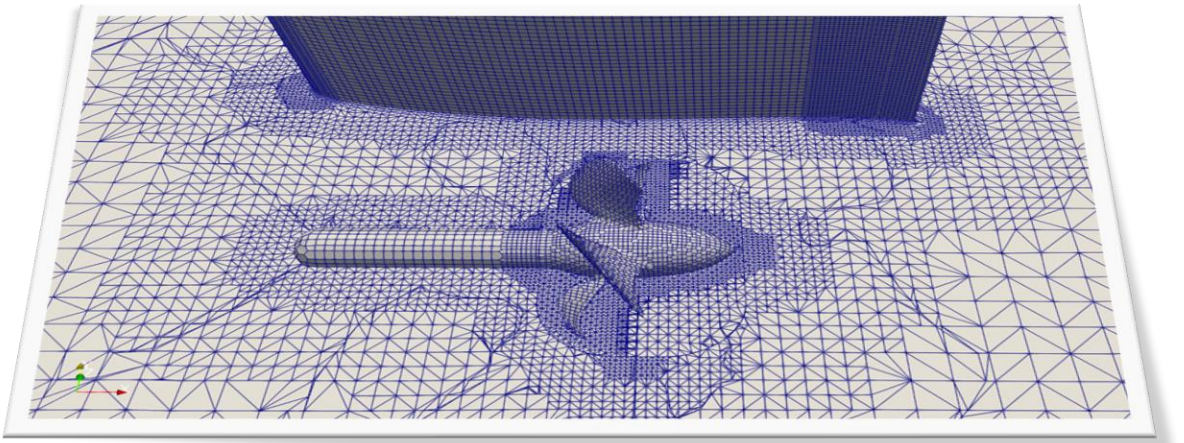

4.3.2 Results

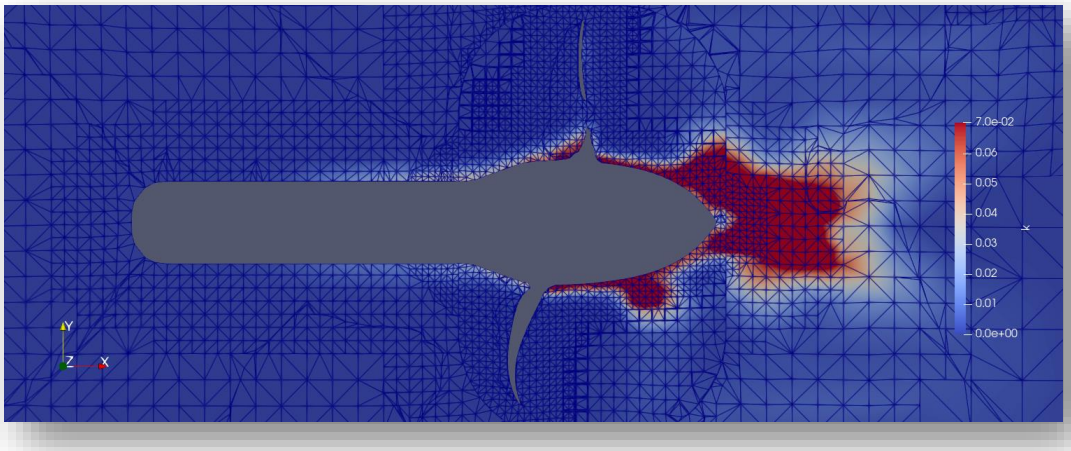

FIGURE 128 TURBULENT KINETIC ENERGY – k

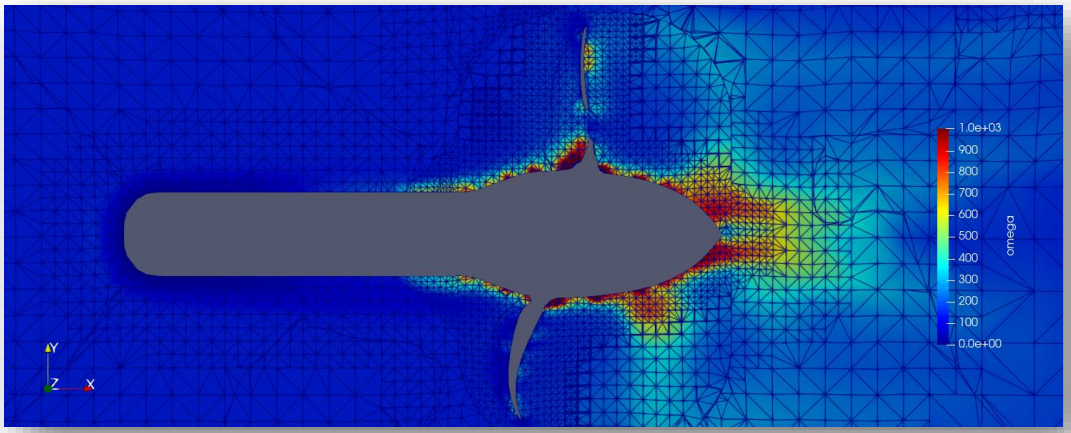

FIGURE 129 TURBULENCE FREQUENCY – ω

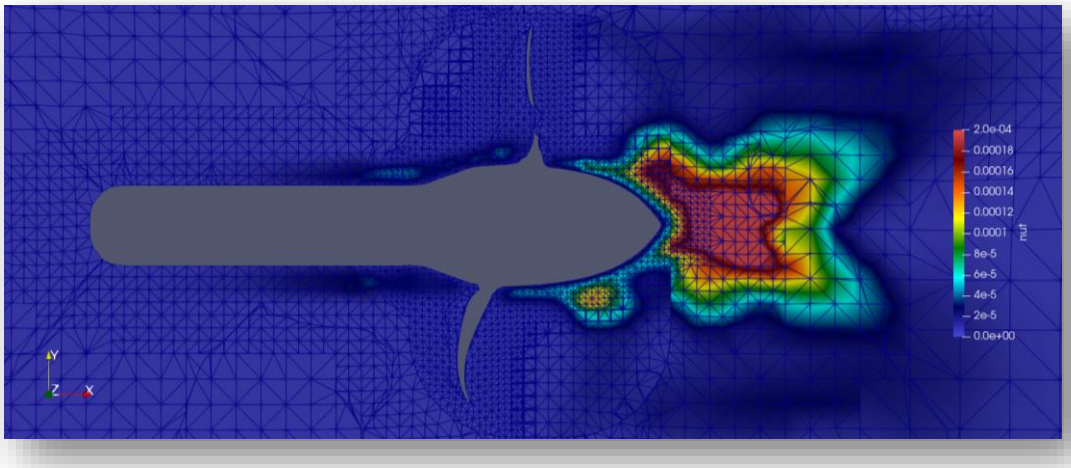

FIGURE 130 TURBULENCE EDDY VISCOSITY – ν_t

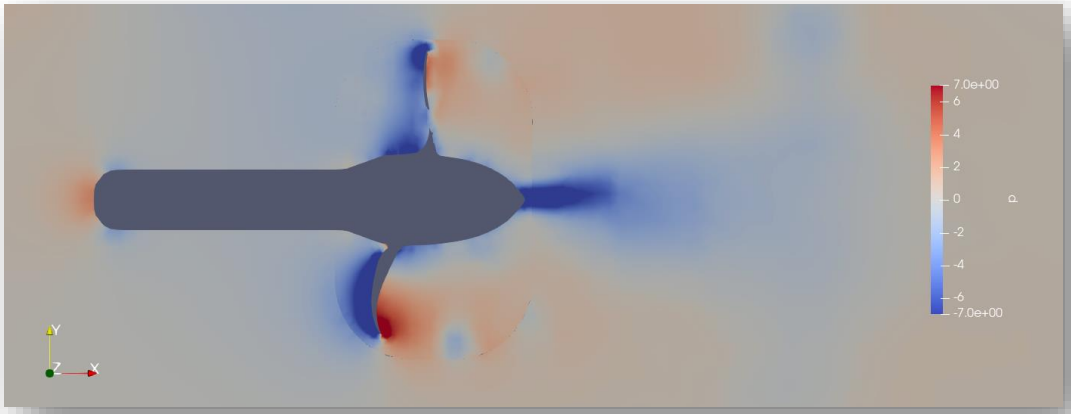

FIGURE 131 PRESSURE COEFFICIENT – c_p

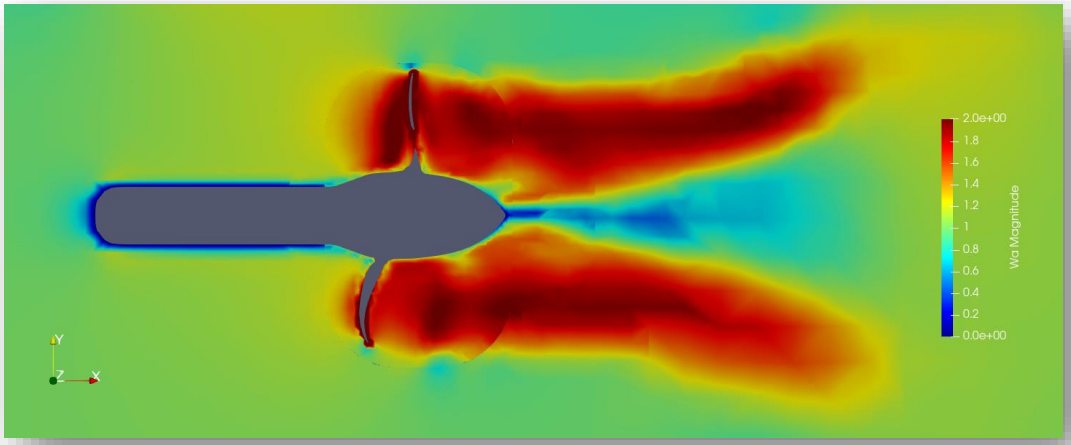

FIGURE 132 VELOCITY MAGNITUDE – U

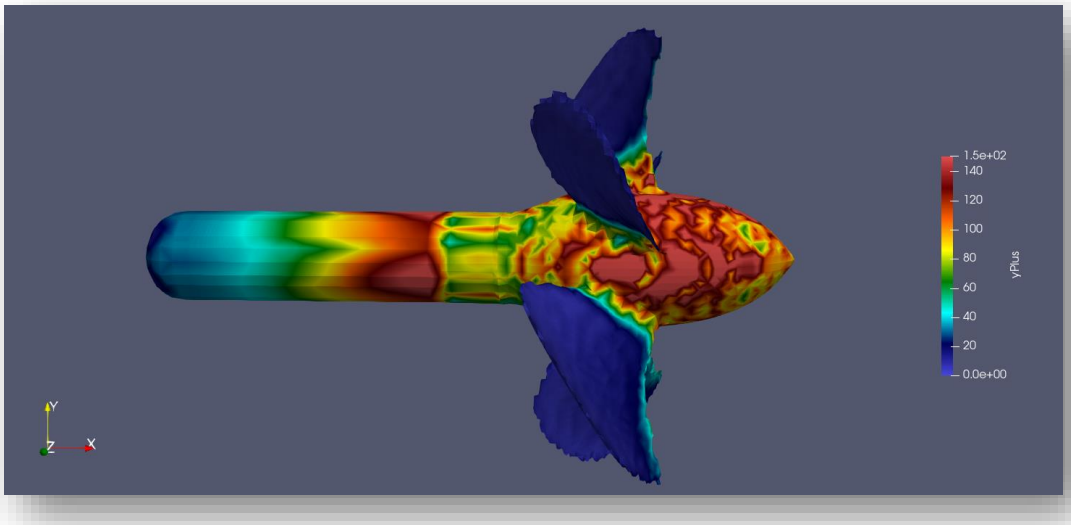

FIGURE 133 YPLUS – y^+

4.3.3 Lift Coefficient, Drag Coefficient and Lift-to-Drag Ratio

The figure below compares 2D and 3D simulation to XFOIL. It is worth noting how little effect the propeller has on the lift and drag coefficient. The small reduction in lift and drag almost balances out and the lift-to-drag ratio and appears almost to be indistinguishable with or without propeller.

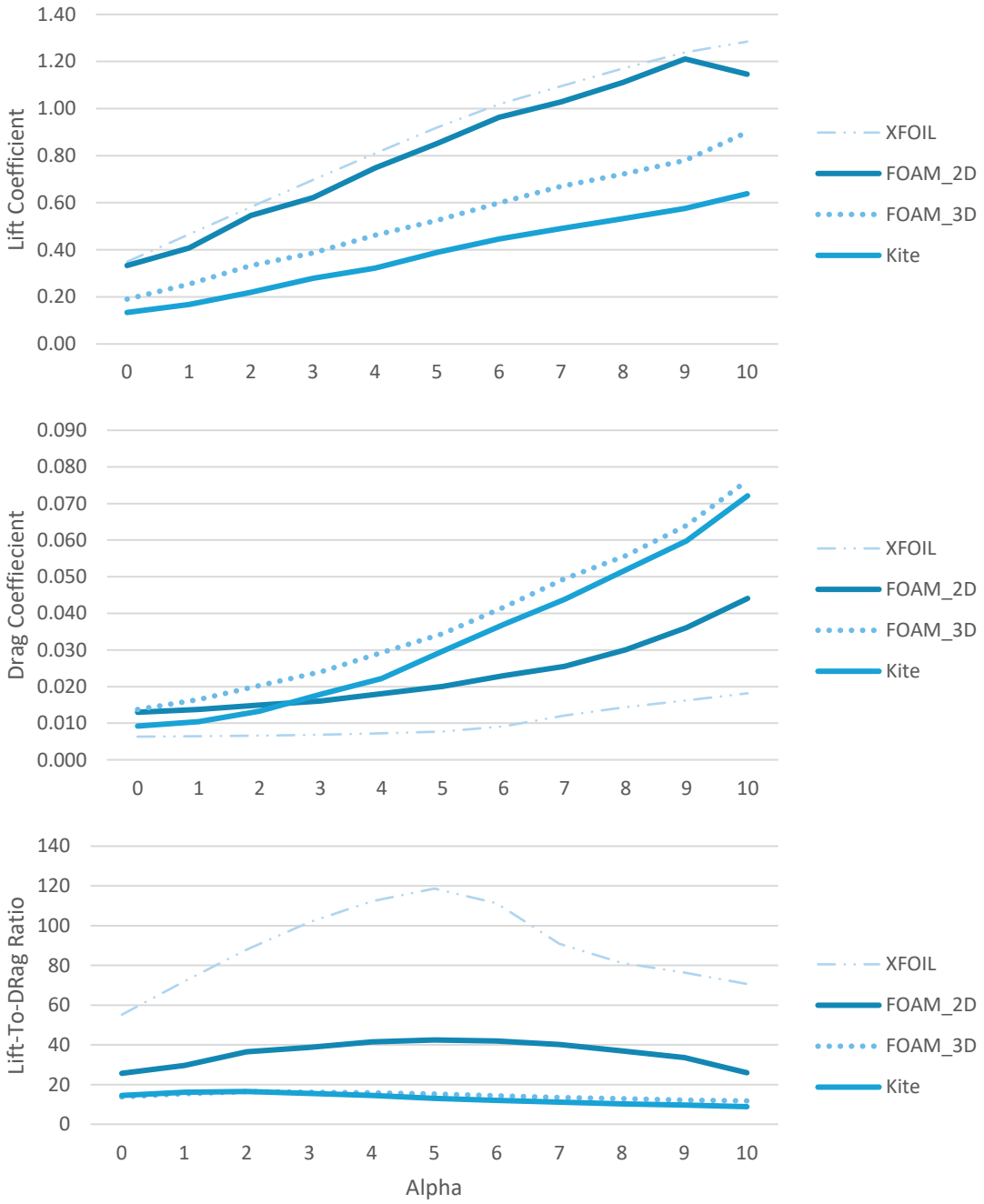

FIGURE 134 COMPARING 2D, 3D AND KITE TO XFOIL FOR $Re = 1e6$

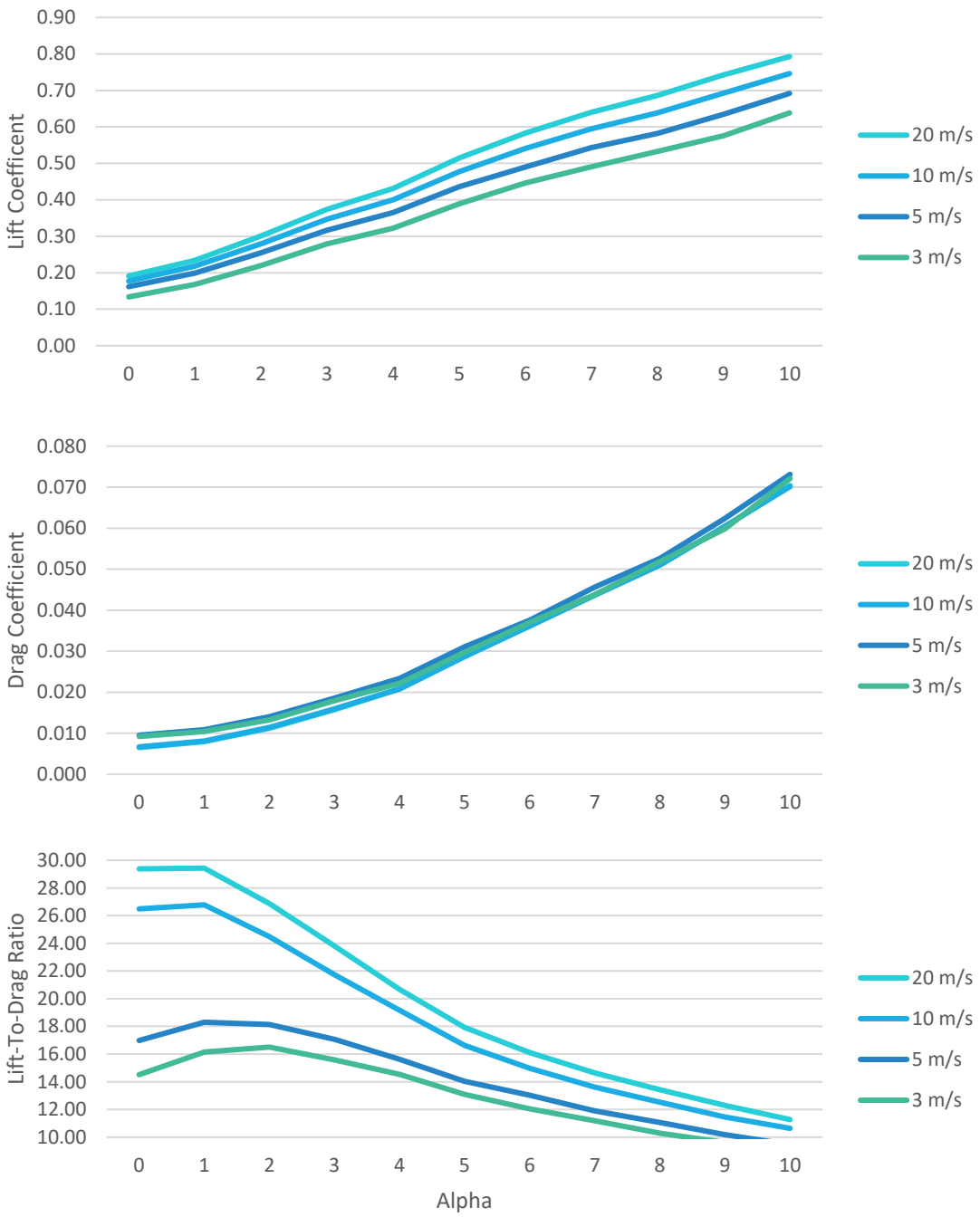

FIGURE 135 COMPARING DIFFERENT VELOCITIES AND REYNOLD'S NUMBERS

The optimal lift-to-drag ratio is about $\alpha = 1°$ for $20\ m/s$ and $10\ m/s$ and around $\alpha = 2°$ for the $5\ m/s$ and $3\ m/s$ case. The lift-to-drag ratio range from about 16 to almost 30. At these high Re it is worth noting that the flow seems to be almost independent of Re. Another point to take notice of is the lift coefficient is no way near $C_L = 1.0$ assumed by Loyd and used in the calculation of the needed wingspan. Consequently, a much larger wing is most likely needed for a turbine of this size.

4.3.4 Propeller with and without Wing

The same simulation set up as in the PPTC was repeated for the **kite** (propeller and wing). The figure below compares the medium mesh case and the experimental data to the 3D simulation of the kite. Note how the optimal η_0 is shifted away from 1.3 towards 1.2 (or less).

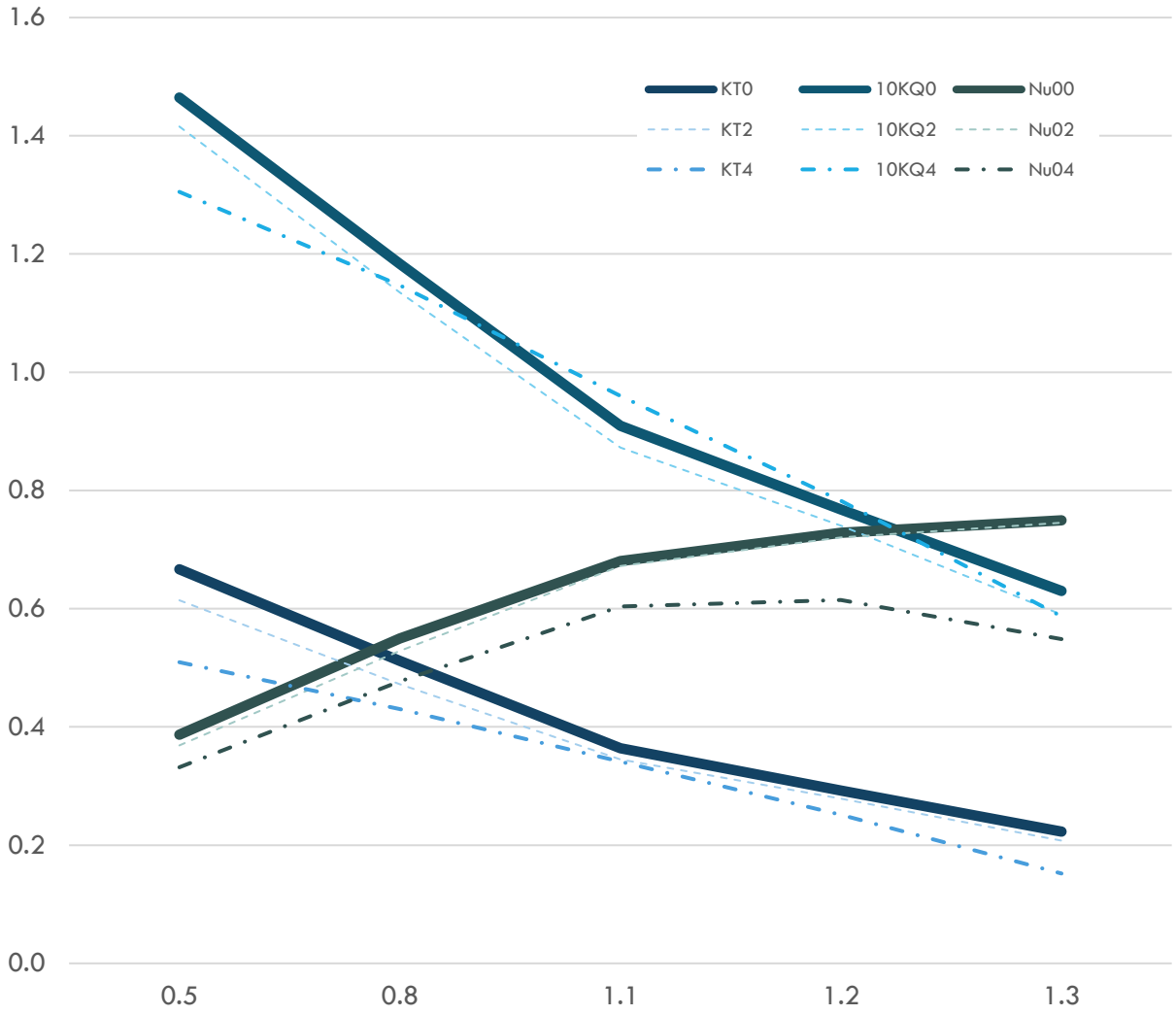

FIGURE 136 K_T, $10K_Q$ AND μ_0. INDEX 0 IS EXPERIMENTAL DATA (PPTC). INDEX 2 IS PROPELLER WITHOUT KITE (MEDIUM MESH), INDEX 4 IS PROPELLER WITH KITE (MEDIUM MESH).

5 Performance and Power

The four first diamonds on the performance curve below were produced from the thrust and torque results from the 3D simulation for the different velocities at the optimal lift-to-drag ratio. The last diamond, the fifth, is extrapolated from the previous four values. For a rated 100 kW Kite (indicated by the horizontal line) an apparent velocity at $24\,m/s$ is needed. Without considering the larger wing area needed and the more realistic lift coefficient, the curve below is a useful indication of the potential in a TUSK system.

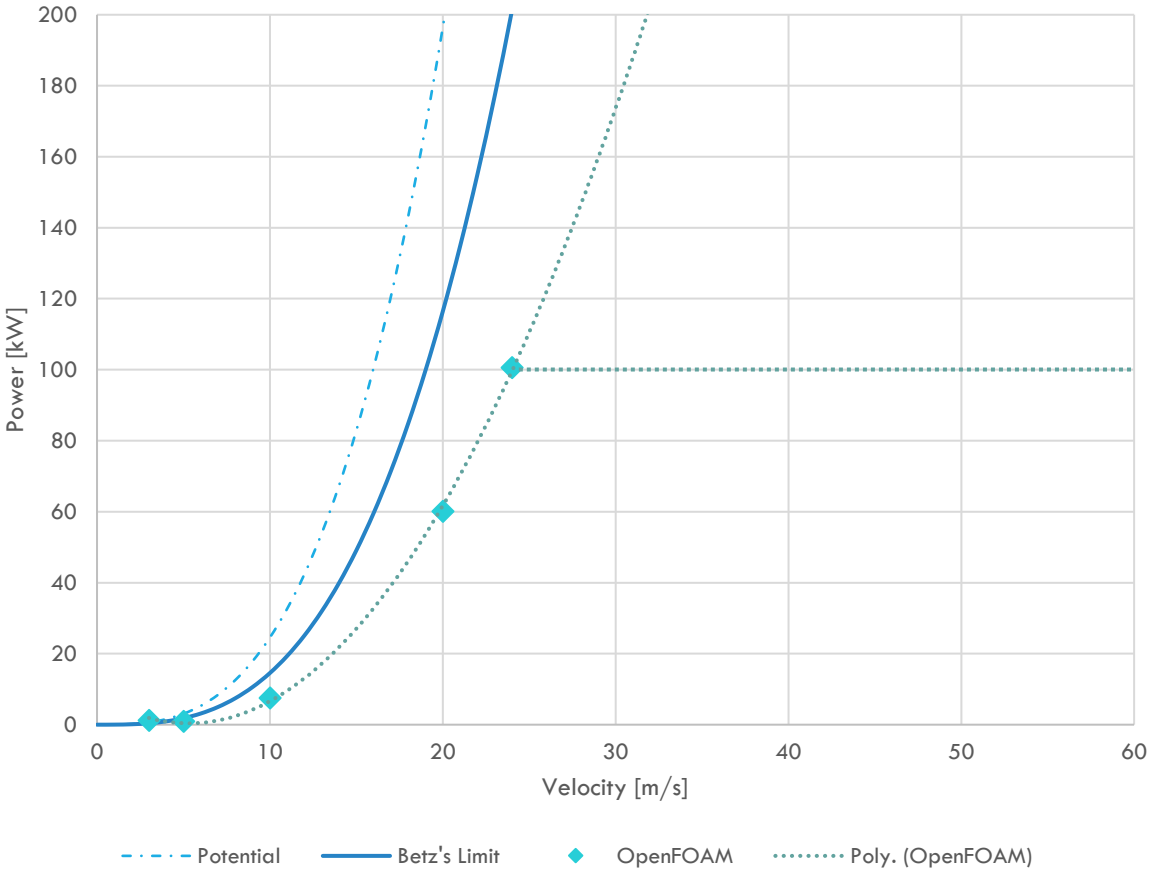

FIGURE 137 PERFORMANCE CURVE USING POTSDAM PROPELLER AS TURBINES

Using Loyd's formulation, a potential power curve can be generated. The figure below indicate that a 1 MW Kite can be achieved assuming a current velocity of 2 m/s, a wing area 15 m^2, turbine diameter 1.04 m and a lift-to-drag ratio of 15. Assuming an efficiency $\eta = 0.3$ (i.e., 50 % beneath the upper Betz's Limit).

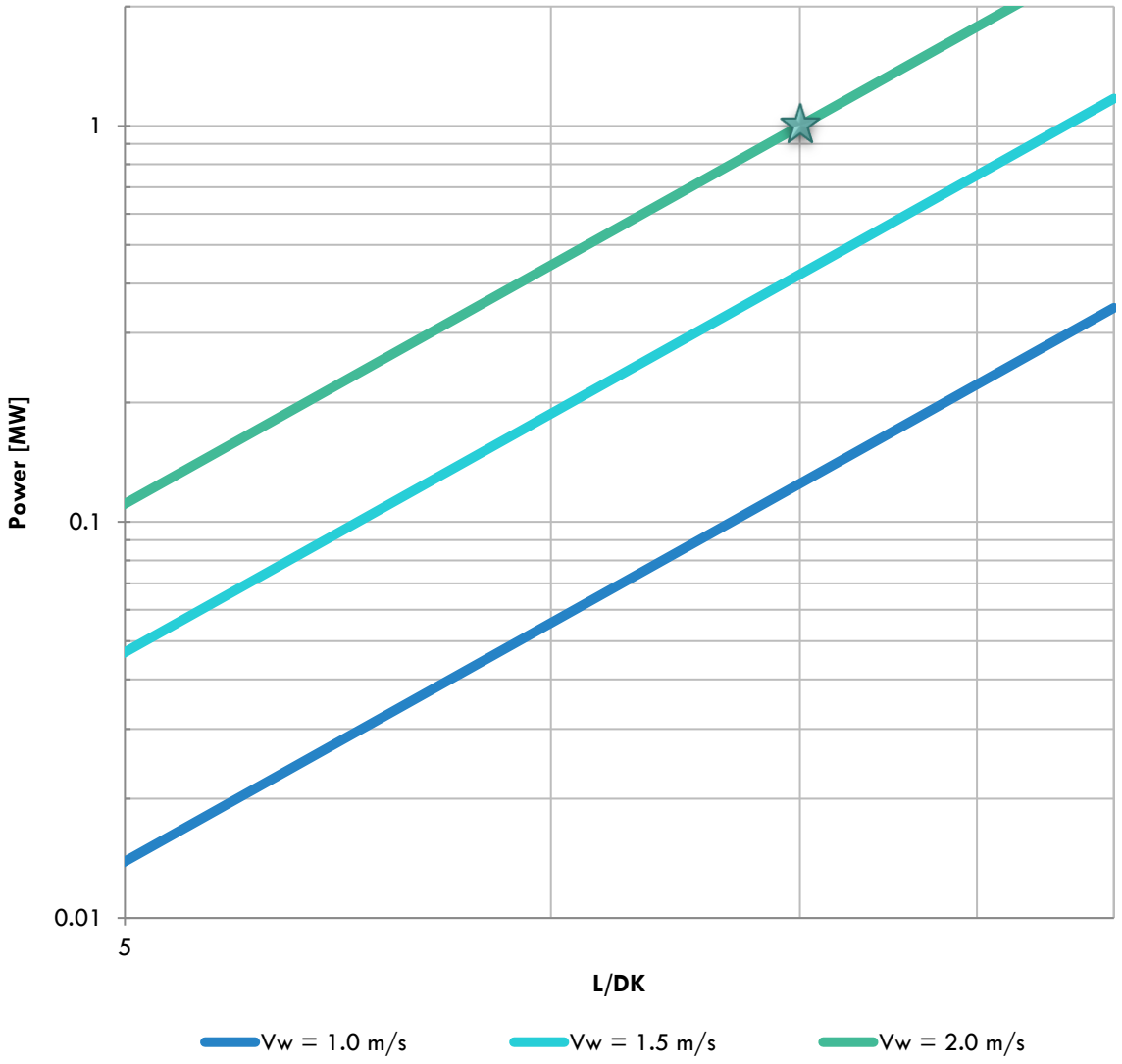

FIGURE 138 POTENTIAL POWER OUTPUT OF AN IDEAL CROSSWIND KITE OF 15 m^2 *WING AREA. (NOTE: LOGARITHMIC SCALE ON BOTH AXIS).*

Repeating the simulation for the up-scaled kite to verify the above-mentioned power out potential, the figure below is the performance curve with a rated power output of 1 MW (indicated by the horizontal line) at apparent velocity $20\ m/s$.

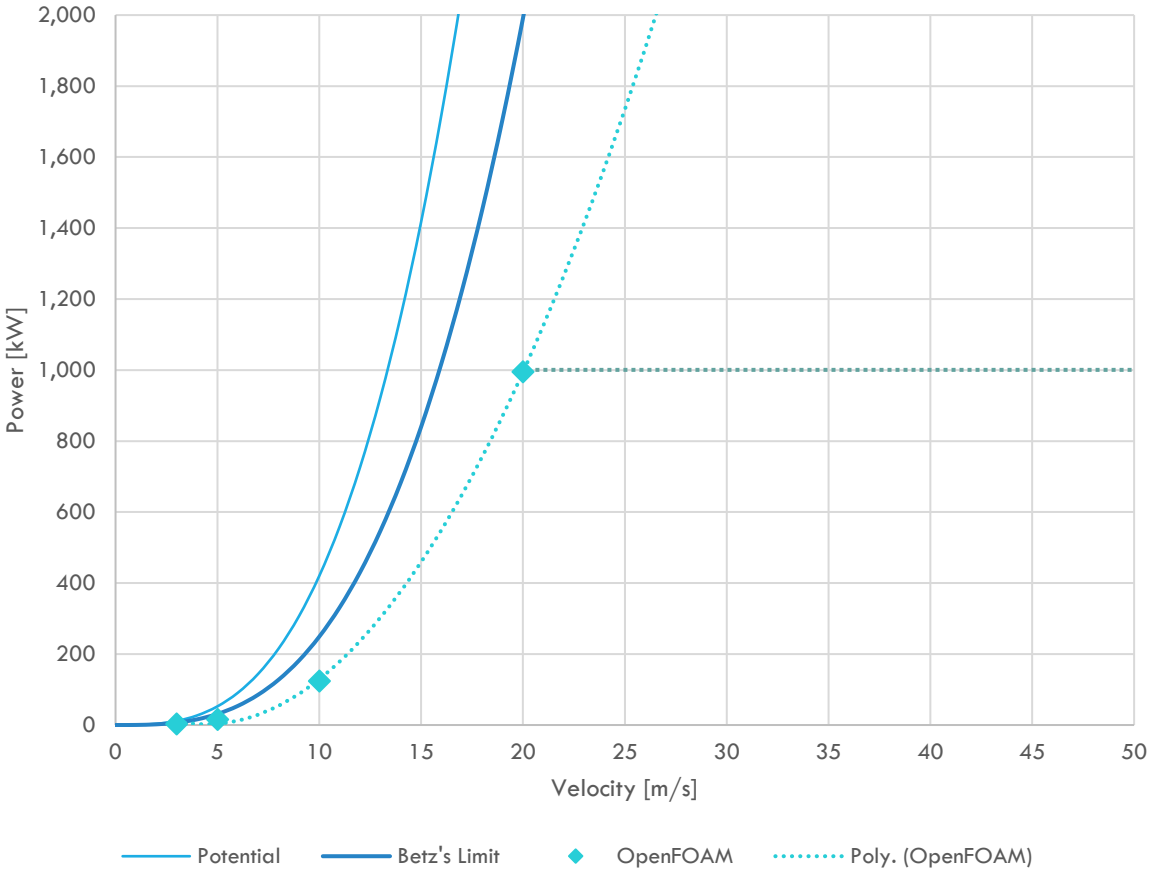

FIGURE 139 PERFORMANCE CURVE FOR 1MW RATED POWER OUTPUT AT $V_A = 20\ m/s$

6 Summary

6.1 Validation of Propeller

Given the very short time length of only $0.1\,s$, thrust and torque seems still to stabilize satisfactorily. Though a longer time length would stabilize it even further. The standard deviation was noticeable higher (though still small) for the coarse mesh (0.383% for thrust and 0.183% for torque) compared to the finer mesh (0.006% for thrust and 0.062% for torque).

Calculation of *trust coefficient* K_T, *torque coefficient* $10K_Q$ and the open water *efficiency* η_0 showed that the coarse mesh deviated 21.6% from the experimental data at the last data point. The medium and coarse mesh deviated by 7.69% and 8.77% respectively. It is also worth noting that the final mesh refinement did not seem to give any noticeable improvements. To improve the simulation a different meshing technique where a more uniform boundary layer of fine mesh covering the whole blade surface may be considered for future works, instead of blindly increasing the number of cells.

Comparison of the velocity field of the simulation seems to agree well with the experimental data. Especially satisfactory is the simulation's ability to capture the vortex at the blade tips. More important however is the SST $k-\omega$ turbulence model's ability to simulate the near wall conditions while allowing for initial values for the free-stream up-stream of the propeller at the inlet boundary to be set. Tweaking the constant of the model may be considered if further mesh refinement proves to be unfruitful.

Wake field study do not directly influence FOAM's ability to predict thrust and torque but can illustrate overall performance. To be able to capture turbulence and vortexes will be even more important when simulating lift and drag over the hydrokinetic kite at high Reynolds numbers.

6.2 Validation of Kite

XFOIL was a useful starting point to get some indication of the flow condition for different velocities and Reynold's Numbers. Lift and drag coefficient were also needed to plot the lift-to-drag ratio for comparison with the simulations.

For 2D simulations the y^+ values were below 30 for $Re = 1e6$ for most of the surface. For higher Re the y^+ averaged above 100 but not reaching 300 for most of the surface. For 3D simulation y^+ values were generally higher and particularly high around the wing tip. For the propeller simulation y^+ was most severe at the hub surface where the most adverse effects were to be found. The sharp trailing edge of the wing produced less satisfactory mesh structures and is a significant source of uncertainty. The relatively coarse mesh resolution explains some but not all the discrepancy between XFOIL data and FOAM results. Wing tip vortices clearly explains the difference between 2D and 3D simulations which was expected from the theory on finite wing.

The propeller seems to have small effect on the flow condition of the wing. The wing appears also to have minor effects on the propeller. It is worth noting that the simulations performed in this project excluded any connecting and supporting structures and is therefore too simplistic to have any fruitful indication of the interplay between the propeller and the wing. The wake field behind the propeller indicate that the short simulation time was insufficient for a mature wake field to develop, however the thrust and torque values extracted from the simulation is still deems satisfactory for the purpose of generating performance and power curves. The $100\ kW$ and $1\ MW$ performance curve illustrate well the potential in the TUSK systems.

More worrisome is the seemingly low angle of attack for the optimal lift-to-drag ratio and the correspondingly low lift coefficient. Even at $\alpha = 5°$ the $C_L = 1.0$ assumed by Loyd seems too optimistic, the $L/D_K = 15$ on the other hand seems rather pessimistic. It is not clear whether the compromise is to operate the kite at higher α away from the optimal lift-to-drag ratio. The computational setup is deemed satisfactory for simulation of a TUSK concept for energy production utilizing tidal stream or ocean current.

7 Future Works

The priority for future works is simulation with higher mesh resolution to increase computational precision. As a start a O-grid or C-grid mesh with $y^+ < 1$ with the mesh fully resolved to the wall instead of using wall function should be studied. This might help explain the discrepancy between XFOIL data and FOAM results.

The result from this work is rudimentary and is to be considered preliminary. A full assembly with the tether and support structure is also necessary for a more comprehensive understanding of the flow conditions around the surrounding supporting structures.

Another aspect not explored in this work is the dynamic simulation of the kite following a figure eight path. The effects of the maneuvering of the kite through the flight path on the power out and performance of the kite is of great interest for a startup aiming to harness the potential in the tidal and ocean current. Control systems and maneuvering mechanism should be thoroughly studied. Experiment with a model size kite in a pool like those performed at Potsdam or Worchester would be useful to better understand flight path, control mechanism and actual power output.

At high Re cavitation should be studied more thoroughly. Both in respect to performance but also structural integrity and maintenance. Cavitation around propeller tip is well studied in the literature, less so is the study of cavitation around wing tip, trailing edge, tether and supporting structures.

A concept worth exploring is the diffuser enhanced funnel in combination with the propeller. Tidal turbine concepts using this design has been studied in the literature but combining this with the TUSK system has yet to be studied more fully.

To enhance the CFD tool the Detached Eddy Simulations (DES) feature might be an interesting avenue to explore. It uses Large Eddy Simulation (LES) principles to capture large turbulent structures where the mesh is sufficiently fine. It might be useful for flow with severe adverse effects.

8 References

[1] C.-J. Bai and W.-C. Wang, "Review of computational and experimental approaches to analysis of aerodynamic performance in horizontal-axis wind turbines (HAWTs)," *Renewable and Sustainable Energy Reviews,* vol. 63, p. 506–519, 2016.

[2] J. M. O'Brien, T. M. Young, D. C. O'Mahoney and P. C. Griffin, "Horizontal axis wind turbine research: A review of commercial CFD, FE codes and experimental practices," *Progress in Aerospace Sciences,* vol. 92, pp. 1-24, 2017.

[3] P.-Å. Krogstad and . M. S. Adaramola, "Performance and near wake measurements of a model horizontal axis wind turbine," *Wind Energy,* vol. 15, p. 743–756, 2012.

[4] P.-Å. Krogstad and P. E. Eriksen, "“Blind test” calculations of the performance and wake development for a model wind turbine," *Renewable Energy,* vol. 15, pp. 325-333, 2013.

[5] F. Pierella, P.-Å. Krogstad and L. Sætran, "Blind Test 2 calculations for two in-line model wind turbines where the downstream turbine operates at various rotational speeds," *Renewable Energy,* vol. 70, pp. 62-77, 2014.

[6] P.-Å. Krogstad, L. Sætran and M. S. Adaramola, "“Blind Test3” calculations of the performance and wake development behind two in-line and offset model wind turbines," *Journal of Fluids and Structures,* vol. 52, pp. 65-80, 2015.

[7] NREL, "Unsteady Aerodynamics Experiment Phase VI: Wind Tunnel Test Configurations and Available Data Campaigns," 2001.

[8] NREL, "NREL Unsteady Aerodynamics Experiment in the NASA-Ames Wind Tunnel: A Comparison of Predictions to Measurements," 2001.

[9] X.-f. Lin, . J.-s. Zhang, . Y.-q. Zhang, J. Zhang and S. Liu, "Comparison of Actuator Line Method and Full Rotor Geometry Simulations of theWake Field of a Tidal Stream Turbine," *Water,* vol. 11, 2019.

[10] H.-n. Wu, L.-j. Chen, M.-h. Yu, W.-y. Li and B.-f. Chen, "On design and performance prediction of the horizontal-axis water turbine," *Ocean Engineering,* vol. 50, pp. 23-30, 2012.

[11] S. Laín, L. T. Contreras and O. López, "A review on computational fluid dynamics modeling and simulation of horizontal axis hydrokinetic turbines," *Journal of the Brazilian Society of Mechanical Sciences and Engineering,* vol. 41, p. 375, 2019.

[12] A. S. Bahaj, A. F. Molland, J. R. Chaplin and W. Batten, "Power and thrust measurements of marine current turbines under various hydrodynamic flow conditions in a cavitation tunnel and a towing tank," *Renewable Energy,* vol. 32, p. 407–426, 2007.

[13] M. M. Nunes, R. C. Mendes, T. F. Oliveira and A. C. Brasil Jr., "An experimental study on the diffuser-enhanced propeller hydrokinetic turbines," *Renewable Energy,* vol. 133, pp. 840-848, 2019.

[14] "Performance of a horizontal axis marine current turbinee A comprehensive evaluation using experimental, numerical, and theoretical approaches," *Energy,* vol. 148, pp. 965-976, 2018.

[15] A. S. Bahaj, W. Batten and G. McCann, "Experimental verifications of numerical predictions for the hydrodynamic performance of horizontal axis marine current turbines," *Renewable Energy,* vol. 32, p. 2479–2490, 2007.

[16] M. Lloyd, "Crosswind Kite Power," *Energy,* vol. 4, p. 106, 1980.

[17] A. Cherubini, A. Papini and M. Fontana, "Airborne Wind Energy Systems: A review of the technologies," *Renewable and Sustainable Energy Reviews,* vol. 51, p. 1461–1476, 2015.

[18] F. Bauer, R. M. Kennel, C. M. Hackl, F. Campagnolo, M. Patt and R. Schmehl, "Drag power kite with very high lift coefficient," *Renewable Energy,* vol. 118, pp. 290-305, 2017.

[19] Makani, "The Energy Kite: Selected Results From the Design, Development and Testing of Makani's Airborne Wind Turbines," 2019.

[20] G. Shirah, "Scientic Visualization Studio," NASA, 24 September 2012. [Online]. [Accessed 2021].

[21] N. Aye-Addo, J. O'Connor and R. Perez, "Design of a Scale-Model Tethered Undersea Kite for Power Generation," 2014.

[22] A. J. Higgins, J. K. O'Hara, M. Pepic, D. J. Porter and P. D. Melander, "Design and Testing of a Scale-Model Surface Undersea Kite," 2014.

[23] R. A. Fredette, "Scale-Model Testing of Tethered Undersea Kites for Power Generation," 2015.

[24] A. Ghasemi, "Computational Modelling of Tethered Undersea Kites for Power Generation," 2017.

[25] H. Li, "Modelling and Control of Kite Energy Systems," 2017.

[26] XFOIL, Feb 2021. [Online]. Available: http://web.mit.edu/drela/Public/web/xfoil/.

[27] M. Drela, "XFOIL: An Analysis and Design System for Low Reynolds Number Airfoils," in *Conference on Low Reynolds Number Airfoil Aerodynamics*, 1989.

[28] J. Morgado, R. Vizinho, M. Silvestre and J. Páscoa, "XFOIL vsCFD performance predictions for high lift low Reynoldsnumber airfoils," *Aerospace Science and Technology*, vol. 52, pp. 207-214, 2016.

[29] M. S. Selig and J. J. Guglielmo, "High-lift low Reynolds number airfoil design," *Jpurnal of Aircraft*, vol. 34, no. 1, 1997.

[30] AIRFOILS INC PORT MATILDA PA, "Comparisons of Theoretical Methods for Predicting Airfoil Aerodynamic Characteristics," U.S. ARMY RESEARCH, DEVELOPMENT AND ENGINEERING COMMAND, Port Matilda PA.

[31] UIUC, "UIUC Airfoil Coordinates Database," UIUC Applied Aerodynamics Group, [Online]. Available: https://m-selig.ae.illinois.edu/ads/coord_database.html. [Accessed Feb 2021].

[32] F. Villalpando, M. Reggio and A. Ilinca, "Assessment of TurbulenceModels for Flow Simulation around aWind Turbine Airfoil," *Modelling and Simulation in Engineering*, 2011.

[33] E. Sagol, M. Reggio and A. Ilinca, "Assessment of Two-Equation TurbulenceModels and Validation of the Performance Characteristics of an ExperimentalWind Turbine by CFD," *International Scholarly Research Network ISRN Mechanical Engineering*, 2012.

[34] H. K. Versteeg and W. Malalasekera, An Introduction to Computational Fluid Dynamics - The Finite Volume Method, 2nd ed., Harlaw: Person / Prentice Hall, 2007.

[35] Y. A. Çengel and J. M. Cimbala, Fluid Mechanics: Fundamentals and Applications, McGraw-Hill, 2006.

[36] leap australia, "TIPS & TRICKS: TURBULENCE PART 2 - WALL FUNCTIONS AND Y+ REQUIREMENTS," Leading Engineering Application Providers (LEAP), [Online]. Available: https://www.computationalfluiddynamics.com.au/tips-tricks-turbulence-wall-functions-and-y-requirements/. [Accessed Jan 2021].

[37] F. Liu, "A Thorough Description Of How Wall Functions Are Implemented In OpenFOAM," Chalmers University of Technology, 2017.

[38] J. D. Anderson, Jr., Fundamentals of Aerodynamics, New York: McGraw-Hill, 2011.

[39] SVA, "Schiffbau-Versuchsanstalt Potsdam," [Online]. Available: https://www.sva-potsdam.de/en/potsdam-propeller-test-case-pptc/. [Accessed 01 2021].

[40] Schiffbau-Versuchsanstalt Potsdam (SVA), "Open Water Tests with the Model Propeller VP1304 - Report 3752," Potsdam, 2011.

[41] Schiffbau-Versuchsanstalt (SVA), "LDV Velocity Measurements with the Model Propeller VP1304 - Report 3754," Potsdam, 2011.

[42] Schiffbau-Versuchsanstalt (SVA) Potsdam, Jan 2021. [Online]. Available: https://www.sva-potsdam.de/en/potsdam-propeller-test-case-pptc/.

[43] H. Schlichting, Boundary Layer Theory, 7th ed., McGraw-Hill, 1979.

[44] Schiffbau-Versuchsanstalt Potsdam (SVA), "PPTC smp'11 Workshop," [Online]. Available: https://www.sva-potsdam.de/en/pptc-smp11-workshop/. [Accessed 2021].

[45] I. NEZU and A. TOMINAGA, "Suirigaku", Asakura Shoten, 2000, pp. 130-133.